NUREG/CR-6809
SAND2003-0839P
ANA-01-0330

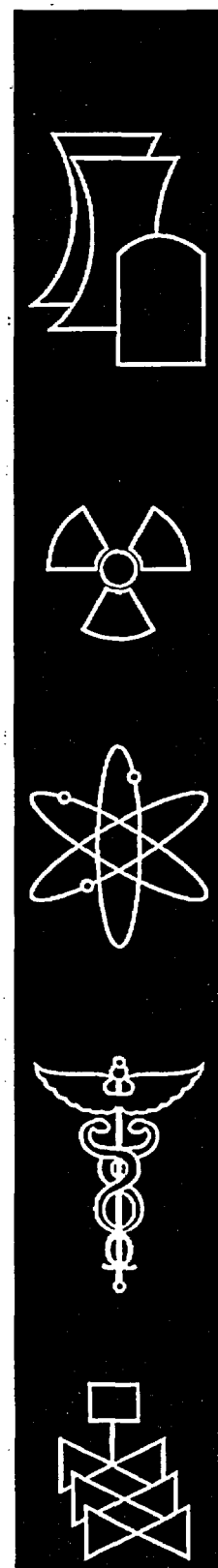

Posttest Analysis of the NUPEC/NRC 1:4 Scale Prestressed Concrete Containment Vessel Model

ANATECH Corporation

Sandia National Laboratories

U.S. Nuclear Regulatory Commission
Office of Nuclear Regulatory Research
Washington, DC 20555-0001

AVAILABILITY OF REFERENCE MATERIALS IN NRC PUBLICATIONS

NRC Reference Material

As of November 1999, you may electronically access NUREG-series publications and other NRC records at NRC's Public Electronic Reading Room at http://www.nrc.gov/reading-rm.html. Publicly released records include, to name a few, NUREG-series publications; *Federal Register* notices; applicant, licensee, and vendor documents and correspondence; NRC correspondence and internal memoranda; bulletins and information notices; inspection and investigative reports; licensee event reports; and Commission papers and their attachments.

NRC publications in the NUREG series, NRC regulations, and *Title 10, Energy*, in the Code of *Federal Regulations* may also be purchased from one of these two sources.

1. The Superintendent of Documents
   U.S. Government Printing Office
   Mail Stop SSOP
   Washington, DC 20402–0001
   Internet: bookstore.gpo.gov
   Telephone: 202-512-1800
   Fax: 202-512-2250
2. The National Technical Information Service
   Springfield, VA 22161–0002
   www.ntis.gov
   1–800–553–6847 or, locally, 703–605–6000

A single copy of each NRC draft report for comment is available free, to the extent of supply, upon written request as follows:

Address: Office of the Chief Information Officer,
Reproduction and Distribution
Services Section
U.S. Nuclear Regulatory Commission
Washington, DC 20555-0001
E-mail: DISTRIBUTION@nrc.gov
Facsimile: 301–415–2289

Some publications in the NUREG series that are posted at NRC's Web site address http://www.nrc.gov/reading-rm/doc-collections/nureqs are updated periodically and may differ from the last printed version. Although references to material found on a Web site bear the date the material was accessed, the material available on the date cited may subsequently be removed from the site.

Non-NRC Reference Material

Documents available from public and special technical libraries include all open literature items, such as books, journal articles, and transactions, *Federal Register* notices, Federal and State legislation, and congressional reports. Such documents as theses, dissertations, foreign reports and translations, and non-NRC conference proceedings may be purchased from their sponsoring organization.

Copies of industry codes and standards used in a substantive manner in the NRC regulatory process are maintained at—

The NRC Technical Library
Two White Flint North
11545 Rockville Pike
Rockville, MD 20852–2738

These standards are available in the library for reference use by the public. Codes and standards are usually copyrighted and may be purchased from the originating organization or, if they are American National Standards, from—

American National Standards Institute
11 West 42nd Street
New York, NY 10036–8002
www.ansi.org
212–642–4900

Legally binding regulatory requirements are stated only in laws; NRC regulations; licenses, including technical specifications; or orders, not in NUREG-series publications. The views expressed in contractor-prepared publications in this series are not necessarily those of the NRC.

The NUREG series comprises (1) technical and administrative reports and books prepared by the staff (NUREG–XXXX) or agency contractors (NUREG/CR–XXXX), (2) proceedings of conferences (NUREG/CP–XXXX), (3) reports resulting from international agreements (NUREG/IA–XXXX), (4) brochures (NUREG/BR–XXXX), and (5) compilations of legal decisions and orders of the Commission and Atomic and Safety Licensing Boards and of Directors' decisions under Section 2.206 of NRC's regulations (NUREG–0750).

NUREG/CR-6809
SAND2003-0839P
ANA-01-0330

Posttest Analysis of the NUPEC/NRC 1:4 Scale Prestressed Concrete Containment Vessel Model

Manuscript Completed: February 2003
Date Published: March 2003

Prepared by
R.A. Dameron, B.E. Hansen,
D.R. Parker, Y.R. Rashid

ANATECH Corporation
5435 Oberlin Drive
San Diego, CA 92121

M. Hessheimer, Sandia Project Monitor

Sandia National Laboratories
Operated by Sandia Corporation for the
U.S. Department of Energy
Albuquerque, NM 87185

J.F. Costello, NRC Project Manager

Prepared for
Division of Engineering Technology
Office of Nuclear Regulatory Research
U.S. Nuclear Regulatory Commission
Washington, DC 20555-0001
NRC Job Code Y6131

ABSTRACT

The Nuclear Power Engineering Corporation of Japan and the U.S. Nuclear Regulatory Commission, Office of Nuclear Regulatory Research, are cosponsoring and jointly funding a Cooperative Containment Research Program at Sandia National Laboratories (SNL) in Albuquerque, New Mexico. As a part of the program, a prestressed concrete containment vessel (PCCV) model was subjected to a series of overpressurization tests at SNL beginning in July 2000 and culminating in a functional failure mode or Limit State Test (LST) in September 2000 and a Structural Failure Mode Test (SFMT) in November 2001. The PCCV model, uniformly scaled at 1:4, represents the containment structure of an actual Pressurized Water Reactor (PWR) plant (OHI-3) in Japan. The objectives of the internal pressurization tests were to obtain measurement data on the structural response of the model to pressure loading beyond design basis accident in order to validate analytical modeling, find pressure capacity of the model, and observe its failure mechanisms.

This report compares results of pretest analytical studies of the PCCV model to the PCCV high pressure test measurements and describes results of posttest analytical studies. These analyses were performed by ANATECH Corp. under contract with SNL. The posttest analysis represents the third phase of a comprehensive PCCV analysis effort. The first phase consisted of preliminary analyses to determine what finite element models would be necessary for the pretest prediction analyses, and the second phase consisted of the pretest prediction analyses.

The principal objectives of the posttest analyses were: (1) to provide insights to improve the analytical methods for predicting the structural response and failure modes of a prestressed concrete containment, and (2) to evaluate by analysis any phenomena or failure mode observed during the test that had not been explicitly predicted by analysis. The posttest activities documented herein also include reviewing the effects of and "correcting" the test data for external factors that were not explicitly considered in the analyses, such as ambient temperature variations and artificial response data created by the instrumentation.

In addition to documenting the comparisons between measured behavior and predicted behavior of the liner, concrete, rebar, and tendons, a variety of failure modes and locations were investigated. Global analysis helped identify possible modes; other analyses investigated localized failure modes or modes specifically associated with 3D behavior. Liner tearing failure at the midheight of the cylinder near penetrations and a shear/bending failure at the base of the cylinder wall were both found to be competing failure modes. More detailed modeling of these locations placed a higher likelihood of failure on the liner tearing mode at the cylinder midheight near a major penetration. The most likely location for the liner tearing failure was near the Equipment Hatch at the ending point of a vertical T-anchor, near where the liner is attached to the thickened liner insert plate. The pressure at which the local analysis computed liner strains that reached the failure limits (indicating tearing and leakage) was 3.2 times the design pressure (Pd) of 0.39 MPa or 1.27 MPa. During the LST, liner tearing and leakage failure was first detected at a pressure of 2.4-2.5 Pd, and subsequent increase in pressure to 3.3 Pd resulted in further tearing at many strain concentration locations and increasing leakage. This report compares measured strains near as many of these strain concentrations as possible to the predictions from the global and local penetration analyses. The report also describes reanalysis of existing models and new analysis of new models, including representation of typical liner seam details aimed at simulating some local as-built conditions that existed in the test.

The LST resulted in liner tearing and leakage, but not in a structural failure. Structural damage was limited to concrete cracking and the overall structural response (displacements, rebar and tendon strains, etc.) was only slightly beyond yield. (Global hoop strains at the midheight of the cylinder only reached 0.4%, approximately twice the yield strain in steel.) In order to provide additional structural response data for comparison with in-elastic response conditions, the PCCV model was resealed, filled nearly full with water, and repressurized during the SFMT to a maximum pressure of 3.6 Pd when a catastrophic rupture occurred. A comparison of pretest and post-LST analysis results to the SFMT data and additional analyses, to provide some insight into the mechanisms leading to the structural failure, are also included in this report.

The report closes with summary and conclusions on the accuracy and adequacy of the pretest prediction analysis. The summary attempts to also draw lessons learned from previous containment research and highlight the new and unique lessons learned from the 1:4 scale PCCV project, such as the modeling and behavior of prestressing and some unique

liner seam details. These conclusions are then used to establish guidelines for containment analysis. The relevance of this research to U.S. plants is also discussed.

CONTENTS

FIGURES

Figure Page

TABLES

EXECUTIVE SUMMARY

The Nuclear Power Engineering Corporation (NUPEC) of Japan and the U.S. Nuclear Regulatory Commission (NRC), Office of Nuclear Regulatory Research, are cosponsoring and jointly funding a Cooperative Containment Research Program at Sandia National Laboratories[1] (SNL) in Albuquerque, New Mexico. As a part of the program, a prestressed concrete containment vessel (PCCV) model was subjected to a series of overpressurization tests at SNL beginning in July 2000 and culminating in a functional failure mode or Limit State Test (LST) in September 2000 and a Structural Failure Mode Test (SFMT) in November 2001. The PCCV model, uniformly scaled at 1:4, represents of the containment structure of an actual Pressurized Water Reactor (PWR) plant (OHI-3) in Japan. The objectives of the internal pressurization tests were to obtain measurement data of the model's structural response to pressure loading beyond design basis accident in order to validate analytical modeling, find pressure capacity of the model, and observe its failure mechanisms. This report documents a comparison of the pre-test analyses with the test results and describes the posttest analyses performed to improve the simulation of model behavior.

The pretest and posttest analyses described herein were performed by ANATECH Corp. under contract with SNL. The current work represents the third phase of a comprehensive PCCV analysis effort. The first phase consisted of preliminary analyses to determine what finite element models would be necessary for the pretest prediction analyses, and the second phase consisted of the pretest prediction analyses. The principal objectives of the posttest analyses are: (1) to provide insights to improve the analytical methods for predicting the structural response and failure modes of a prestressed concrete containment, and (2) to evaluate by analysis any phenomena or failure mode observed during the test that was not explicitly predicted by analysis.

The first two chapters summarize the events of the high pressure LST, including the observed failure modes and corresponding pressures and a final set of analyses conducted immediately prior to the test, but after publication of the formal pretest analyses in [1] and [2]. The ABAQUS general purpose finite element program with the ANACAP-U concrete and steel constitutive modeling modules were used for the analysis. Tendons and their prestressing were modeled to replicate expected tendon stress-strain behavior and friction effects. Concrete cracking was simulated with the "smeared crack" approach, where cracking is introduced at the finite element integration points. The failure predictions consisted of liner tearing locations, all occurring near the midheight of the cylinder near penetrations and weld seams with "rat-hole" details. The most likely location for the liner tearing failure was predicted to be near the Equipment Hatch (E/H) at the ending point of a vertical T-anchor, near where the liner is attached to the thickened liner insert plate. The failure pressure was predicted to be 3.2 times the design pressure (Pd) of 0.39 MPa or 1.27 MPa. During the LST, liner tearing and leakage failure was first detected at a pressure of 2.4-2.5 Pd, and a subsequent increase in pressure to 3.3 Pd resulted in further tearing at many strain concentration locations and increased leakage. Subsequent chapters compare measured strains near as many of these strain concentrations as possible to the predictions from local analyses, and also describe reanalysis of existing models and new analyses, such as liner seam models aimed at simulating some of the model's as-built conditions.

The models that constituted the final pretest predictions were the global axisymmetric, the semi-global three-dimensional cylinder midheight (3DCM) model, and local penetration models of the E/H, Personnel Airlock (A/L), and Mainsteam (M/S) penetrations. The local failure predictions were all driven by response versus pressure histories calculated by the 3DCM model. The only changes made between the 1999 pretest predictions reported in [1] and the final (2000) pretest predictions were to material properties and prestressing levels. Because visual inspection of the model revealed the existence of micro-cracking (probably due to curing and shrinkage) throughout the cylinder, the concrete tensile strength was reduced to a cracking strain of $\varepsilon_{cr} = 40 \times 10^{-6}$, based on prior experience with similar test structures. A new suite of concrete compressive tests became available in February, 2000, so these were also incorporated into the final pretest analyses.

ANATECH was also tasked with reviewing and correcting measurements taken during the LST. This effort focused on identifying artifacts in the response data resulting from uncontrollable, external influences on the model and those that

---

[1] This work is jointly sponsored by the Nuclear Power Engineering Corporation and the U.S. Nuclear Regulatory Commission. The work of the Nuclear Power Engineering Corporation is performed under the auspices of the Ministry of Economy, Trade and Industry, Japan. Sandia is a multiprogram laboratory operated by Sandia Corporation, a Lockheed Martin Company, for the U.S. Department of Energy under Contract Number DE-AC04-94AL85000

were a byproduct of the instrumentation. The effects and phenomena addressed in the "data correction" effort were ambient temperature variations, rigid body motion of the model, and strain localization. The details of these corrections are described in the test report; however, the phenomena and corresponding corrections are summarized in Chapter 3.

In reviewing the PCCV test data, the 55 Standard Output Locations (SOLs) used for the Round Robin prediction exercise held in 1999 were very useful comparison points. In Chapter 4, the published and final pretest analyses are compared to the test data at each SOL. All analysis data curves were "rezeroed" to the first point of the test data, i.e. the data reading occurring at the start of the test. This slightly shifted the analysis data, but it simplified the comparison of the response to internal pressure and eliminated differences in the response to dead load and prestressing and that could occur from creep or other time-dependent effects. This is justified because most of the PCCV instrumentation was initialized in March, 2000; after dead loads were applied, the model was prestressed, and subjected to six months of daily temperature cycling and low- pressure testing prior to the start of the LST (September, 2000).

The overall conclusions from the comparisons of the pretest analysis with the LST are as follows:

- Radial displacements in the cylinder wall were well predicted by global axisymmetric analysis, but dome and overall vertical displacements were significantly overpredicted.
- Wall-base juncture behavior, including many rebar and liner strain measurements, were well predicted by the detailed wall-base juncture (axisymmetric) modeling.
- Functional failure (i.e. leakage in excess of 1% mass/day) at a pressure of 2.5 Pd occurred at a liner tear in an area of high strain that was not predicted by analysis, but was probably amplified due to defects associated with weld seam repair.
- Maximum pressure, 187.9 psig (3.30 Pd), which was primarily the onset of global yielding, was closely predicted by analysis, but the predicted failure mode itself did not manifest. Note that the maximum pressure achieved during the LST was also limited by the capacity of the pressurization system to balance the increasing leak rate after functional failure occurred.
- The average radial displacement at the midheight of the cylinder of 20mm at maximum pressure, equivalent to an average hoop strain of 0.37%, is within 10% of that predicted by global analysis (21.9 mm or 0.41%).
- Maximum radial displacement at E/H = 29mm, equivalent hoop strain of 0.0054, was reasonably predicted by 3DCM model, but prediction of displacements at other azimuths–like the buttresses–were poorly predicted by 3DCM model.
- For both the hoop and vertical tendons, there was about 8% to 10% loss of stress between the initial prestressing and the start of the LST caused by long-term effects and by the SFT and SIT.
- Hoop tendon stress distribution simulated by analysis at start of LST shows fair agreement with measurements, implying that the angular friction and anchor set modeling assumptions at the start of the test were reasonable. Vertical tendon stress distribution at the start of the LST were less consistent with the initial modeling assumptions. One tendon, V85, showed significant friction losses below the springline, and the other two instrumented vertical tendons showed only about half of the friction loss in the dome than what was assumed by designers and incorporated in analysis.
- Hoop tendon stress distributions during pressurization showed poor agreement with the pretest analysis. In particular, the gages interior from the ends are underpredicted *and* the anchor forces are overpredicted.
- The cylinder hoop tendon data, in total, shows evidence of the tendons slipping during pressurization. The measurements indicate that the shape of the tendon stress profile completely changes during pressurization. Comparing the increase in the tendon strain to the cylinder hoop strain implies that portions of the tendons are slipping (i.e. tendon strain is greater than the cylinder wall strain) in order for the higher deformation at other azimuths to be accommodated.

Chapter 5 describes the global posttest analyses performed after the LST. To summarize the conclusions:

- Basemat uplift and dome displacements comparisons were significantly improved by redistributing soil basemat springs according to tributary area, improving the dome meridional tendon representation to account for the added stiffness of the overlapping tendons due to the rectilinear "hairpin" layout.
- Comparisons were also improved by using no vertical tendon friction in the cylinder.
- Analysis should not use the "Prestress Hold" option in ABAQUS.

Chapter 6 describes the posttest 3DCM analysis. In the pretest analyses, the 3DCM model was developed to investigate the non-axisymmetric behavior of the cylinder wall and provide more realistic boundary conditions for the penetration's submodels. Buttresses above and below the 3DCM model boundaries have vertical beam stiffnesses that were not accounted for in the pretest analysis. Equivalent spring properties were derived and then applied as radial spring elements. The derivation was performed by adding a 2D plane stress representation of a buttress to the axisymmetric model. The model was then cut at the appropriate 3DCM model horizontal boundary. Zero rotation boundary conditions were applied at the cut boundary and horizontal and vertical tendon prestress was maintained as in the full axisymmetric models. A horizontal displacement was then applied to the cut boundary. Separate models were analyzed with and without the buttress present and the force versus displacement results were differenced; these became the force versus deflection properties assigned to the buttress springs. The only other modeling assumption found to be at significant variance with observed test behavior was the tendon modeling, especially the representation of friction. A lengthy study and series of analyses focused on this variance. Two important observations were made about the hoop tendon measurements as pressure increases:

1. When pressure overcomes prestress, P = 0.59 MPa, tendon stress distributions change from the classical angular friction design assumption to an approximately uniform distribution; then they stay fairly uniform at most higher pressures. Toward the end of the test, some tendon interior forces slightly exceed the force at the anchor.
2. The apparent strain increases in the tendons corresponding to the force/strain gage readings are significantly larger (e.g. 0.48% versus 0.35%, for H53) than the strain that corresponds purely to radial expansion. This can only be explained by force redistribution associated with sliding. Thus the position of the tendon relative to the concrete must be allowed to change after initial prestress in order to adequately simulate tendon behavior during overpressurization.

These observations led to changes and studies of the tendon friction modeling in the 3DCM model. Because the tendon friction behavior observed in the test turned out to be quite complex, the analysis strategies investigated were chosen to at least bracket the observed LST behavior. The last three analyses presented are:

Model 6. Apply prestress. Then, by using the ABAQUS *MODEL CHANGE capability, fix the tendon nodes at their initially deformed position relative to the concrete. In other words, start from classical design prestress with friction and then grout (bond) the tendons.

Model 7. Perform run 5 (the run with only the buttress springs added) up to P = 1.5 Pd (0.59 MPa), then "MODEL CHANGE" all friction elements to non-friction elements (truss ties aligned perpendicular to the tendons. In other words, at P = 1.5 Pd, perfectly grease (unbond) the tendons).

Model 9. After prestress, keep the initial friction elements, but add a new set of friction elements in the reverse orientation so that if points on the tendon move relative to concrete in the reverse direction from that of initial prestress, they will experience reverse direction friction.

In general, the tendon friction simulation runs 6, 7, and 9 show progressively better agreement with test measurements, with run 9 showing quite good agreement at the anchors and at most points interior to the tendon ends. Based on these and the other observations, the results of run 9 were used to drive the submodels for E/H and M/S (and estimated feedwater (F/W)) penetrations posttest analysis. On tendon friction behavior, the test measurements and analytical evidence support the conclusion that tendon friction is important to the tendon behavior, but traditional friction design formulas that predict tendon stress distribution begin to break down once pressurization exceeds the pressure that overcomes prestress (in this case, roughly 1.5 Pd). The coefficient of angular friction appears to lessen, allowing sliding and force redistribution as the vessel expands, but more importantly, some parts of the tendon are forced to reverse direction of travel relative to the duct, reverse it from the direction of travel experienced during prestressing. Under this action, angular friction properties probably still hold, but the direction of friction must change sign from that assumed in a design calculation.

Chapter 7 describes the posttest analyses of the penetration submodels. Liner strains measured in the vicinity of the E/H penetration collar were much lower than predicted by pretest analysis. Since the predicted high strain locations were fundamental to the failure predictions, significant effort was spent reanalyzing the E/H model after the test. With a set of changes that included conversion of the model to the other side of the hatch (away from the buttress) and a correction to the vertical stress boundary condition, posttest E/H model's hoop expansion behavior correlated much better with measured global displacement behavior. The hoop deformation correlation-to-pressure function introduced in the pretest work was no longer needed. Two hypotheses were developed.

Hypothesis 1: The liner in the E/H area had a high degree of bond-friction with concrete, preventing slippage of the liner relative to the concrete; relative slippage is required for elevated strains to develop near local discontinuities like T-anchors and stiffeners.

Hypothesis 2: Formation of a major crack near the edge of the E/H embossment further concentrated the liner strains at the edge of the embossment.

Posttest analysis showed that by preventing relative slip between liner and concrete, the overall behavior of the system (concrete strains, tendon strains, liner strains away from the hatch) remained the same, but the elevated strains close to the collar were eliminated. In the final case, directed cracks were introduced to one row of elements, and a discrete crack was formed by adding double rows of nodes along an assumed crack line. This was found to create an elevated liner strain phenomenon. The mild strain concentration coincides, in location, with rat-hole weld seam details, and in the LST, numerous tears occurred at these details. Based on results of detailed liner rat-hole analysis (Chapter 8), the additional strain concentration associated with these details is enough to generate liner strains at the edge of the embossment in excess of the liner tearing strain criteria. This shows that with discrete crack modeling and local rat-hole modeling, a liner tear could have been predicted to occur as early as 2.8 Pd. Based on the evidence provided by liner strain gages and by acoustic monitoring, one of the tears along this embossment edge may have even occurred as early as 2.5 Pd. (Note that this posttest analysis did not attempt to include as-built liner defects, such as local thinning or residual stresses resulting from initial fabrication or subsequent repairs.) The posttest E/H study thus presents a modeling strategy with results that correlate well with the LST measurements and observations. A somewhat higher strain prediction might be possible if a discrete crack (separate rows of nodes) were propagated all the way through the concrete wall, but this would require a change in rebar modeling strategy–one that is probably not practical even for detailed analysis of containments.

The M/S and F/W penetration hot spots (both analysis and LST observations) occurred near the vertical T-anchor terminations and near the 'equator' of the thickened insert plate surrounding the penetration group, i.e. at the 3:00 and 9:00 positions. For the posttest analysis effort, no changes to the M/S model were necessary, other than updating the applied displacement versus pressure histories that were obtained from 3DCM posttest Model 9. After studying the F/W geometry in the posttest phase of the project, it was determined that the F/W penetration model was so similar to the M/S penetration model that it was not necessary to pursue separate analysis of the F/W model; the posttest M/S model analysis was assumed to be reasonably representative of the F/W penetrations. Several observations could be made from the well-instrumented M/S and F/W locations that are relevant to response predictions around containment penetrations.

- Many of the highest strains recorded during the LST are near the M/S and the F/W.
- There is wide variation in peak strain measurements, even at locations that are theoretically identical in geometry; factors contributing to these differences are: slight variations in liner thickness (due to manufacturing and weld repair grinding), gage position relative to the collar/weld, material properties (including welding heat effects), etc.
- The highest strain measurements can, but do not always, correspond to tear locations. Examples supporting this are: 1) a gage near the F/W tear shows evidence of rising strain prior to tear occurrence, then starting at 2.9 Pd, declining strain due to the stress relief caused by the tear; a gage located near the crack tip, on the other hand, showed quite low strain up to 3.1 Pd and then a sudden jump. This supports a hypothesis that this tear initiated at a pressure of 2.9 Pd at about the 7:30 position (midpoint of the tear) and then between 2.9 Pd and 3.1 Pd, the tear ran around the perimeter of the thickened collar and up to the 9:00 position.

Comparisons of analysis to the M/S and F/W liner strain gages show that the posttest analysis of the M/S penetrations captures the strains measured in the LST quite well for both the M/S and F/W penetrations.

Chapter 8 describes the investigation of the liner tears that occurred away from the penetrations but where welding details may have caused local liner strain concentrations. The PCCV model exhibited 16 distinct locations at which liner tears occurred. All 16 locations were near vertical weld seams, but with some variation in the presence or configuration of a horizontal stiffener or rat-hole. By comparing "before and after" photos taken by SNL and with reference to a posttest metallurgical study [7], it was observed that liner welding irregularities were present at almost all of the tear locations. These irregularities included points of extensive repair, such as grinding, points of discontinuous or missing back-up bars, or points with weld and liner seam fit-up irregular geometry. Some locations, where a seam and rat-hole existed and high strains were measured, but a tear did not occur (e.g., at Location D-7, just below where tear 16

occurred), provide additional evidence of the importance of the welding details to liner tearing. Visual observation showed extensive grinding and weld repair in the liner welds where most of the tears occurred. Ultrasonic measurements showed substantial reductions in thickness near these tears. Measurements showed ~23% thickness reduction in many locations, and more (up to 40% in a few locations). A posttest liner seam analysis study was aimed at answering questions about quantifying the effects of welding irregularities and distinguishing these from strain concentration effects solely related to geometry. A mesh-size sensitivity study was conducted. Analyses were then conducted to assess the effects of material and geometry variations. The first variation was to implement varying material properties near the weld areas. This included assignment of different material properties to the base metal, heat affected zone (HAZ), and weld fusion zone (WFZ) regions of the model. The second variation only modified the material in the WFZ. The final phase incorporated geometry modifications to the model near the weld lines. This included thinning of elements and varying the extent of thinning in the vicinity of the welds due to grinding. The geometry modifications were coupled with modified material properties ranging from uniform to including variations of base metal, HAZ, and WFZ regions. All of the material and geometry variations were based on the data contained in the SNL metallurgical analysis report [7]. The conclusions of the liner seam/rat-hole modeling study are summarized below:

- By comparison with strain gage measurements and posttest liner tear observations, some of the finite element weld seam analyses are able to generate strain fields in and around the rat-holes and liner welds which exceed the liner tearing strain criteria at locations where tears were observed.
- Because of competing mechanisms (between the weld zone and the ends of stiffeners), making yield and ultimate strength adjustments to the HAZ material properties appears to be justified and necessary to correctly predict strain concentration location and intensity.
- The models with back-up bars, nominal geometric properties, and best-estimate material properties yielded the best simulations of defect-free construction of rat-hole/weld-seam details, represented in the PCCV model at locations D7 and J5. However, even models without back-up bars also provided reasonable correlation with gages at these locations.
- A case with severe (~40%) amounts of thinning appears to provide the best simulation of the behavior of tear occurrences in which severe liner thinning (due to weld repair grinding) was reported in [7] to be present and back-up bars were absent; these conditions existed at tears 7, 8, 10, 12, 13, 14, 15, and 16.
- A case specifically representing the "tear 16" detail was performed. This case appears to provide reasonable simulation of the tears that occurred *with* back-up bars present, namely, tears 1, 2, 6, 9, 11, and 16. The severity of the strain at this case also shows that a tear ($\varepsilon_{eff} > 20\%$) at the geometry simulated would have been predicted to occur as early as 3.0 Pd.
- If a section of liner with a rat-hole/liner-seam detail, such as that at tear Locations 7, 12, 13, and 15 is subjected to additionally elevated strain (i.e. strain across the liner model that is larger than free-field global strain) a tear even earlier than 3.0 Pd can be justified. In practice, such a prediction could approximately be made using a strain concentration factor approach. The strain concentration factors (K = peak ε_{eff} divided by global ε_{hoop}) implied by this liner seam study are as follows: K = 48 (tear at stiffener end, no back-up bar); K = 45 (tear at stiffener end, with back-up bar); K = 59 (tear at HAZ, no back-up bar, and 40% thickness reduction due to grinding); K = 91 (tear at tear 16, if a short segment of horizontal weld seam back-up bar is missing)
- Using a model of the rat-hole/seam locations without defects, such as location D-7, showed that liner tears still would have developed by pressure of 3.4 Pd, so liner tearing and leakage would still have been the failure mode (for quasi-static pressurization) even in the absence of liner welding irregularities.

The LST resulted in liner tearing and leakage, but not a structural failure. Structural damage was limited to concrete cracking, and the overall structural response (displacements, rebar and tendon strains, etc.) was only slightly beyond yield. (Global hoop strains at the midheight of the cylinder only reached 0.4%, approximately twice the yield strain in steel.) In order to provide additional structural response data to compare with in-elastic response conditions, the PCCV model was resealed, filled nearly full with water, and repressurized during the SFMT to a maximum pressure of 3.6 Pd when a catastrophic rupture occurred. Chapter 9 includes a brief discussion and comparison of the pretest and post-LST analysis results to the SFMT data and presents the results of a post-SFMT analysis intended to provide some insight into the mechanisms leading to the structural failure.

The SFMT posttest analysis showed that good simulation of the PCCV global behavior through and including tendon rupture is possible with a 3D shell model. The main limitations of the shell model were a lack of local liner strain concentration prediction and a lack of accuracy in the predictions of local wall-base-juncture behavior. However, significant accuracy in global behavior prediction did not seem to be lost when a bonded tendon assumption was used.

The SFMT model provided additional insight as to how the structural failure likely developed. Near the 0 degrees - 6 degrees azimuth of the cylinder, there is a discontinuity of a step-down in inner and outer hoop rebar area of 38% (step-down from alternating D19, D16 bars to a pattern of 1D16/3D13 bars). Then at 3.49 Pd, the wall and tendon strain at the 0 degrees - 6 location is a little higher than all other azimuths, and a tendon rupture occurs. Once this occurs, the analysis shows neighboring tendons rupturing and deformations spreading quickly along this azimuth. It is interesting to note that the analysis predicts that the secondary tendon ruptures spread upward. Shortly after the first rupture at 5.4 m, analysis predicts the tendon ruptures to spread up through 6.5 m. From review of the test video, this appears to agree with observations. By 3.65 Pd, the analysis shows rupture to have spread over a vertical line spanning about 6 m. This also agrees with observations. After wall rupture, a secondary event occurred in the SFMT: through-wall failure around the circumference of the wall at about 1.5 m elevation. While it is difficult to say at what azimuth this failure initiated, it seems clear that this was a shear or combined shear/flexural failure of the wall. The plotting of analysis shear results showed that such failure may have initiated at the buttresses (evidenced by the high shear stresses predicted there) and then "unzipped." Note from the plans that at elev. 1.60 m, there is a step-down in vertical rebar from D19 to D16, which may have focused this shear failure plane. Moreover, at the buttresses, the outer vertical rebar step down occurs slightly lower: at 1.22 m there is a change from a total of nineteen D19 bars down to a total of ten D19 bars placed within the buttress. This may explain why the circumferential failure ran through the buttresses at a slightly lower elevation than the rest of the wall. As a point of comparison, the shear failure threshold calculation performed in the pretest work [1] is compared to the demand (both pretest axisymmetric and posttest SFMT) in Chapter 9. This shows that without the trigger of rupture of the vessel, the capacity (a modified compression field theory calculation) exceeds the demand throughout the pressurization. But with the triggering event of a massive wall rupture, one of two mechanisms may have caused shear demand to exceed capacity: 1) a large deformation of the wall opening, creating large rotations near the base of the wall, would crush the outer concrete of the flexural section and thereby reduce the capacity, or 2) the water jet-induced momentum imbalance would cause added shear demand; this would create tangential shear at some azimuths and would be the maximum at the buttresses; such shear acting in combination with the already high radial shear stresses could have increased shear stress demand enough to induce the shear failure.

The 1:4 scale PCCV test showed the driving response quantity that leads to the limit state of the vessel is the radial expansion of the cylinder. This aspect of response must be predicted correctly in order to reasonably predict vessel capacity and predict, at least approximately, the many other local aspects of response (local liner strains, etc.) that are driven by the cylinder expansion. With this test, as with the 1:6 scale PCCV model, many competing strain concentrations occur around the mid-height of the cylinder. Although it is difficult to predict which local liner detail will tear first, and although some particular response quantities, like basemat uplift, were not predicted exactly by the ANATECH/SNL pretest analysis of the PCCV model, the radial expansion of the cylinder was predicted very accurately. A response mechanism that also appears to have been well predicted was cylinder wall-base flexure and shear, another mechanism that, if predicted grossly incorrectly, could lead to erroneous pressure capacity/failure mode conclusions.

The minimum requirement for a containment overpressure evaluation should certainly be a robust axisymmetric analysis. Other steps, guidelines, and lessons learned are provided in the final chapter of this report. The lessons learned in the current work, which are perhaps the most novel, are those related to tendon friction behavior. As a result of this project, the best calculation methods recommended for tendon friction modeling are, in descending order of preference, 1) an advanced contact friction surface between the tendons and the concrete (not manageable for the current problem size and complexity), 2) pre-set friction ties applied in one direction during prestressing and then added in the other direction during pressurization (3DCM run 9) and 3) if neither of these methods are practical within the scope of the calculation, it is best to start with an "average" stress level (using a friction loss design formula), but assume uniform stress distribution in the tendons throughout pressurization, i.e., an unbonded tendon assumption, and finally 4) same as 3, but using a bonded tendon assumption. It should be recognized for method 4, however, that this can lead to a premature prediction of tendon rupture, because the tendon strain increments during pressurization will match the hoop strain increments of the vessel wall one-to-one, and this was not observed during the PCCV LST.

The relevance of this work to full size U.S. Containments is fundamental. All of the analysis methods tried, calibrated, and validated would be highly applicable to full-scale structures. The posttest work also provides a reasonably simple liner-only mesh approach to predicting local strains near weld seams, and the test itself underscores the need for continuous back-up bars on all liner seam welds. Such is the requirement in the current U.S. design rules.

ACKNOWLEDGMENTS

This pretest analysis effort was sponsored by the U.S. Nuclear Regulatory Commission. The authors would first like to thank Dr. James F. Costello of the NRC for his technical interaction and support throughout the program.

The work described herein was performed by ANATECH for Sandia National Laboratories in Albuquerque under Contract No. AO-5464. Reviews of the posttest analysis plan and the analysis results have been conducted by Mike Hessheimer and other Sandia personnel. The valuable discussions and guidance received during those reviews were critical to the development and presentation of the results. It should also be noted that the analytical models and software developed by ANATECH for the Electric Power Research Institute (EPRI) in their Containment Integrity Program were made freely available by EPRI and proved to be indispensable in the performance of this work.

ABBREVIATIONS

3DCM	entire cylinder midheight region
A/L	airlock
BPS	before prestressing
CIRC	circular cross section
CTL	Construction Technology Laboratories
DOR	data of record
DYN	"dynamic" data
E/H	Equipment Hatch
F/W	Feedwater
HAZ	heat affected zone
LST	Limit State Test
M/S	Mainsteam
NRC	U.S. Nuclear Regulatory Commission
NUPEC	Nuclear Power Engineering Corporation
PCCV	prestressed concrete containment vessel
PSFT	Post System Functionality Test
SFT	System Functionality Test
SFMT	Structural Failure Mode Test
SIT	Structural Integrity Test
SNL	Sandia National Laboratories
SOL	Standard Output Locations
UTS	Ultimate Tensile Strength
WFZ	weld fusion zone

1.0 INTRODUCTION

1.1 Background Leading up to the Limit State Test

Sandia National Laboratories (SNL) is conducting a research program to investigate the integrity of nuclear containment structures. This program is cosponsored by the Nuclear Power Engineering Corporation (NUPEC) of Japan and the U.S. Nuclear Regulatory Commission (NRC). As part of the program, NUPEC constructed a 1:4 scale model of the prestressed concrete containment vessel (PCCV) of a Japanese pressurized water reactor (PWR) plant at SNL's Containment Technology Test Facility in Albuquerque, NM. The model is shown in Figures 1-1 and 1-2. SNL designed and installed an extensive suite of instrumentation during and after the construction of the model and conducted a series of overpressurization model tests leading to both functional and structural failure. One of the key program objectives was to validate methods for predicting structural performance of containment vessels when subjected to beyond-design-basis loadings, such as very high internal pressurization. The NRC-sponsored analysis effort to achieve this objective included 2D and 3D nonlinear finite element modeling of the PCCV model. Such analyses were performed using the nonlinear concrete constitutive model, ANACAP-U, in conjunction with the ABAQUS general purpose finite element code [5]. The analysis effort was conducted in three phases:

1. Preliminary Analysis,
2. Pretest Prediction, and
3. Posttest Data Interpretation and Analysis.

The purpose of the preliminary analysis was to provide a basic understanding of the model response for program planning purposes and to define the scope of the pretest analysis. The preliminary analysis results were not formally documented; however, a summary paper was published [2], and the results are reflected in the pretest analysis that followed. A list of possible failure modes and locations was developed in the preliminary analysis phase prior to conducting the formal pretest analyses. Some of the potential failure modes were specifically addressed by the global analysis, while others were addressed by local models. The results of the preliminary analyses indicated that a liner tearing failure at the midheight of the cylinder near a penetration and a shear/bending failure at the base of the cylinder wall were both found to have a significant probability of occurrence. Recommendations were then made for the pretest analyses, including model refinements and the development of local models to better predict the sequence of competing failure modes were identified.

The principal objectives of the pretest analyses were to (1) exercise advanced analytical methods for predicting structural response of a prestressed concrete containment, (2) gain insight into potential structural failure modes of a prestressed concrete containment, and (3) support planning of test procedures and instrumentation. One requirement of the program was that the pretest analysis predictions be completed and published [1] prior to the high-pressure Limit State Test (LST) of the PCCV model, which was conducted in September, 2000. This meant that the pretest prediction analyses must be completed many months prior to the test. For this reason, the published pretest analysis predictions did not include certain as-built features, actual measured prestressing and associated losses, or creep and temperature effects. Prestress values, losses due to friction, anchor set, and concrete creep were approximated from the assumptions used in the PCCV model design.

In addition to a detailed axisymmetric global model, local models developed for the pretest analysis included: the Equipment Hatch (E/H) region, the Personnel Airlock (A/L) region, and the Mainsteam Penetration (M/S) region. A detailed 3D model of the entire cylinder midheight region (3DCM) was also developed to investigate tendon behavior in the cylinder and 3D effects that drive the local strain concentrations near the penetrations. A highly detailed representation of the wall-basemat juncture region was also added to the 2D axisymmetric model, making total of five pretest analysis models. The pretest analyses described herein were also the basis of the SNL/ANATECH submittal to an international Round Robin Pretest Analysis exercise [3].

The pretest analysis phase of the PCCV model test program refined and demonstrated finite element and material modeling methods and a systematic process for developing pressure response predictions from global 2D, semi-global 3D, and local 3D analysis models. Tendon modeling tasks demonstrated the utility of a new tendon modeling approach in which friction losses are explicitly represented by friction truss tie elements. Tendon stress distributions at various pressures were provided as benchmarks of expected tendon behavior. Capturing the tendon stress distributions in more

detail refined the prediction of displacement response and liner strains, especially near the E/H, where this distribution is very complex. **The 3DCM model, with its detailed tendon representation, predicted the rupture of hoop tendons closest to the E/H at a model pressure of about 3.5 Pd. However, this mode was predicted to be precluded by the liner tearing and leakage failure mode.**

Using a strain-based failure criteria that considered the triaxiality of stress and a reduction of ductility in the vicinity of a weld, a liner failure strain criteria of 16% was established. The failure pressure at which a local analysis computed effective plastic strain that reached the failure strain criteria was 3.2 Pd, or 1.3MPa. The location for this liner-tearing failure was near the E/H, adjacent to a vertical liner anchor that terminated near the liner insert plate transition. Other local models showed other candidate liner tear locations, several of which were predicted to occur during the pressure range 3.2 Pd to 3.5 Pd if they were not precluded first by the growth of the first tear and subsequent depressurization of the vessel. A significant candidate tear location was also found near the 90 degree buttress where hoop strains are elevated due to circumferential bending, and weld seams with hoop stiffener "rat-holes" are coincidentally located. Failure at such locations was predicted to occur shortly after failure at the E/H location.

After publishing the pretest analysis results, a final pretest analysis was performed to refine the pretest predictions using the most current as-built model properties. This final pretest analysis was performed primarily to support test operations by providing the 'best' predictions of the model's response for real-time comparison with the actual response. This information was essential to the safe and successful conduct of the test. Since the results of this final pretest analysis were not published in the pretest analysis report [1], a summary of the results are included in Chapter 2 of this report.

1.2 Limit State Test and Structural Failure Mode Test Overview

The following "quick look" observations written a few days after the test by Mike Hessheimer at SNL provide a concise overview of the LST conduct and PCCV model behavior:

> The PCCV Limit State Test (LST) began at 10:00a.m., Tuesday, September 26, 2000 as scheduled. We began pressurizing in increments of 0.2 Pd, repeating the Structural Integrity Test (SIT) pressure sequence we followed on September 12. We continued pressurizing the model to 1.5 Pd, when we conducted a leak check and calculated a leak rate of approximately 0.5% mass/day after 3.5 hours. Based on our experience during the SIT/ILRT we interpreted this as indicating that there was no leakage.
>
> We proceeded to pressurize in increments of 0.1 Pd until we reached 2 Pd at 22:00 Tuesday evening to conduct another leak check. Since there was no evidence of distress, we continued the leak test throughout Tuesday night and Wednesday morning and calculated at leak rate of >0.1% mass/day after holding pressure for approximately 8 hours.
>
> At 07:00, Wednesday, September 28, we continued pressurizing the model in increments of 0.1 Pd until we reached 2.5 Pd around 10:00. At this point, we observed some liner strains approaching 2% and also had some evidence from the acoustic system that there might have been a liner tear. We continued with the planned leak check at this pressure and after 1-1/2 hours, calculated a fairly stable leak rate of 1.5% mass/day (+/- 0.5% mass/day). We decided that this was clear indication of a liner tear/leak and modified our test plan slightly, continuing to pressurize the model in incremental steps of 0.05 Pd, but reducing the hold time at each pressure step to less than 10 minutes.
>
> We were able to continue pressurizing the model to approximately 3 Pd, with increasing evidence of leakage and increasing liner strains. At 3 Pd, it became difficult to increase pressure so we increased the nitrogen flow rate to 3500 scfm. We were able to increase pressure to 3.1 Pd however the pressure dropped steadily after reaching this pressure. We estimated the leak rate at this point to be approximately 100% mass/day. We then increased our nitrogen flow rate to the maximum capacity of the pressurization system (5000 scfm) and were able to increase the pressure to slightly over 3.3 Pd before the leak rate exceeded our capacity to pressurize the model. Since we could no longer increase pressure and we had almost exhausted our supply of nitrogen, the decision was made to begin terminating the test. The isolation valve was closed and we allowed the model to depressurize on it's own. We estimated that the initial terminal leak rate was on the order of 900% mass/day. (The maximum flow rate of nitrogen, 5000 scfm is equivalent to 1000% mass/day.) As the model

depressurized, we observed a steadily decreasing leak rate (initially decaying at 250% mass/day per hour). We then opened the vent valve to depressurize the model more quickly to 1.0 Pd.

At 1.0 Pd, we were able to inspect the model and observe (hear and feel) nitrogen gas escaping through many small cracks in the concrete and at the tendon anchors. We suspect that the liner acted as a leak chase, allowing nitrogen gas escaping through a tear or tears in the liner to travel between the liner and the concrete until it found an exit path through a crack in the concrete or a conduit in the tendon duct.

At maximum pressure local liner strains approached 6.5% and global hoop strains (computed from the radial displacement) at the mid-height of the cylinder averaged 0.4%. While we observed large liner strains and suspect that the liner may have torn in several locations, the remainder of the structure appears to have suffered very little damage with the exception of more extensive concrete cracking at some locations. There was no indication of tendon or rebar failure.

Plots of the model pressurization versus time, nitrogen flow in versus time, and the flow rates versus time are shown in Figures 1-3 and 1-4. Once the model was depressurized and inspected, a total of 26 liner tears were found at 17 different locations. This observed liner tear map is shown in Figure 1-5. Every tear occurred at or near a vertical weld seam, and some of the tears grew quite large; certainly large enough to account for the depressurization of the model.

Following the LST and post-LST inspection of the model and the data, it became clear that the objectives of the test program were not fully satisfied. Other than concrete cracking, liner tearing, and leakage, the LST did not cause any significant structural damage in the model, and overall structural response (displacements, rebar and tendon strains, etc.) was only slightly beyond the elastic range. In order to provide additional structural response data to compare with inelastic response conditions, the PCCV model was resealed, filled nearly full with water, and repressurized during the Structural Failure Mode Test (SFMT). A maximum pressure of 3.6 Pd was reached when a catastrophic rupture occurred. This was preceded only briefly by tensile failure of several hoop tendons. The condition of the model immediately after the SFMT is shown in Figure 1-6.

1.3 Objectives of Posttest Analysis Work

The scope and objectives of the posttest analysis work are outlined below.

1.3.1 Final Pretest Analysis

A final pretest analysis was performed to support test operations and to account for information (such as tendon prestress levels) learned in the final months prior to the test.

1.3.2 Evaluation of Test Data and Comparison with Pretest Analysis Results

The published and final pretest analysis results are compared to the test data to characterize how well the pretest analyses predicted the behavior and identify areas for improvement or modification in the posttest analyses. In addition to comparing responses for specific transducers, a qualitative assessment on the overall response is also included. Also, the effect of uncontrollable external factors (e.g. variations in ambient thermal response), as well as response artifacts introduced by the instrumentation, were identified and the methods used to 'correct' the data for these effects were developed.

1.3.3 Global Posttest Analysis

The global PCCV axisymmetric model was updated to reflect actual conditions during the LST (e.g., material properties, in-situ stress conditions of concrete and tendons, etc.) and the global model was reanalyzed. The effect of soil stiffness on the basemat and the modeling of the dome tendons were also addressed.

1.3.4 Local Posttest Analyses

The 3DCM model, the local penetration models (E/H, A/L, and M/S), and, to address the liner failure occurrence in some unexpected location, one new model, were developed and analyzed.

1.3.5 Post SFMT Analysis

Selected data from the SFMT was compared to both the pretest and posttest analyses. A simplified 3D shell model was developed to simulate and provide some insight into the sequence of events leading to the catastrophic structural failure.

1.3.6 Posttest Analysis Report

The results of these tasks are documented herein, including a summary of lessons learned and possible analysis methodology enhancements as a result of the PCCV analysis research program.

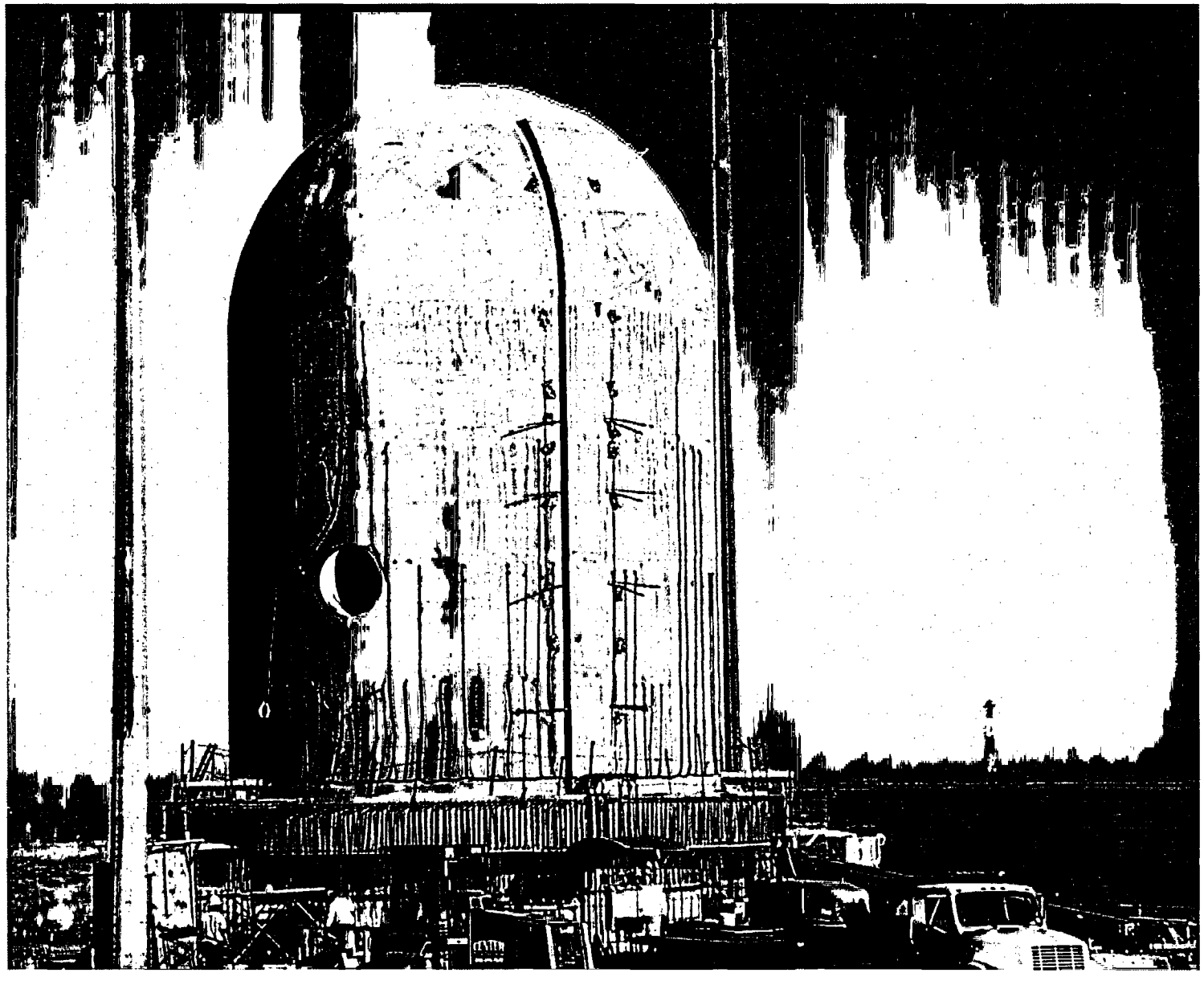

Figure 1-1. NUPEC/NRC 1:4 Scale PCCV Model Built at Sandia National Laboratories

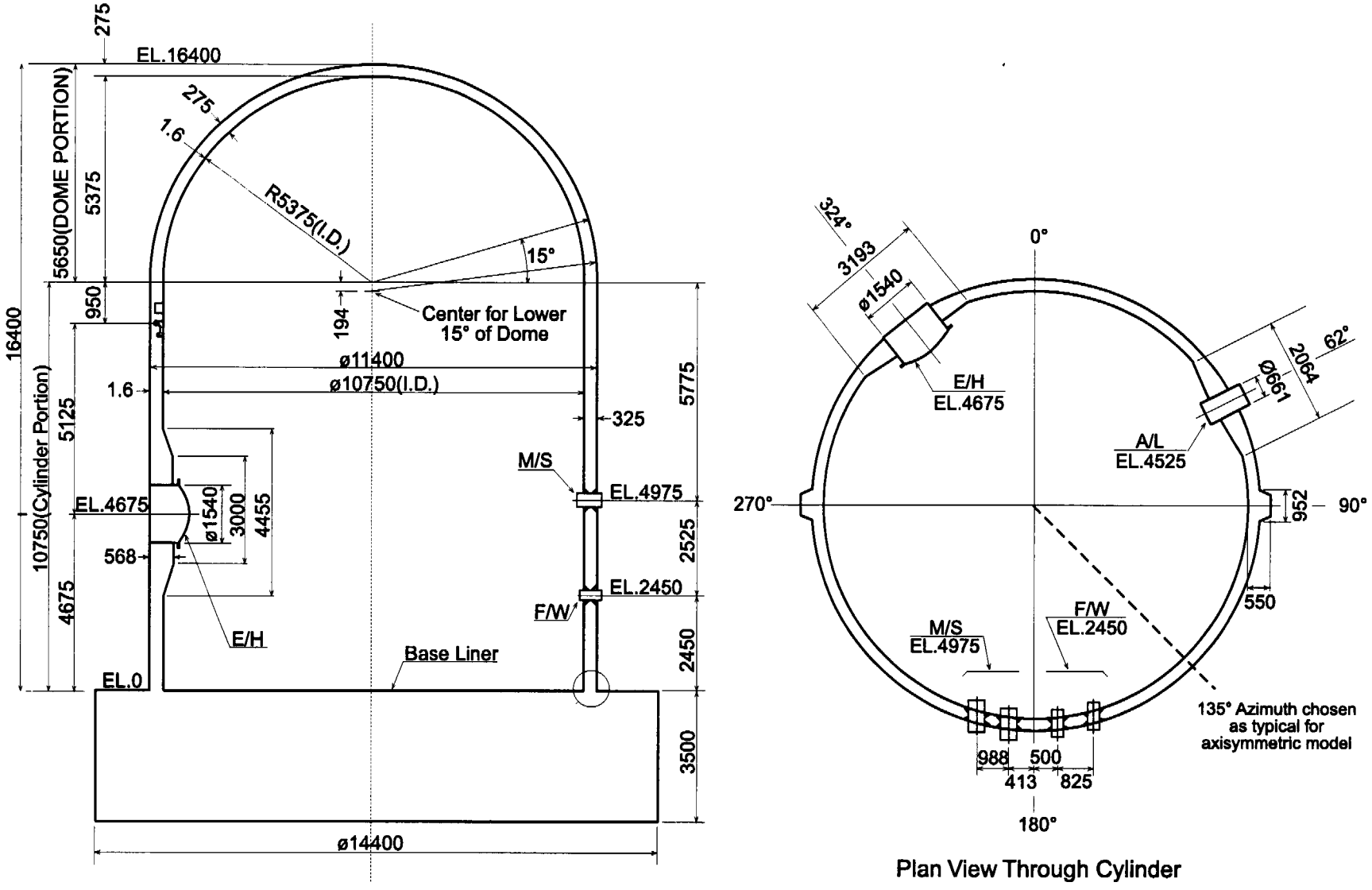

Figure 1-2. 1:4 Scale PCCV Model Geometry (dimensions in mm)

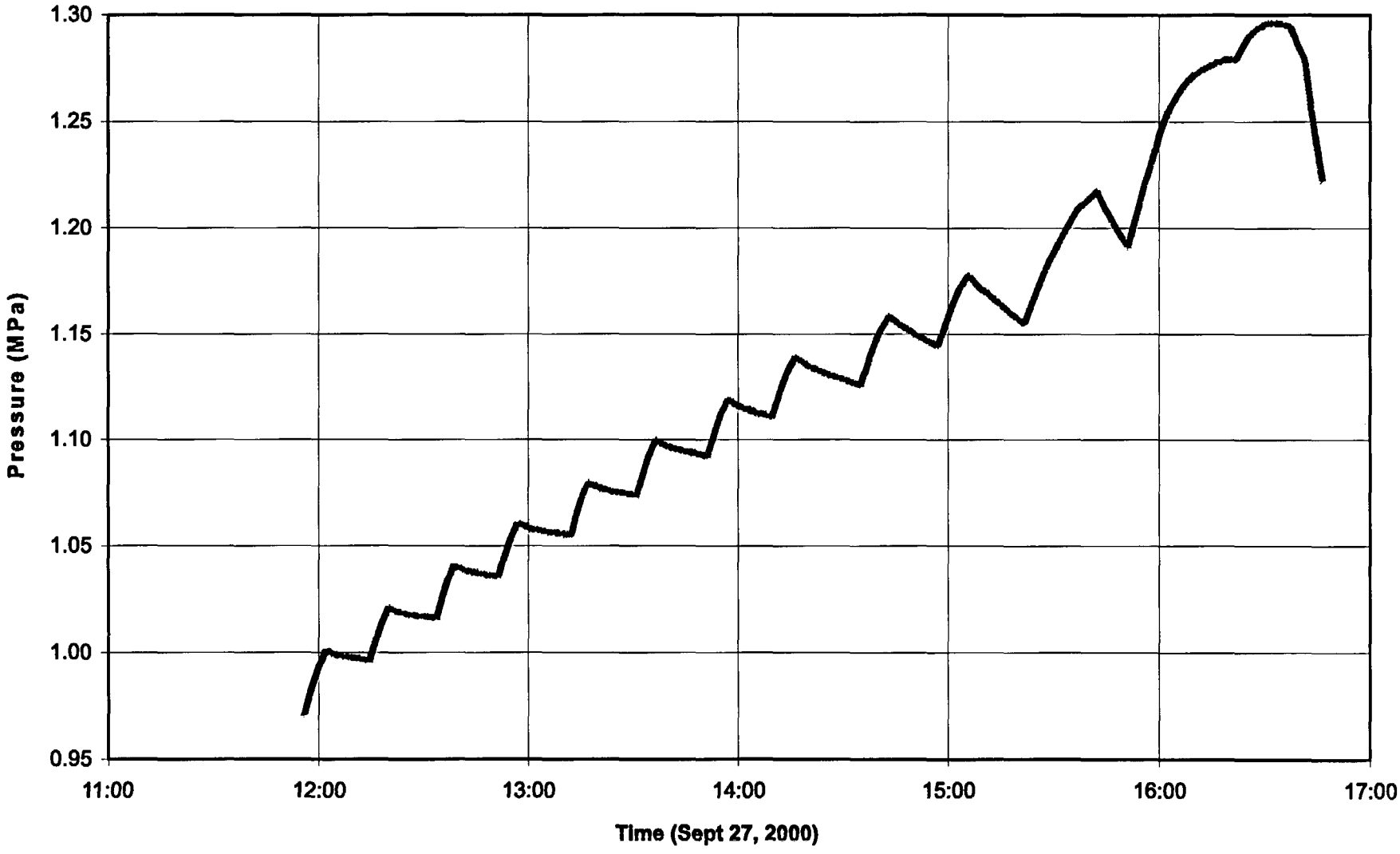

Figure 1-3. LST Pressure Time History (2.5Pd - 3.3Pd)

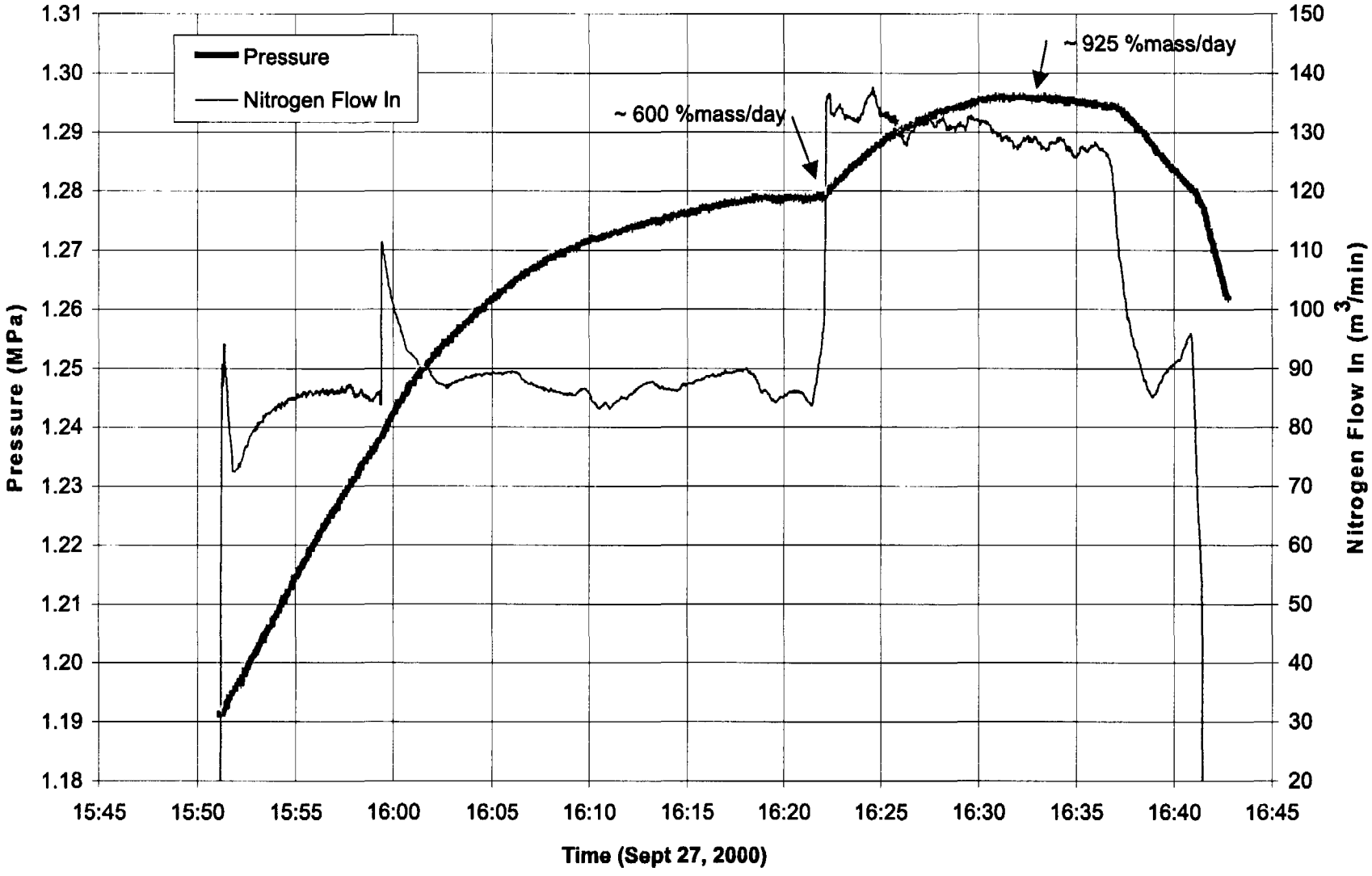

Figure 1-4. LST Pressure and Flow (Final Minutes)

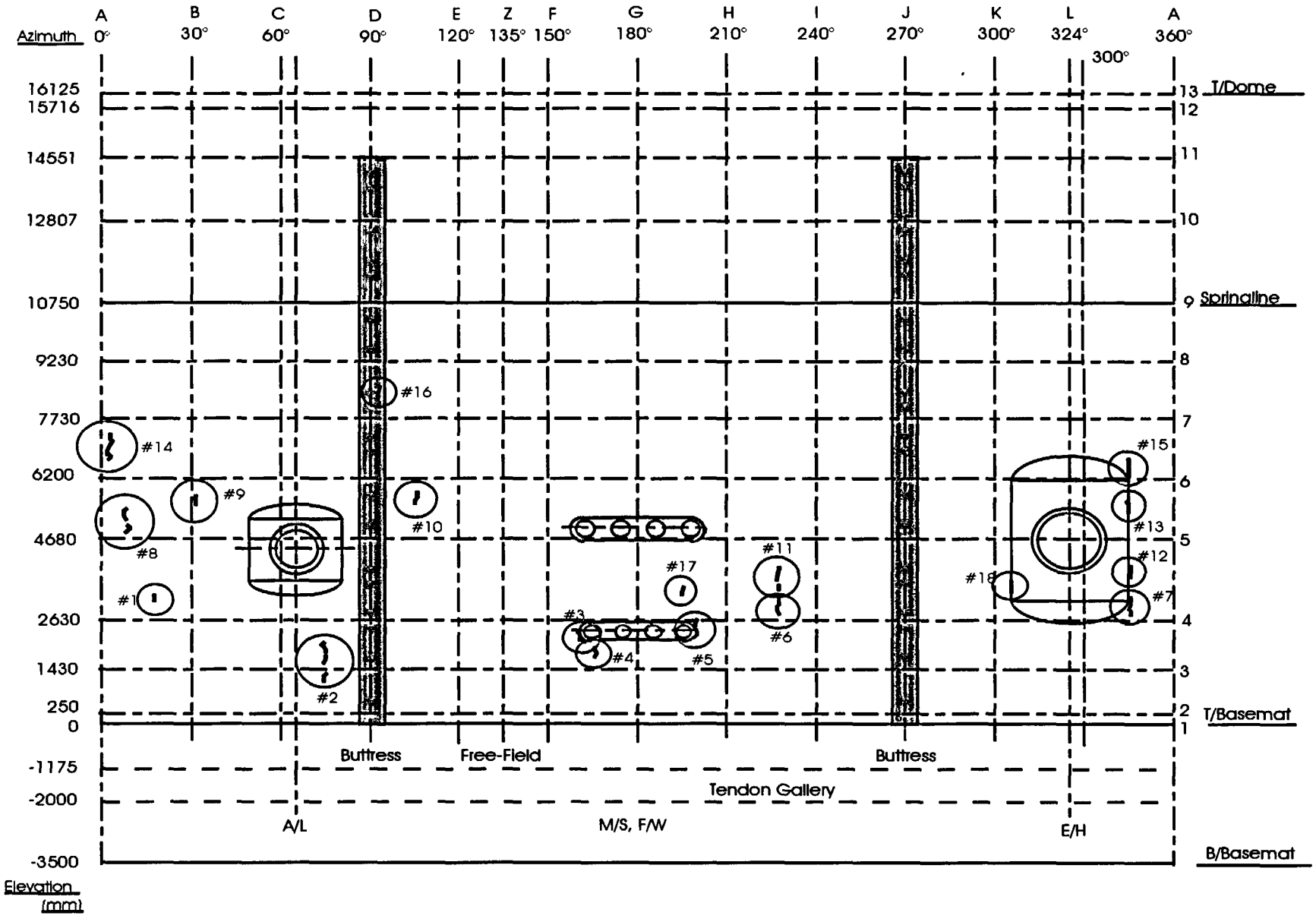

Figure 1-5. Liner Tears Observed After LST

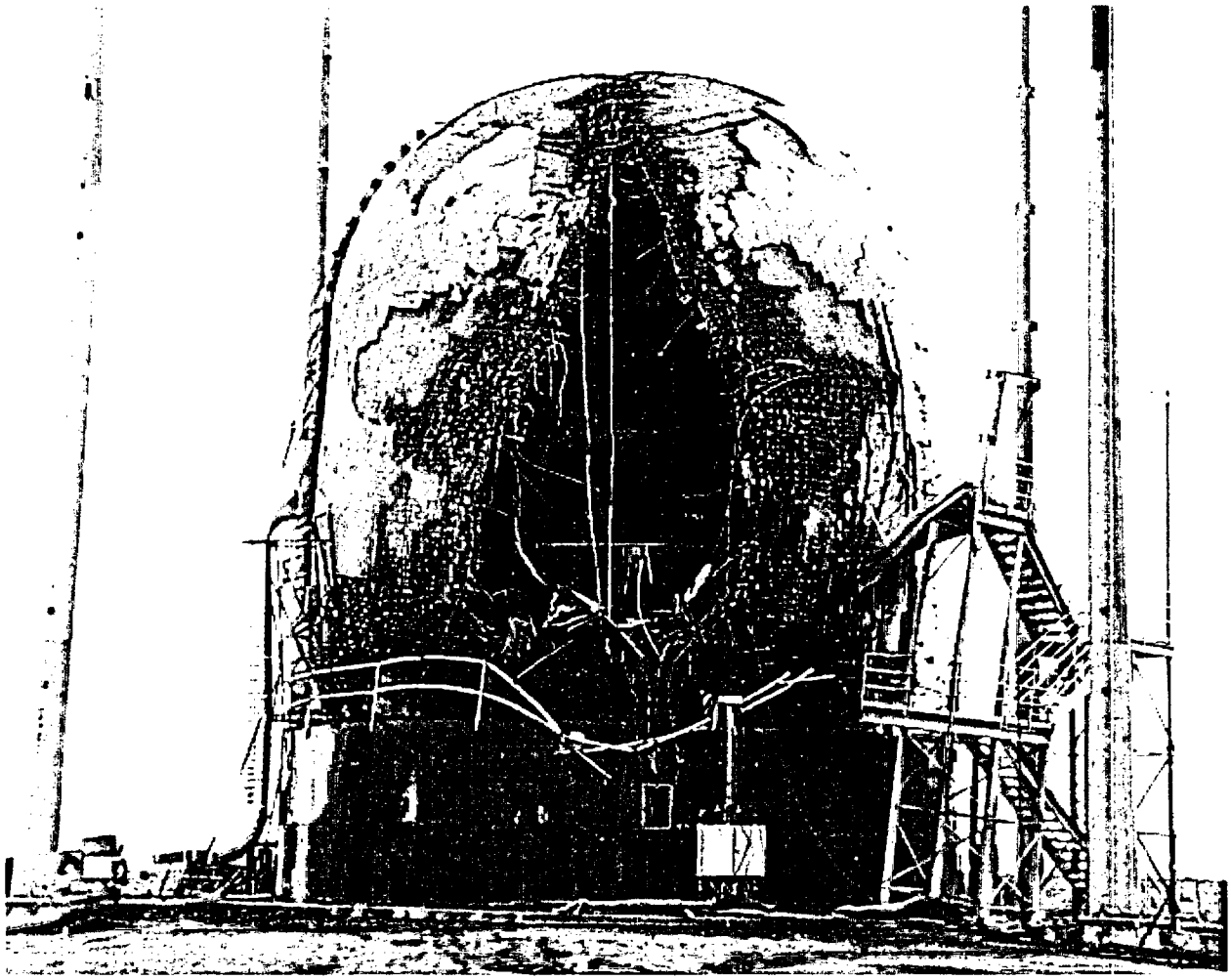

Figure 1-6. PCCV Model after Structural Failure Mode Test

2.0 FINAL PRETEST ANALYSIS

2.1 Scope of Final Pretest Analysis

Pretest prediction analysis of the NUPEC/SNL 1:4 scale PCCV model LST is formally documented in the NUREG CR-6685 Report [1]. Due to the logistics of report preparation and reviewing requirements, the analyses reported therein were performed in the fall of 1999, one year prior to the LST scheduled for September, 2000. A final set of pretest prediction analyses were performed just prior to the test, which incorporated updated properties and in-situ conditions of the model. These final pretest analyses were performed primarily to support test operations by providing the 'best' predictions of the model's response for real-time comparison with the actual response. This information was essential to the safe and successful conduct of the test. The properties and modeling inputs considered for modification were:

1. Concrete material properties,
2. Prestress (stress levels, stress distribution due to friction, and anchor set), and
3. Creep, temperature, and other time dependent effects.

The global axisymmetric, the semi-global 3DCM models, and the local penetration models were reanalyzed. The local failure predictions are all driven by response versus pressure histories calculated by the 3DCM model, but the local models had to be reanalyzed to save the data recently selected for monitoring during the test. How the updated modeling inputs were considered in the final analyses is summarized herein.

2.2 Final Model Inputs

2.2.1 Concrete Material Properties

Because visual inspection of the model reveals the existence of microcracking (probably due to curing and shrinkage) throughout the cylinder, the concrete tensile strength was reduced to correspond to a cracking strain of $\varepsilon_{cr} = 40. \times 10^{-6}$. This is half of the value used in the prior analysis.

A new suite of concrete compressive tests conducted at Construction Technology Laboratories (CTL) became available in February, 2000. The concrete pour designations are shown in Figure 2-1 and the latest test results are tabulated in the CTL test excerpt, Table 2-1. How this data was used in the reanalysis is summarized below.

2.2.1.1 Axisymmetric Analysis

Based on prior analysis, the areas where concrete behavior most influences model behavior are in regions C1 and F3B. A third zone, the rest of the basemat, was also identified separately because of the differences in material specifications for this zone. The zones used for the analysis assumptions are shown in Figure 2-1. The average strengths and moduli assigned for these regions are as follows:

		Region C1	Region F3B	Rest of Basemat
f_c'	=	60.9 MPa (8831 psi)	59.4 MPa (8613 psi)	49.2 MPa (7,134 psi)
E	=	27.1 GPa ($3.93 \cdot 10^6$ psi)	28.0 GPa (4.06×10^6 psi)	26.0 MPa (3.77×10^6 psi)

These figures were computed by averaging the data in Table 2-1, but only using "C1," "F3B," and the average of region "F1," "F2," and "F3A," respectively. The Region C1 and F3B strengths are roughly 22% higher than what was used in the prior prediction analysis, and may, therefore, have a noticeable effect on the cylinder wall flexural behavior. The Young's Moduli are roughly 15% lower than what was used in the prior analysis. Note that the strain at peak stress (provided in e-mail correspondence from M. F. Hessheimer, 7/21/00) is mostly in the range of 0.0025 to 0.0026, so the shape of the stress-strain curve used in the prior analysis is judged to be reasonable with the exception of softening the modulus.

Table 2-1. Strength and Modulus of Elasticity Results

Sample	Test Number	Load, kN	Stress MPa	Average	Modulus GPa	Average
C1T2	4	1,077	59.0	60.9	26.0	27.1
C1T5	1	1,146	62.8		28.2	
C1T6	3	1,109	60.8		27.2	
C2T1	7	1,142	62.6	57.0	25.5	26.6
C2T3	5	959	52.6		26.0	
C2T4	6	1,019	55.9		28.3	
C3T1	8	961	52.7	50.7	18.4	24.4
C3T3	9	1,101	60.4		29.5	
C3T5	2	711	39.0		25.3	
C4T1	11	1,151	63.1	61.8	28.6	28.6
C4T2	10	1,302	71.4		32.4	
C4T3	12	930	51.0		24.9	
D1T2	13	1,316	72.1	71.3	30.8	30.9
D1T3	14	1,293	70.9		30.9	
D1T4	15	1,291	70.8		31.1	
D2T2	16	977	53.6	50.7	28.0	23.6
D2T3	17	799	43.8		15.9	
D2T4	18	996	54.6		26.9	
D3T1	19	1,322	72.5	57.0	31.6	22.5
D3T2	20	873	47.8		17.3	
D3T2	21	922	50.6		18.6	
F1T5	32	1,045	57.3	52.2	22.0	25.8
F1T6	31	1,010	55.3		28.3	
F1T8	33	803	44.0		27.2	
F2T2	30	978	53.6	54.2	27.2	29.5
F2T4	29	911	49.9		28.2	
F2T8	28	1,078	59.1		33.2	
F3AT3	35	790	43.3	41.2	26.4	22.8
F3AT4	36	628	34.4		16.0	
F3AT5	34	839	46.0		26.0	
F3BT2	25	1,316	72.1	59.4	30.6	28.0
F3BT3	26	920	50.4		26.8	
F3BT7	27	1,017	55.8		26.7	
F4T1	22	1,239	67.9	65.9	29.1	30.0
F4T2	23	1,161	63.6		30.2	
F4T2	24	1,205	66.0		30.5	

If all the cylinder and dome pours were averaged, then

$$f'_{c_{avg}} = 58.5\text{MPa}$$

which is within 4% of the C1 value. For this reason, it was decided to use the C1 value throughout the cylinder and dome of the axisymmetric analysis. Similarly, the average value for the basemat is 54.6 MPa or within 8% of the F3B value; therefore, it was decided to use the F3B value, as shown.

2.2.1.2 3DCM Analysis

The 3DCM model encompasses all of region C3 (whose strength is substantially lower than C1) and about half of region C4. For this model, the compressive properties were modified as follows:

$$f_c' = \left(f_{c_3}' + 0.5 f_{c_4}'\right)/1.5 = 54.4 MPa (7{,}838\ psi)$$

$$E = \left(E_{c3} + 0.5 E_{c4}\right)/1.5 = 25.8 GPa \left(3.74 x 10^6\ psi\right)$$

2.2.2 Prestressing

Table 2-2 shows a prestressing data summary, prepared by SNL, which tabulates the averages for measurements of forces, friction, and seating losses.

Table 2-2. Prestressing Data Summary

Avg. Values	Hoop	Vertical
Design Tension Forces	44.4 Tonnes (97.9 K)	49.6 Tonnes (109.3 K)
Jack Force	43.6 Tonnes (96.1 K)	49.0 Tonnes (108.1 K)
Design Lift-off Force	34.1 Tonnes (75.2 K)	46.3 Tonnes (102.1 K)
Jack Lift-off Force	34.0 Tonnes (75.0 K)	44.2 Tonnes (97.5 K)
Load Cell Force (5/4/00)	33.3 Tonnes (73.52 K)	43.6 Tonnes (96.04 K)
Load Cell Force (7/6/00)	33.1 Tonnes (73.04 K)	43.5 Tonnes (95.85 K)
Friction Coeff.	0.18	0.22
Seating Loss (mm)	3.95 mm	4.95 mm
Seating Lost Force	9.56 Tonnes (21.09 K)	4.79 Tonnes (10.56 K)

2.2.2.1 Axisymmetric Analysis

After extensive review of the data, it was decided to use the average load cell force recorded approximately two months after completion of prestressing, on July 6, in the axisymmetric analysis. This includes stress redistributions due to tendon relaxation, seating, and initial effects of creep. Judging by the very limited change from May to July, the July value appears to be a very stable value and it is apparent that creep effects may have been much smaller than anticipated, or partially offset by change in ambient thermal conditions between May and August.

The measured friction coefficients for the hoop and vertical tendons (0.18 and 0.22) were close to the design value assumed prior to the test (0.21). However, there is a great deal of conflicting information in reaching these final friction coefficient conclusions. For example, the measurements for the instrumented vertical tendons show that angular friction may be greatly overstated, but setting losses and "wobble" friction may be understated. The reverse may be true for the hoop tendons. The hoop tendon friction is discussed in more detail for the 3DCM. Since there is no hard-and-fast conclusion on the friction coefficient, it was decided to stay with angular friction that is based on NUPEC's original measurements, namely $\mu = 0.21$ for the hoop tendons. For the vertical tendons, some changes were adopted.

The hoop prestress values relevant to the axisymmetric analysis were recomputed as follows:

Hoop Tendons

The azimuth at which 3.95 mm loss is absorbed/balanced by tendon friction = 39.5° from buttress centerline (by separate calculation; see 3DCM discussion)

$T_2 = T_1 e^{-\mu\alpha}$ $\quad (\mu = 0.21)$

Stress at load cell = 73.04 K/.525 in^2 = 0.96 MPa (139.1 ksi)

Stress at anchor set balance/absorption point = 1.074 MPa (155.7 ksi)

The stresses at the 135° azimuth were recalculated as:

$$\sigma_{Group1} = 155.7e^{-\left(.21x955x\frac{\pi}{180}\right)} = 109.7\ ksi \quad (757\ MPa)$$

$$\sigma_{Group2} = 155.7e^{-\left(.21x5.5x\frac{\pi}{180}\right)} = 152.6\ ksi \quad (1052\ MPa)$$

These hoop prestress values are 5% lower than those used in the earlier analysis.

Vertical Tendons

The strain gage measurements on V46 and V37 (plots attached as Figure 2-2 and 2-3) show much different stress distributions than originally assumed. The axisymmetric model was not originally set up to model vertical tendon anchor set or wobble friction. However, judging by the measurements of Tendon V46, some simulation of stress variation along the straight vertical tendon segments was needed. From Table 2-2, the average force measured in the vertical tendons on July 6, 2000 was 43.47T (95.85k). For Tendon 46, it was 42.18T (93 kips), and there were significant losses along the cylinder barrel section of the model (see Figure 2-2). Without having much additional data, Tendon V46 was used as a prototype for the final axisymmetric analysis vertical tendon stress distribution. As such, the anchor force was set equal to 42.18T (93 kips). The stress at the anchor is therefore

$$\sigma_{vertical} = 42.18T/3.393cm^2 = 1222\ MPa\ (177\ ksi).$$

A friction tie strategy similar to the dome strategy of the earlier axisymmetric models was adopted and implemented as shown in Figures 2-4, 2-5, and 2-6. The resulting stress distribution after prestressing and equilibration is shown in Figure 2-7. The stress results are also shown on the measurement plots in Figures 2-2 and 2-3. The anchor force used is about 8% less than that for the prior pretest analysis. For friction, an angle for the 5 friction ties of 11.70 degrees was selected to achieve the stress losses shown in the figures. This friction tie modeling strategy was explained in detail in the pretest analysis report [1].

2.2.2.2 3DCM Model

The 3DCM model behavior was found to be sensitive to the extent of anchor set; thus more discussion is warranted for making the final tendon stress assumptions for this model.

The 3DCM model spans vertically from hoop tendon H35 to H72. The prestressing tendon tensioning data [1] shows that the average hoop tendon seating loss is 3.95 mm when averaged over all hoop tendons *and* when averaged over H35 to H72. Therefore, it was decided to use 3.95 mm for the seating loss on all hoop tendons. This put the seating loss zone of influence at 39.5 degrees from the buttress centerline, which creates a case that is partway between Case 1 and Case 2 from the early 3DCM anchor set loss sensitivity study [1]. This assumption appears to agree fairly well with the strain gage data points on the hoop tendons that were instrumented (H35, H53, and H68) (see Figures 2-8 to 2-13). The measured strains/forces at the midpoints of H53 and H68 imply that the angular friction may be a little smaller than the design value (0.18 versus 0.21), but the H35 measurements show that near penetrations where the tendon path curves around the penetrations, the effective angular friction may be higher than the design value. For the tendons represented in the 3DCM, it was assumed that the design value 0.21 (as measured by NUPEC in separate mock-up tests) would provide a reasonable average of the varying conditions that occur in the cylinder-midheight region. Note that the initial stress profile of H35 simulated in the 3DCM mimics the plotted measurements, with the minimum stress position at a point closer to the equipment hatch, rather than at the tendon midpoint (90 degrees). This is because of the extra local angle changes that the tendon passes through when sweeping around the E/H.

Although it would be possible to input different hoop tendon stresses in each tendon, it was decided to use the average load cell value of 32.89T (72.5 kips) that existed at the July 6 measurement. The load cell measurements for H40 (End A) and H58 (End A) appear unreasonably low compared to the jacking forces, and an average force seems more appropriate. The target hoop prestress at the anchors, therefore, was

$$\sigma_{anchor} = {32.89T}/{3.393cm^2} = 952MPa\,(138.1ksi).$$

The final hoop tendon stress profiles produced are shown in Figures 2-8 through 2-16.

2.2.3 Creep, Temperature, and Other Time Dependent Effects

Judging by the minimal change in the tendon forces between May and July, the effects of creep and shrinkage appear to be much smaller than anticipated. It is difficult, however, to isolate the creep response from other time-dependent effects, such as temperature. Since creep effects will tend to be largest within the first 30 to 60 days after prestressing, using the July 6 measured prestress values accounts for time-dependent effects reasonably well. In general, as is shown in Figures 2-8 to 2-13, the initial levels of prestress arrived at are lower than those measured on individual tendons by between 3% and 10%. This should accommodate creep effects that may occur between July 6 and September 26, but no further creep and temperature effect simulations have been performed other than the one discussed in the pretest analysis report [1].

2.3 Data Presentation

The goals of the final pretest prediction analysis were to update the prediction results with analyses that included the latest material properties and tendon stress conditions. As noted, this was done primarily to support test operations by providing the 'best' predictions of the model's response for real-time comparison to the actual response. The following suites of data were provided for making real-time comparisons during the test:

1. All Standard Output Locations (SOL);

2. Four sets of displacement profile data versus pressure (vertical sections at 90 degrees, 135 degrees, and 324 degrees and a horizontal profile at Elev. 4.7m);

3. Four sets of strain data to be displayed on panels (E/H, A/L, M/S and Wall-Base Juncture).

Some of the more important plots with the published and final pretest predictions are presented in Chapter 4. The radial displacements at the bottom and top of the final 3DCM model are compared to the final axisymmetric model results in Figures 2-17 and 2-18. Comparing to the previous pretest analysis shows a trend of slight reduction in 3DCM radial displacement and an increase in axisymmetric radial displacements. This brings the 3DCM radial displacement results, at 135 degrees, a little closer to the axisymmetric results, but there is still a substantial difference between the two. Developing a final suite of analysis data to compare to test data during the test meant choosing between cylinder radial displacement data predicted by the two different models. To this end, it was decided to use a spatial interpolation scheme to develop a consistent set of displacement data for the entire cylinder. The difference between the 3DCM model and axisymmetric model radial displacements is one of several posttest evaluation topics in this report.

2.4 Conclusions of Final Pretest Analysis

Final changes to the pretest prediction analyses were documented prior to the test and summary results. Based on the final analyses, the general failure mode prediction, liner tearing near the equipment hatch, did not change; nor did the failure (leakage) pressure, 3.2 Pd. The final ranking and predicted sequence of failure locations was previously published in the pretest predictions report [1]. Those predictions are repeated below for reference.

Table 2-3. Possible Liner Tearing Locations in Descending Order of Probability of Occurrence

Most Likely Occurrence	Location
1.	E/H near vertical T-anchor termination (4 locations, Type 3);
2.	E/H near horizontal stiffener termination(4 locations, Type 2);
3.	Near a weld seam with hoop stiffener rat-hole, 5 degrees from the centerline of 90 degree buttress (i.e. 95 degrees; occurs in roughly 6 locations);
4 and 5	Similar to 1 and 2, but near the A/L (7 locations, Types 3 and 2);
6.	Similar to 1, but near the M/S penetration (2 locations, Type 3);
7.	Similar to 1 and 2, but near the feedwater (F/W) penetration (3 locations, Types 3 and 2);
8.	Strain concentration Location Type 4 near F/W penetrations, M/S penetrations.
9.	Liner tear at wall-basemat juncture.

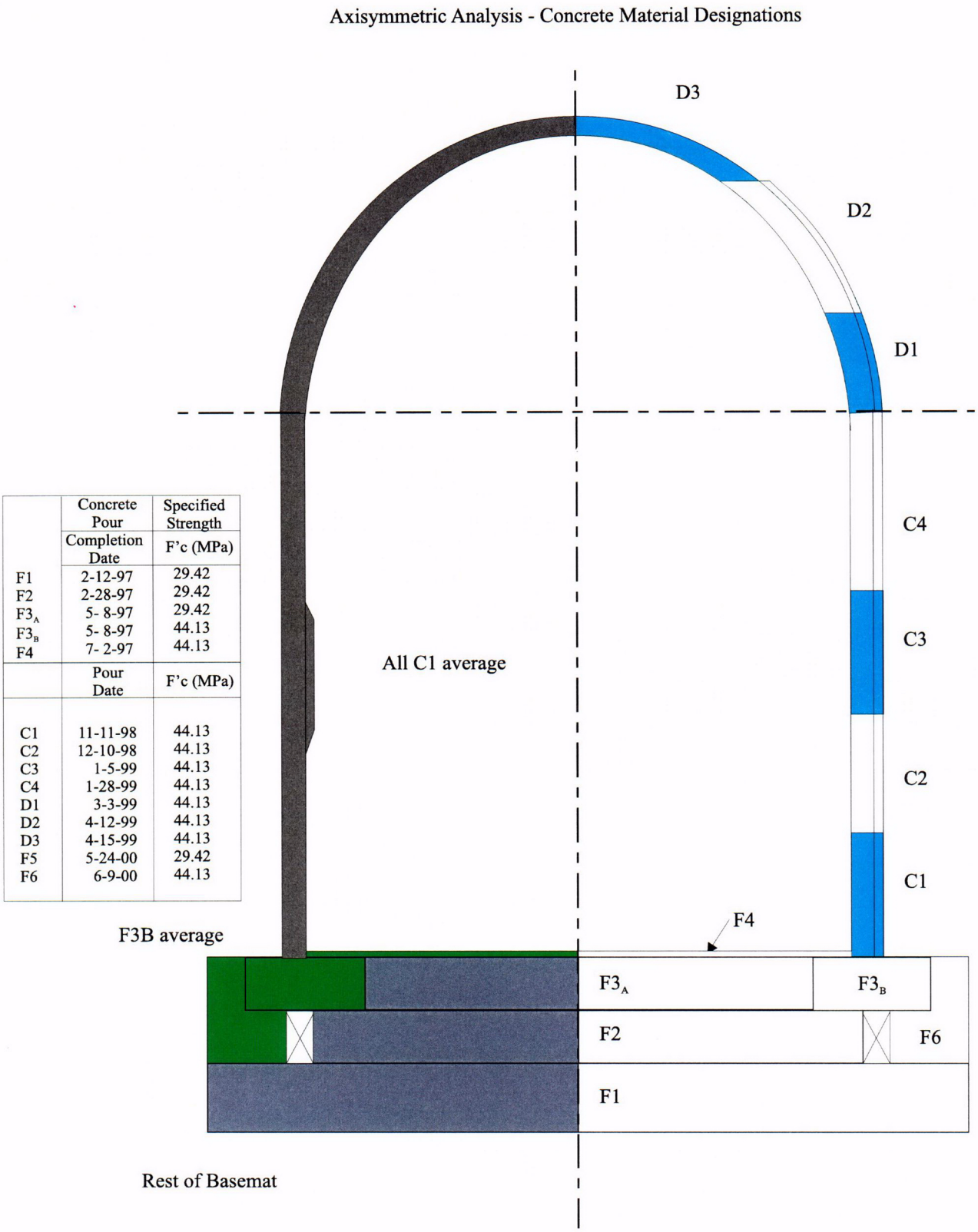

	Concrete Pour Completion Date	Specified Strength F'c (MPa)
F1	2-12-97	29.42
F2	2-28-97	29.42
$F3_A$	5- 8-97	29.42
$F3_B$	5- 8-97	44.13
F4	7- 2-97	44.13
	Pour Date	F'c (MPa)
C1	11-11-98	44.13
C2	12-10-98	44.13
C3	1-5-99	44.13
C4	1-28-99	44.13
D1	3-3-99	44.13
D2	4-12-99	44.13
D3	4-15-99	44.13
F5	5-24-00	29.42
F6	6-9-00	44.13

Figure 2-1. PCCV Model with Revised Concrete Pour Schedule

C01

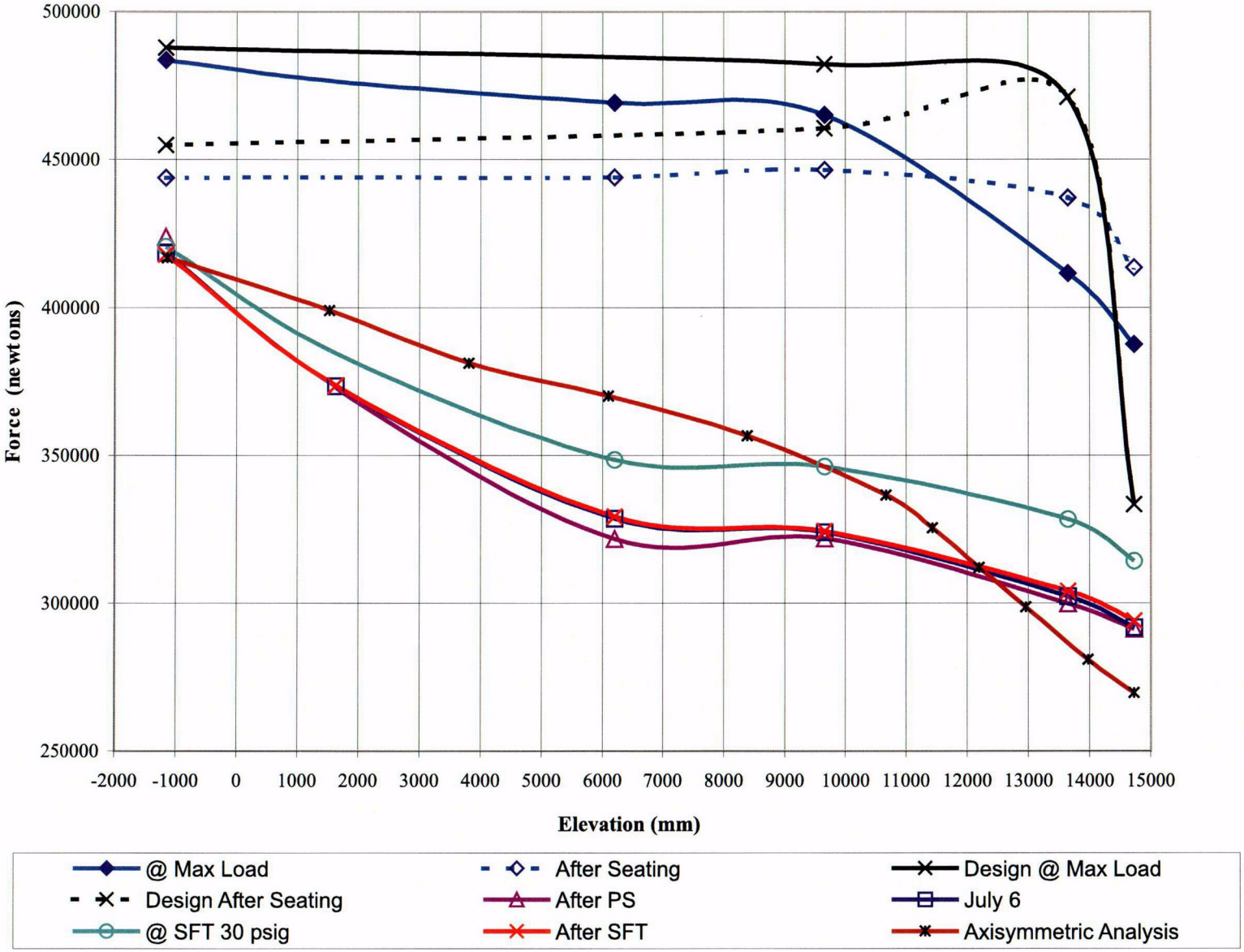

Figure 2-2. Tendon Force Measurements for Vertical Tendon #V46

C02

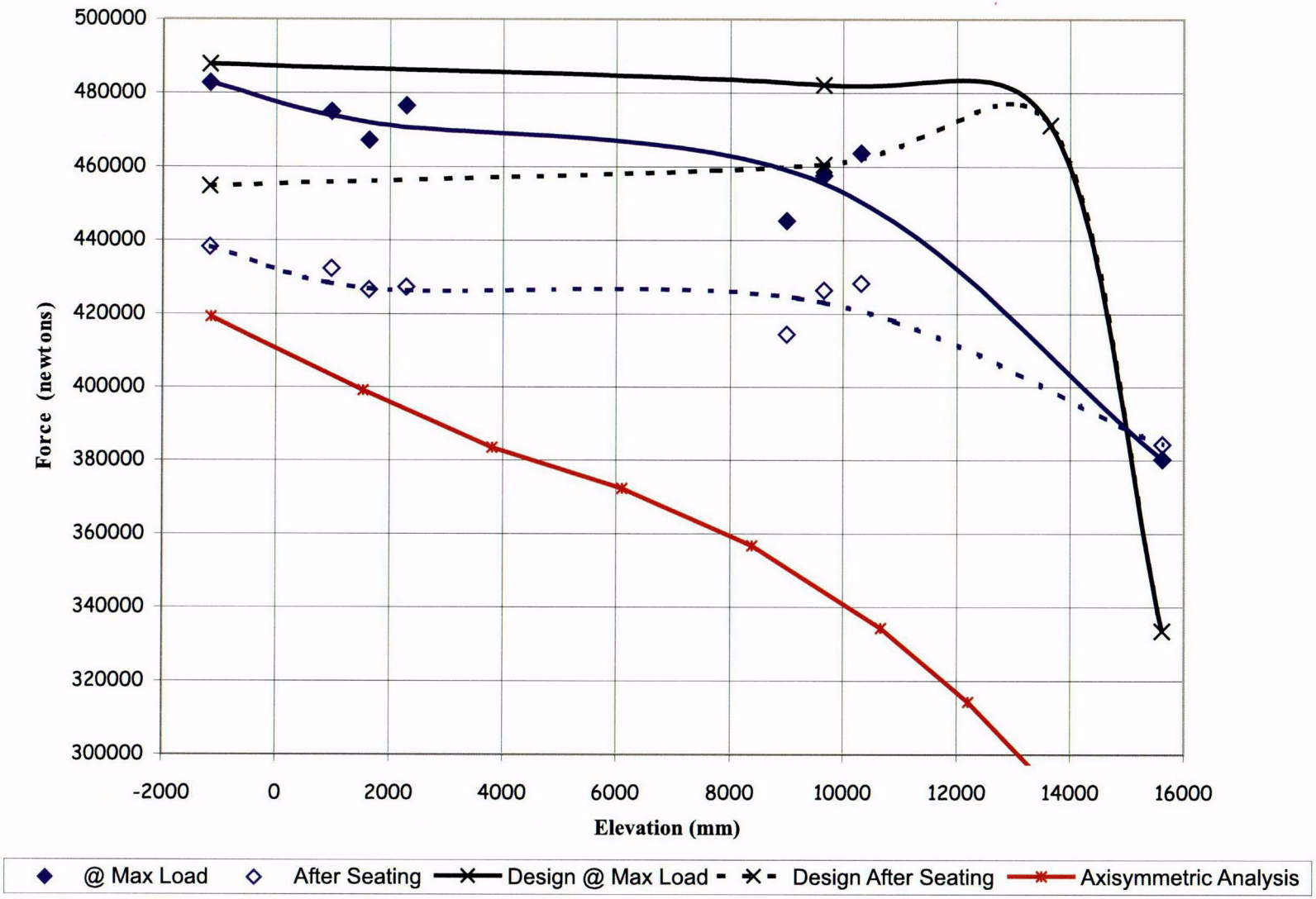

Figure 2-3. Tendon Force Measurements for Vertical Tendon #V37

C03

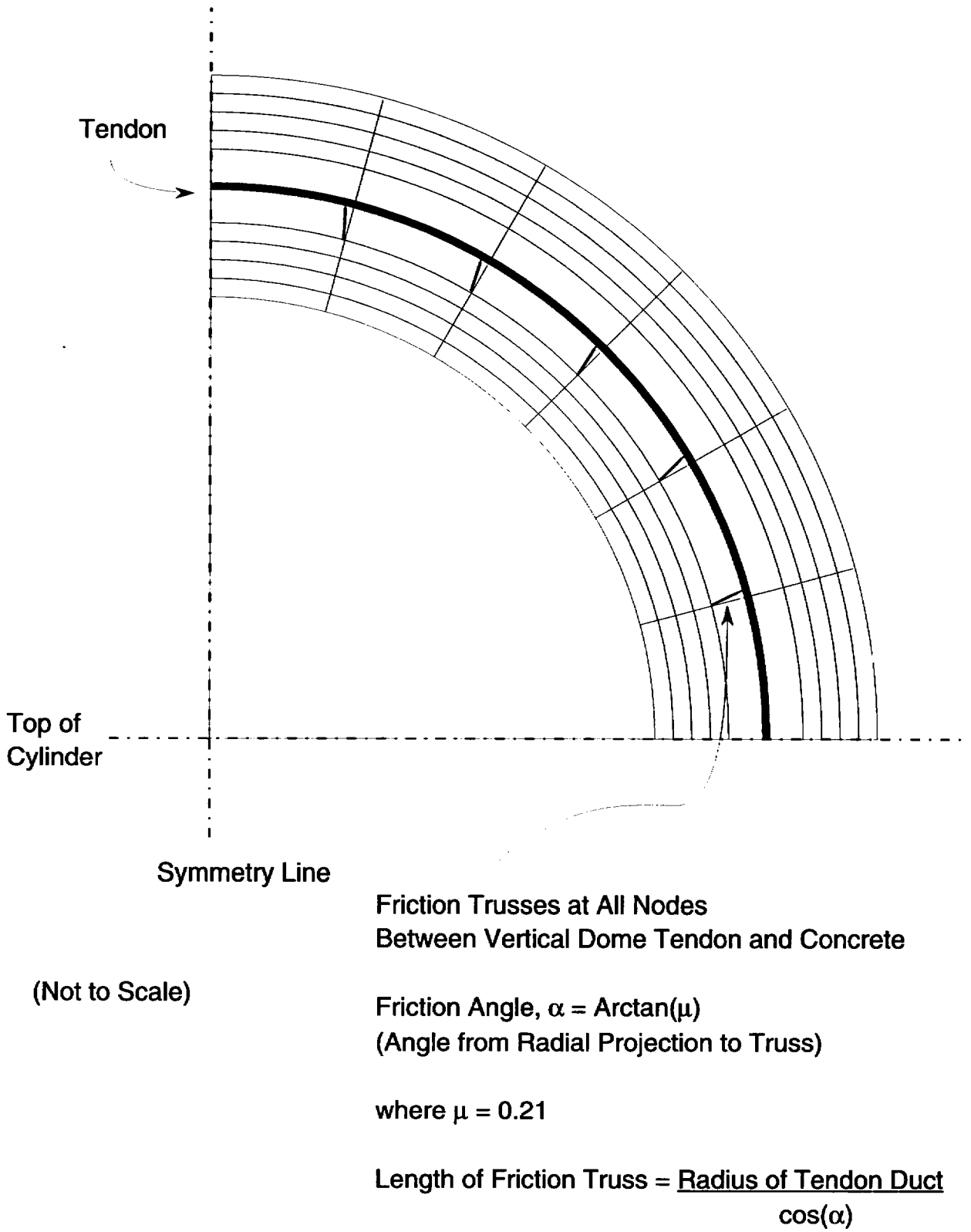

Figure 2-4. Modeling of Tendon Friction Behavior

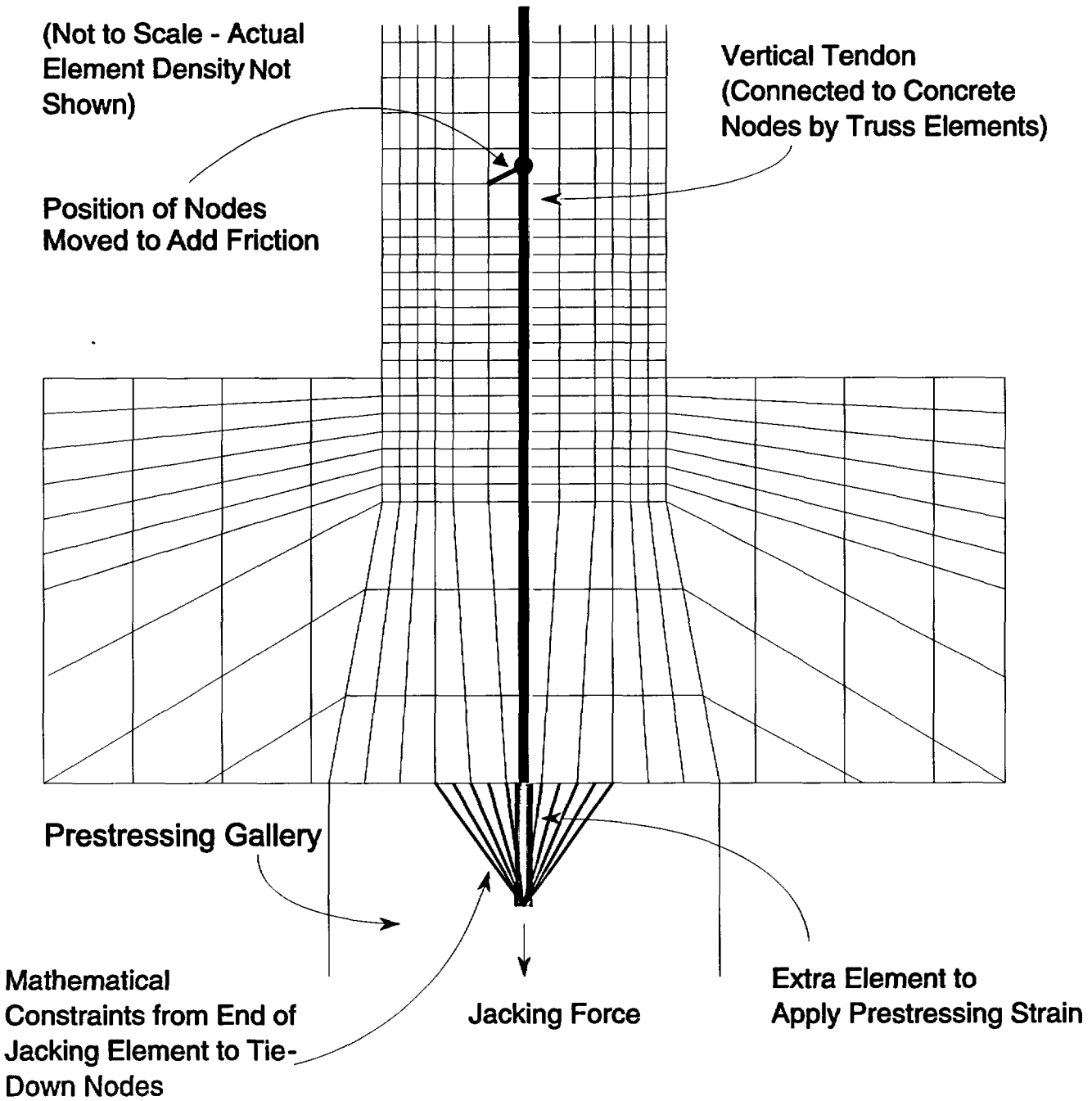

Figure 2-5. Modeling of Prestress Application with Jacking Element

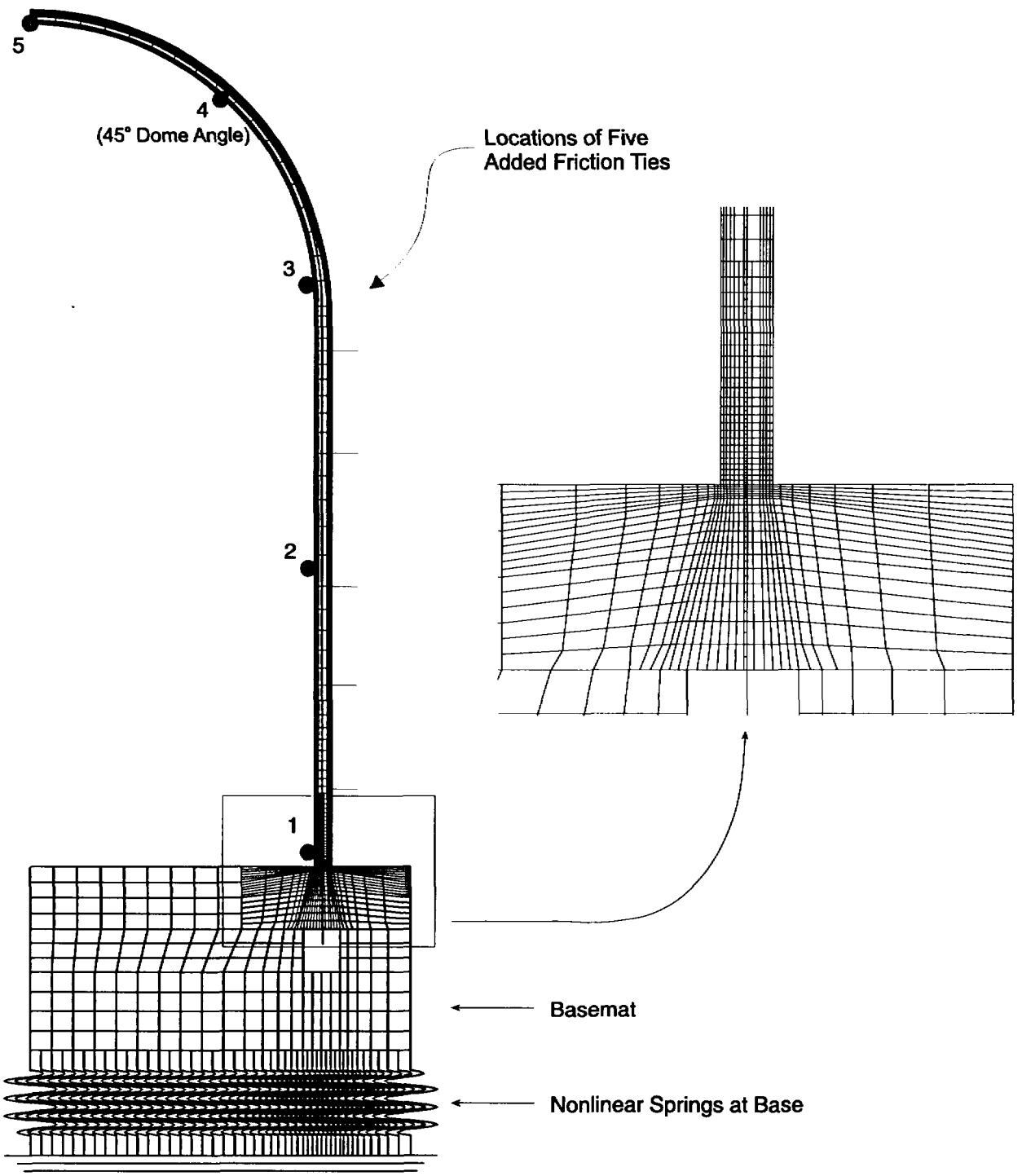

Figure 2-6. Axisymmetric Model of PCCV and Locations for Plotted Output

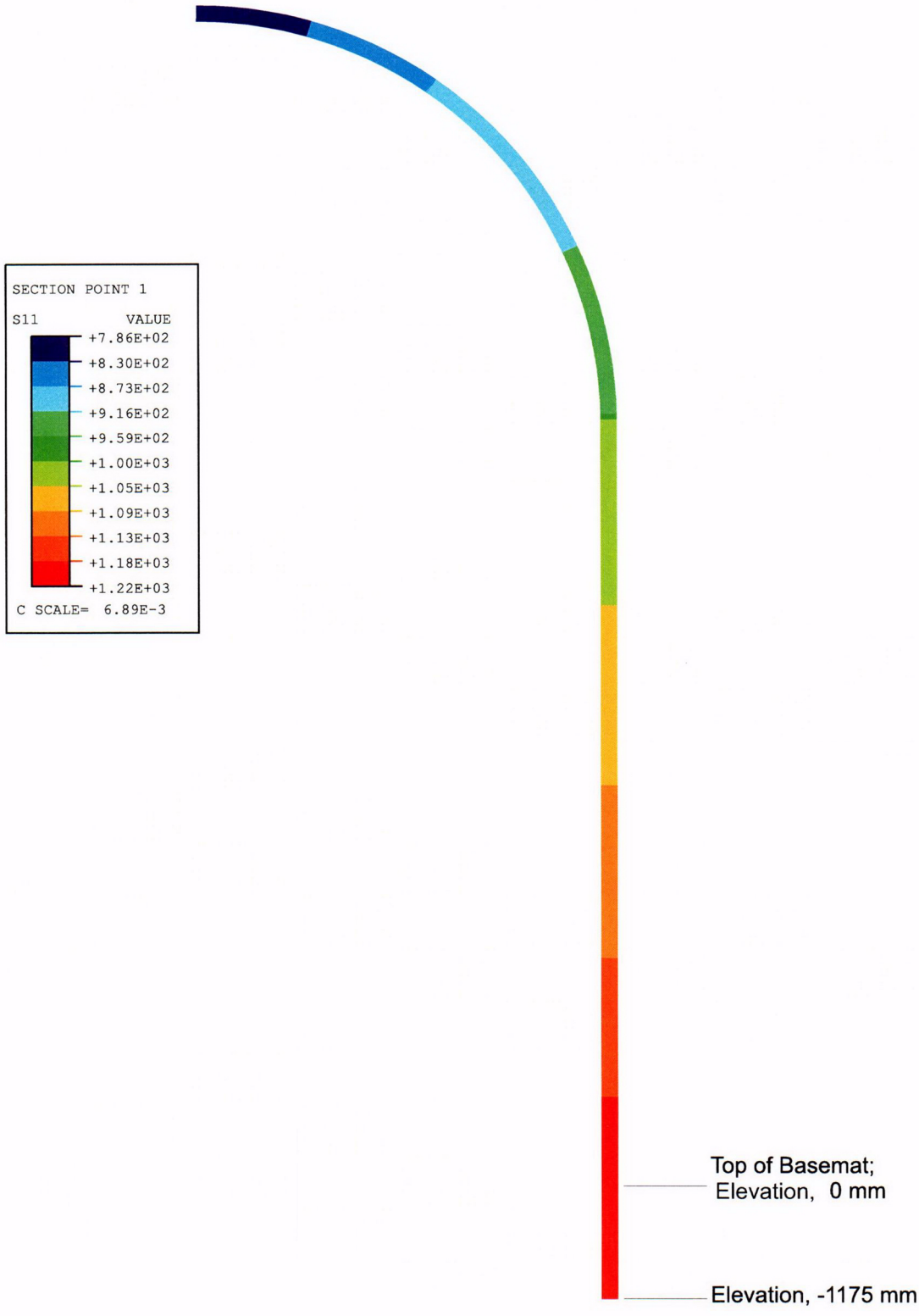

Figure 2-7. Vertical Stress (MPa) in Vertical Tendons after Prestress

C04

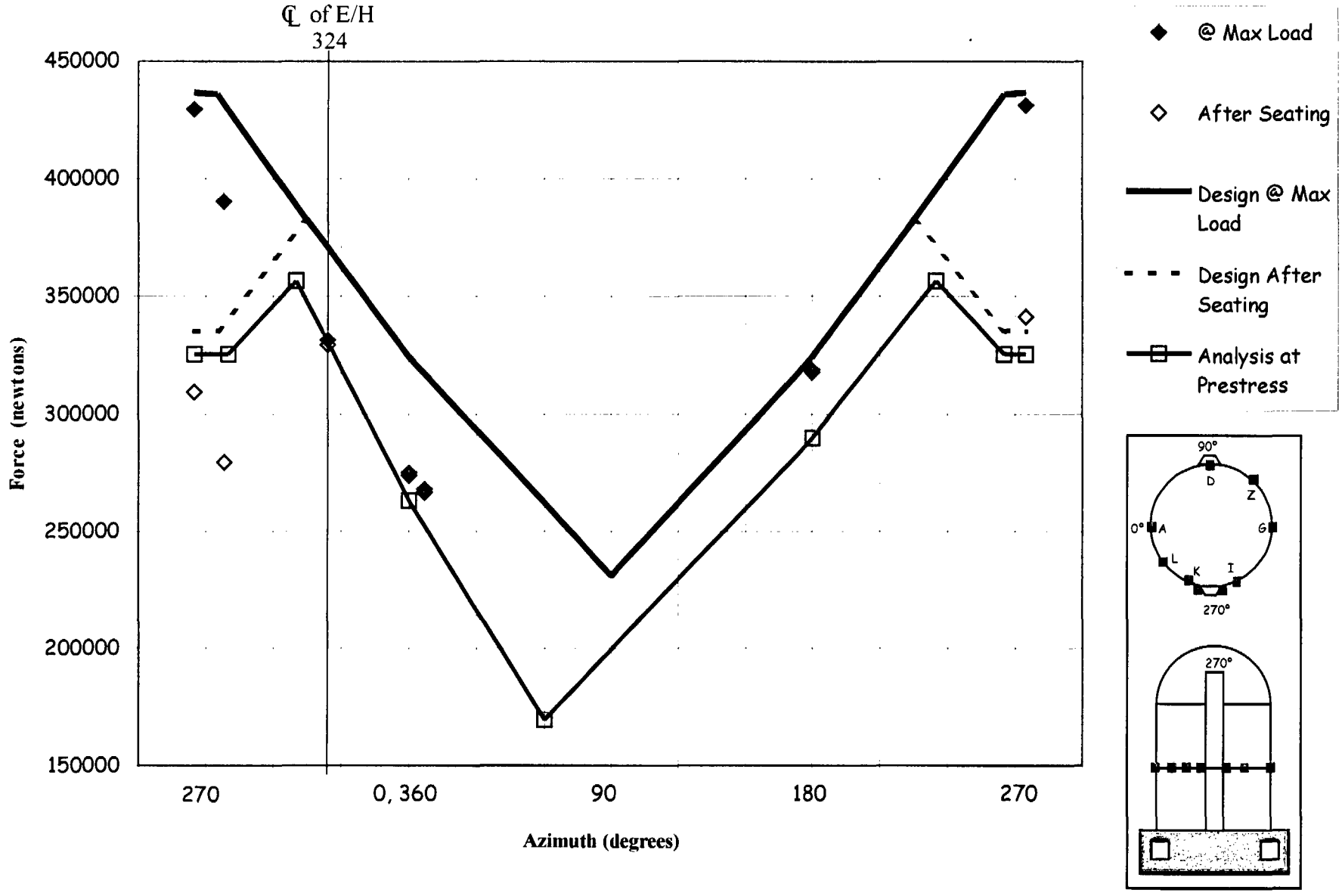

Figure 2-8. Tendon H35 Force Distribution (Strain Gage Data)

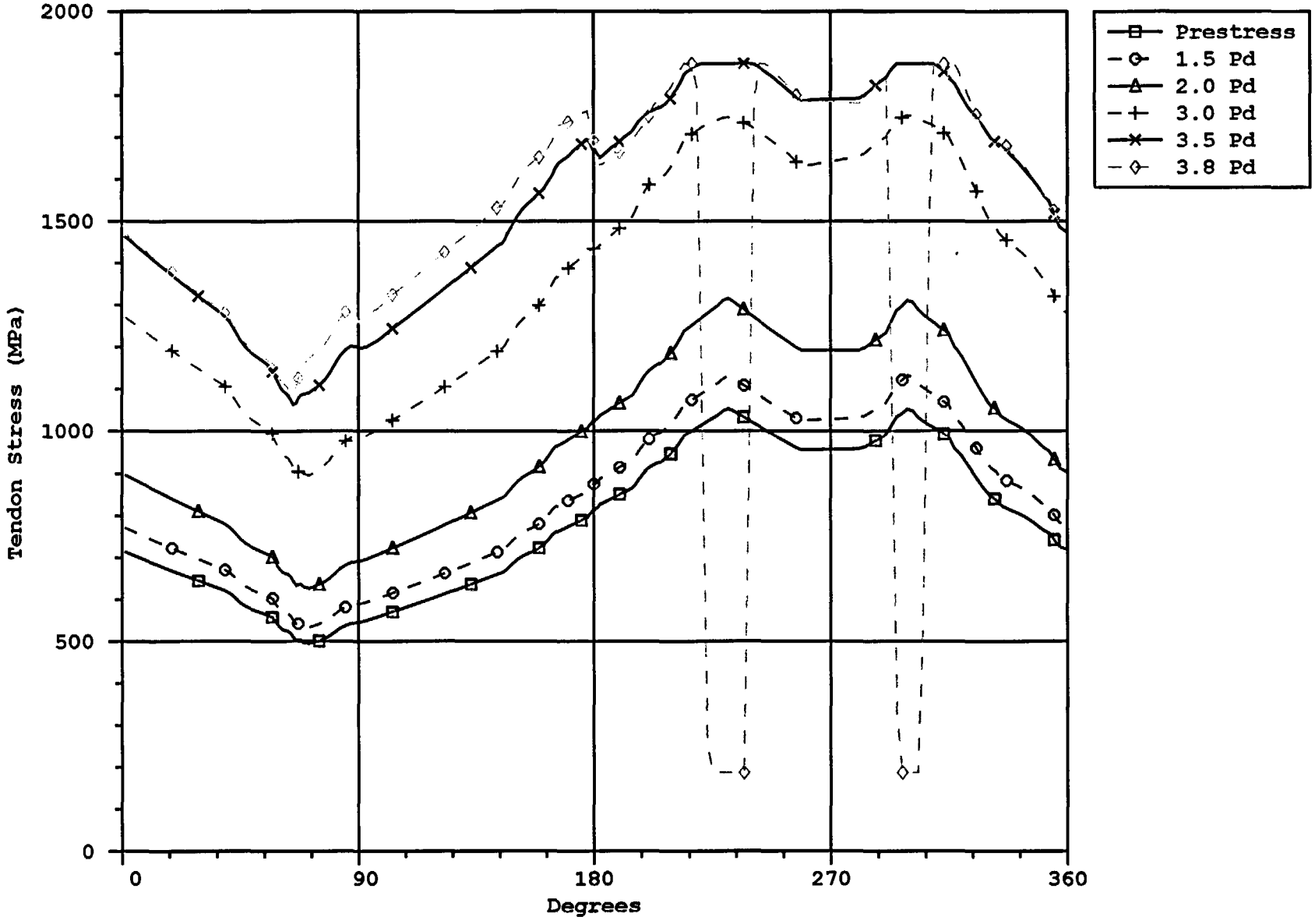

Figure 2-9. Tendon Stress Profile for Instrumented Hoop Tendon #H35

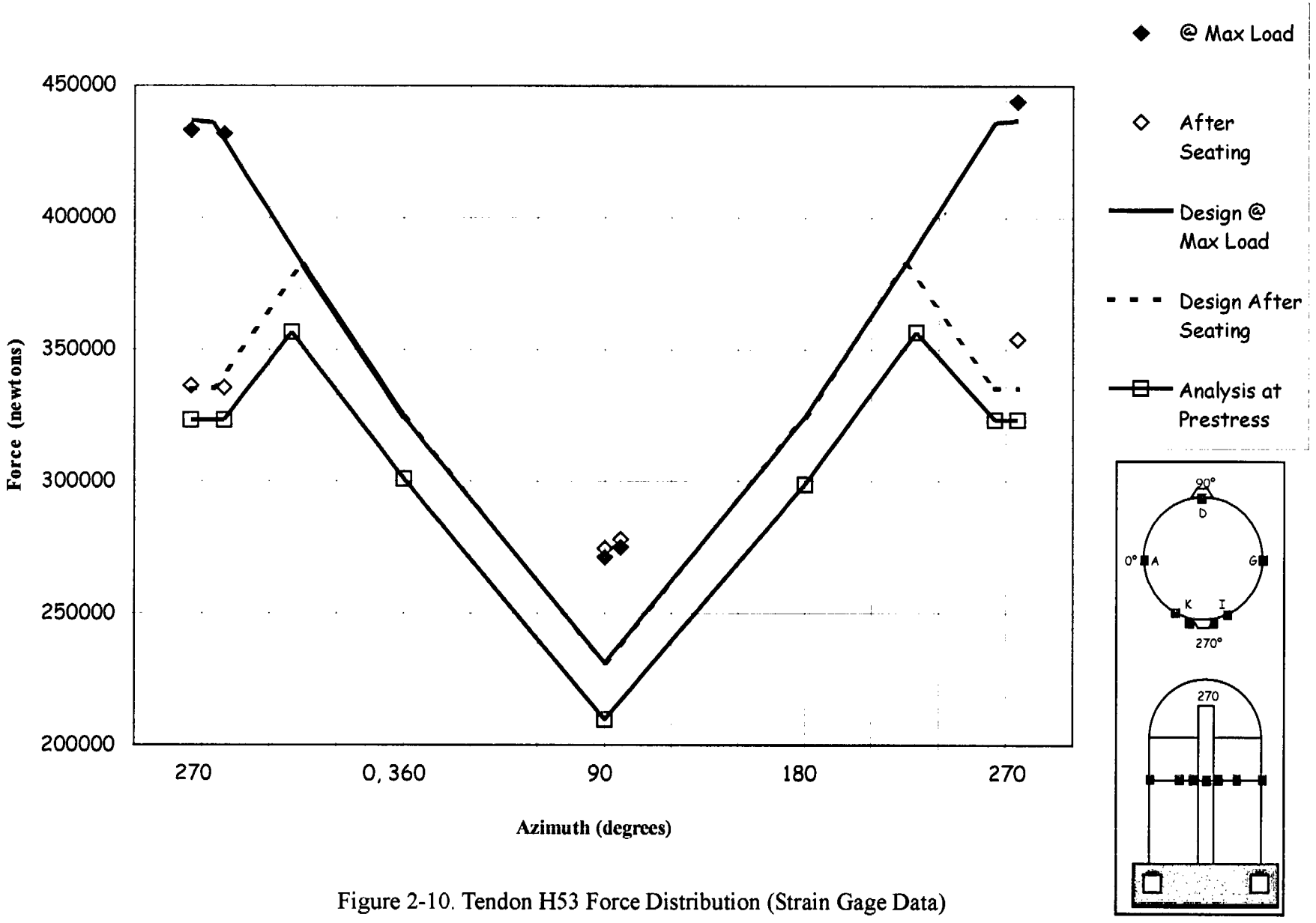

Figure 2-10. Tendon H53 Force Distribution (Strain Gage Data)

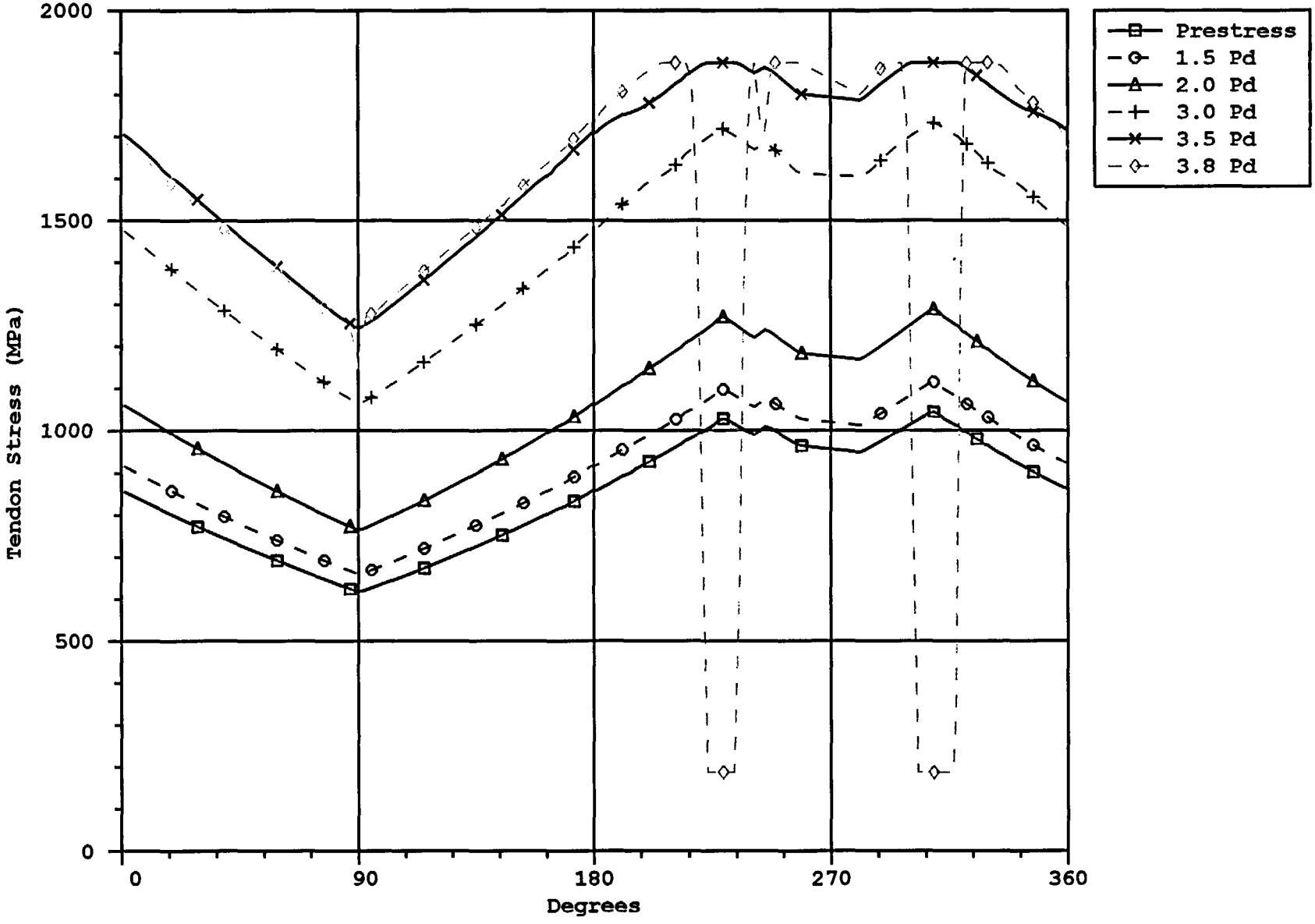

Figure 2-11. Tendon Stress Profile for Instrumented Hoop Tendon #H53

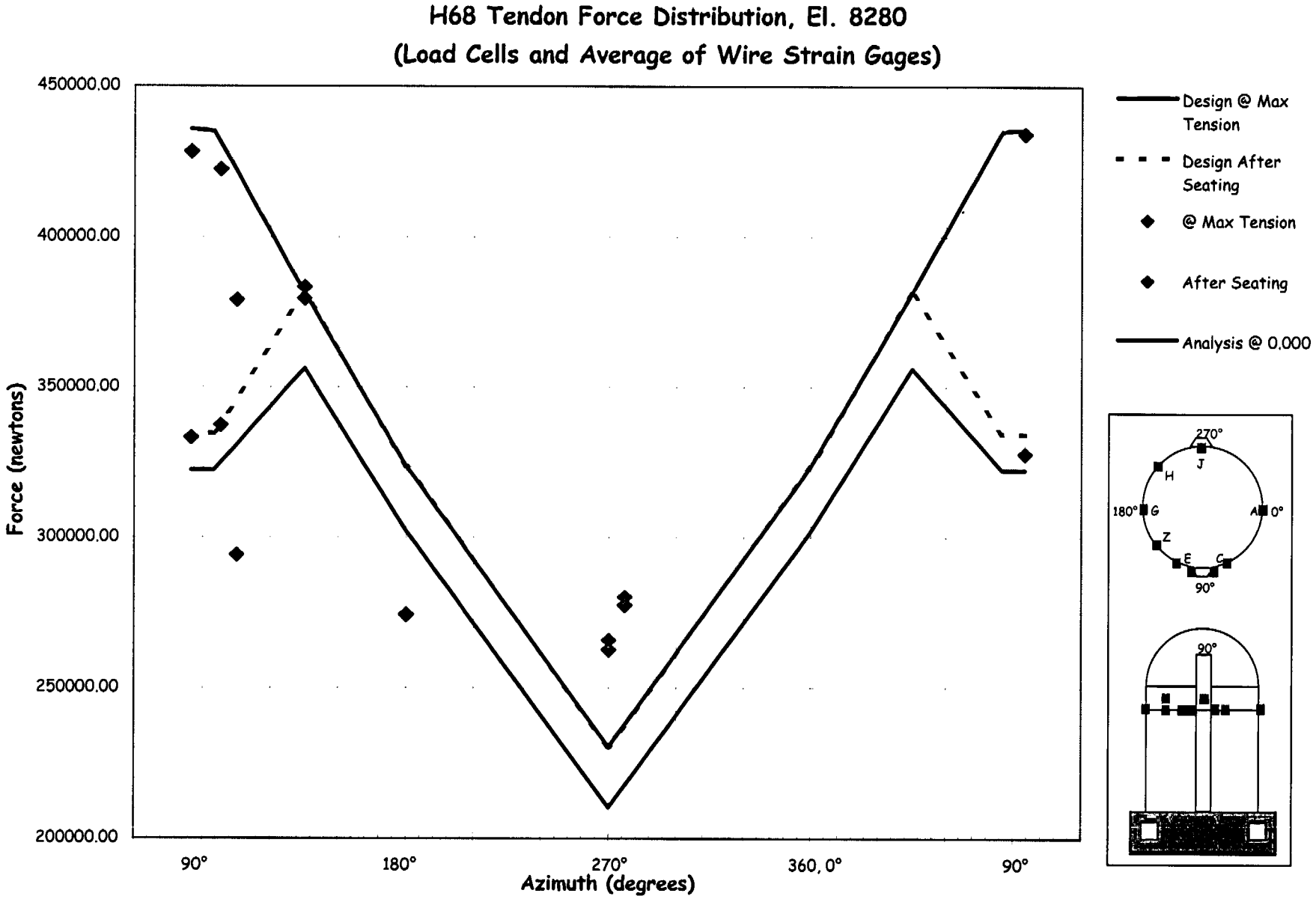

Figure 2-12. Tendon H68 Force Distribution (Strain Gage Data)

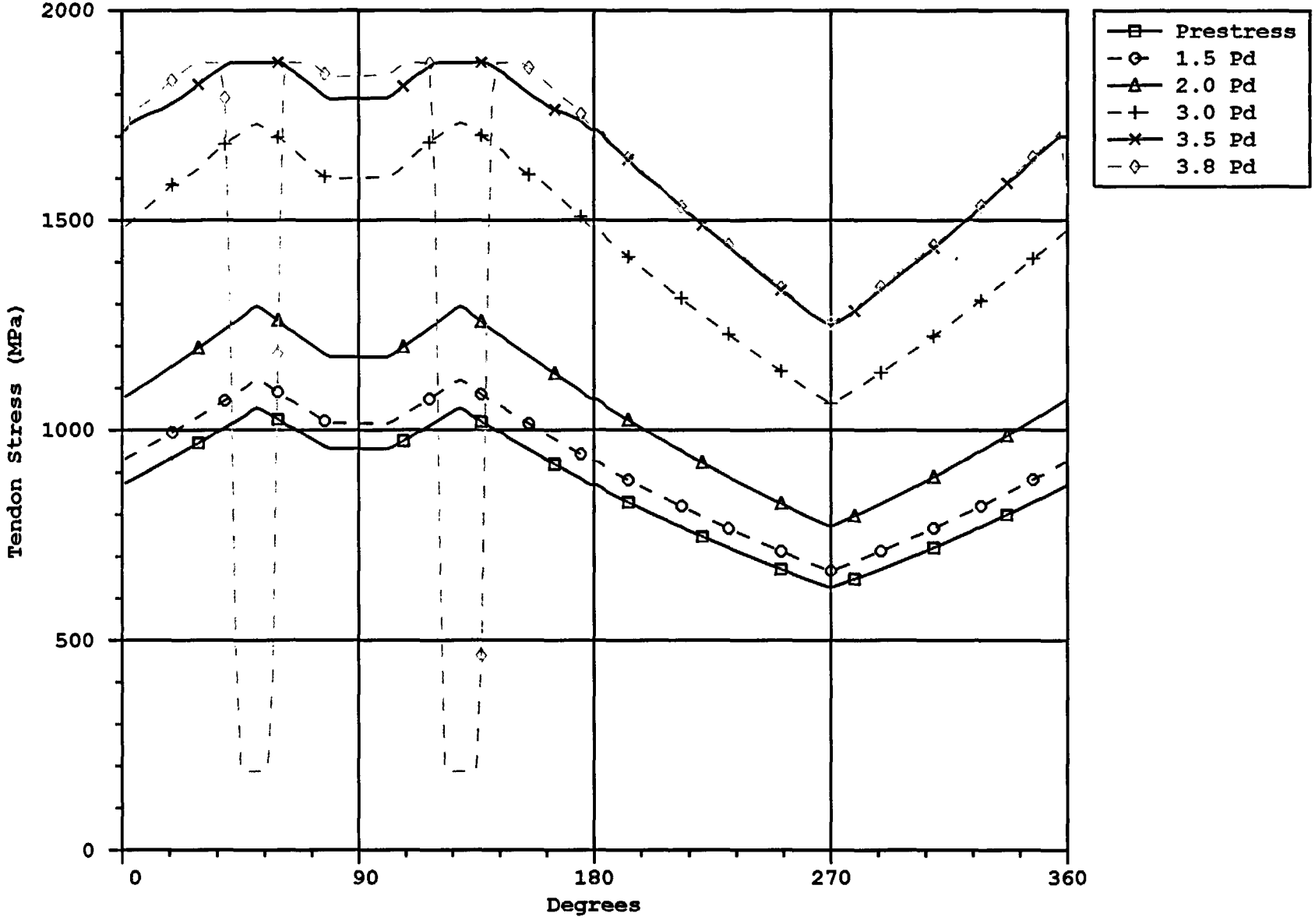

Figure 2-13. Tendon Stress Profile for Instrumented Hoop Tendon #H68

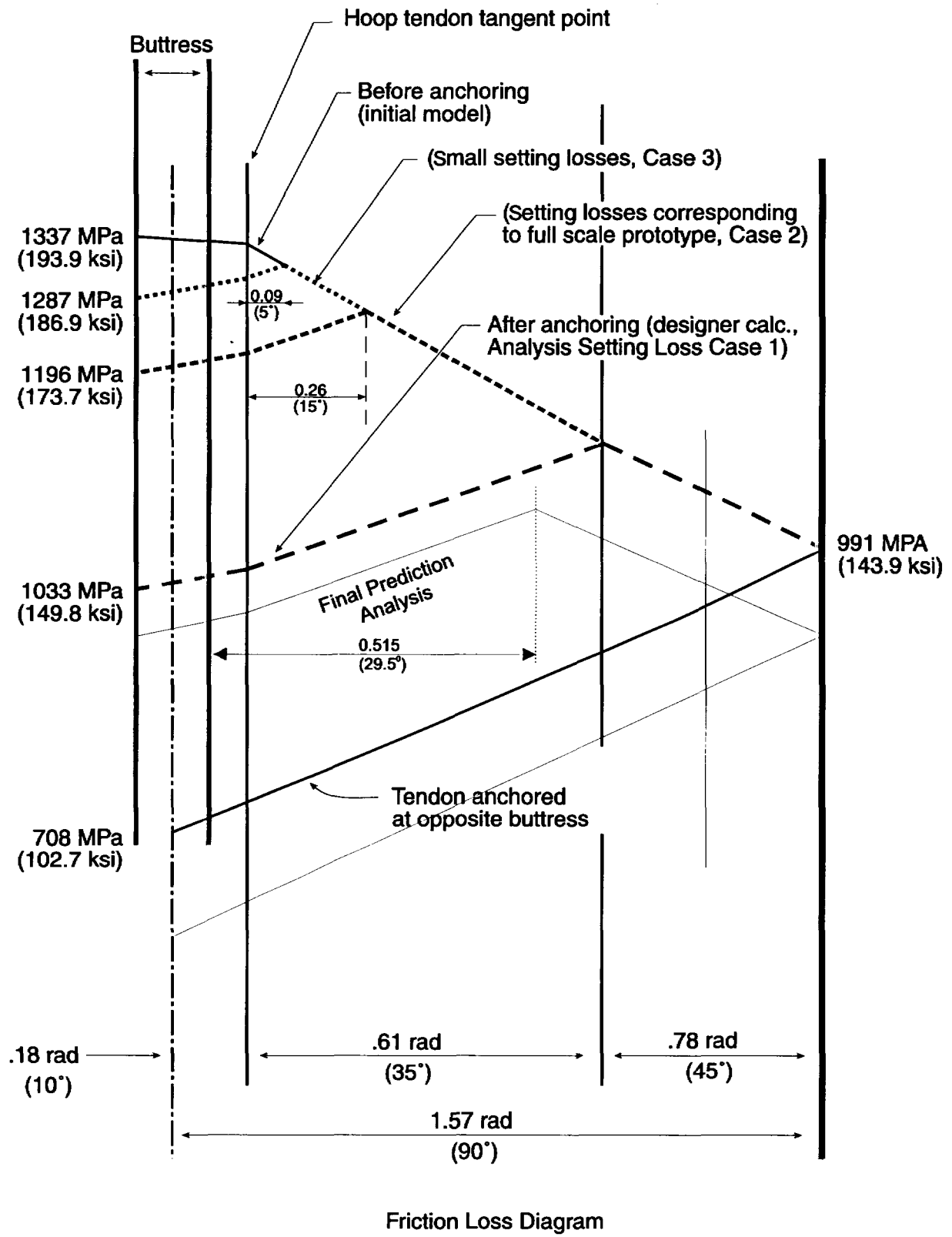

Figure 2-14. Other Setting Loss Cases for Parameter Study

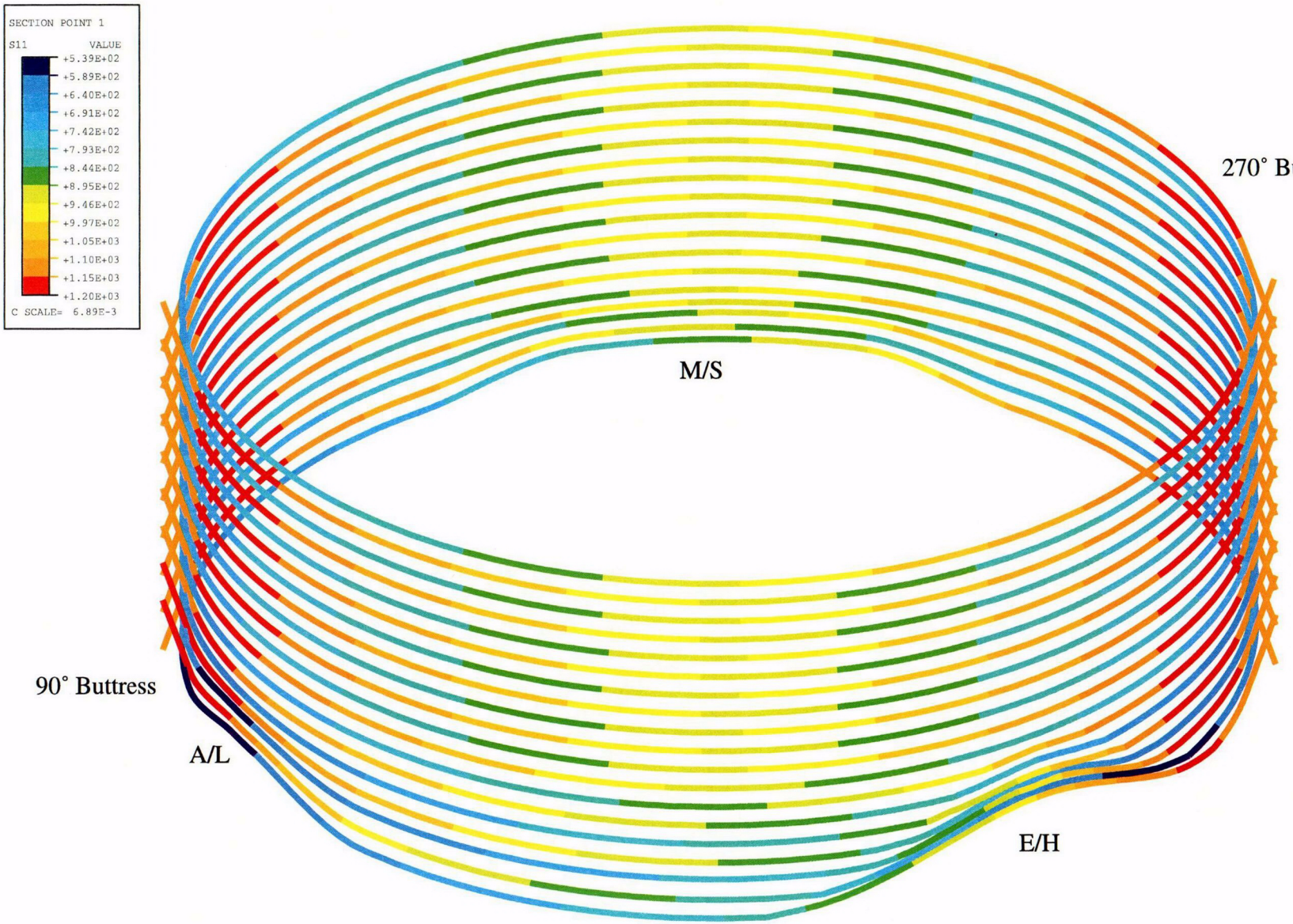

Figure 2-15. Stress Contours (MPa) in Hoop Tendons After Prestress

C05

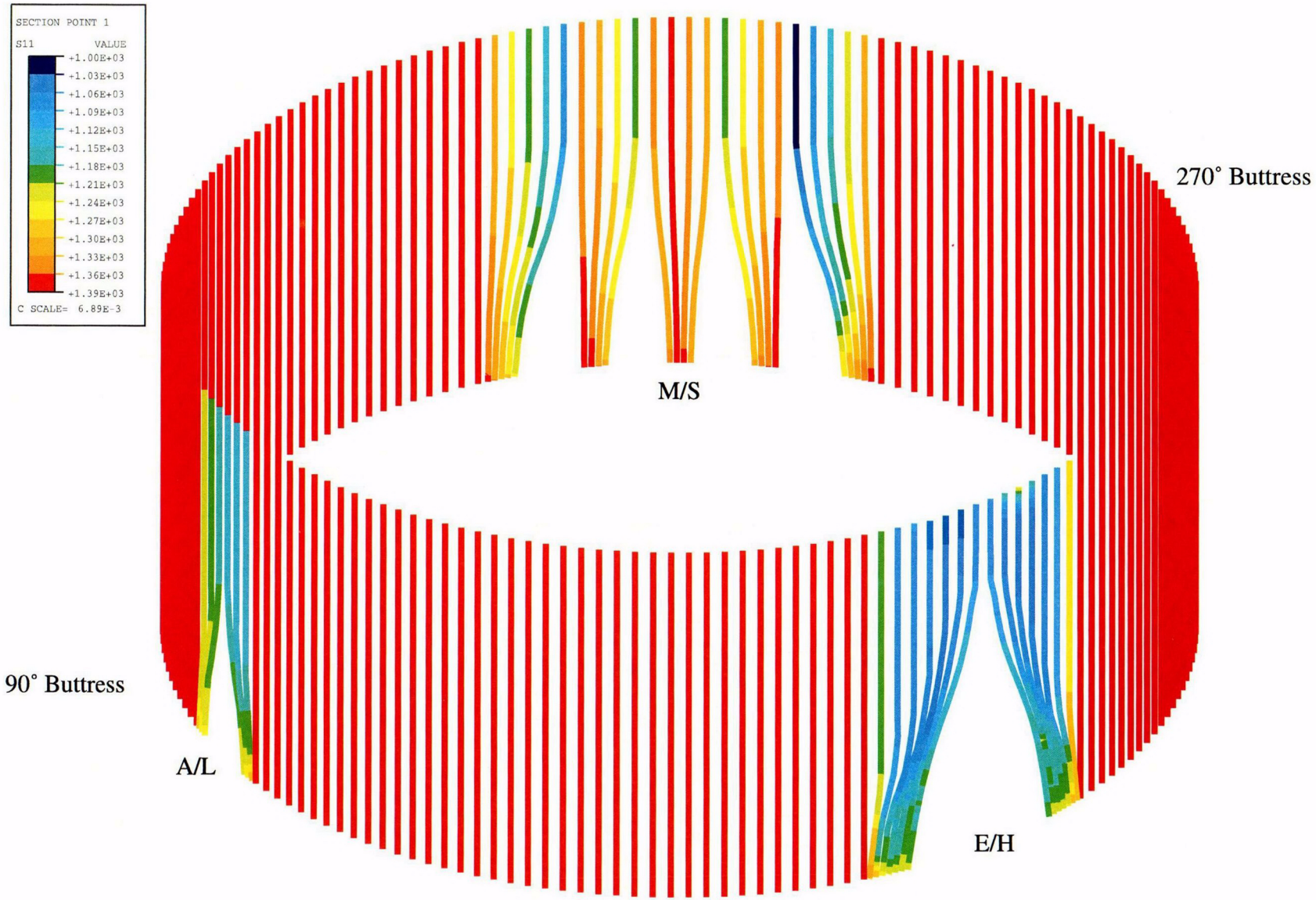

Figure 2-16. Stress Contours (MPa) in Meridional Tendons after Prestress

C06

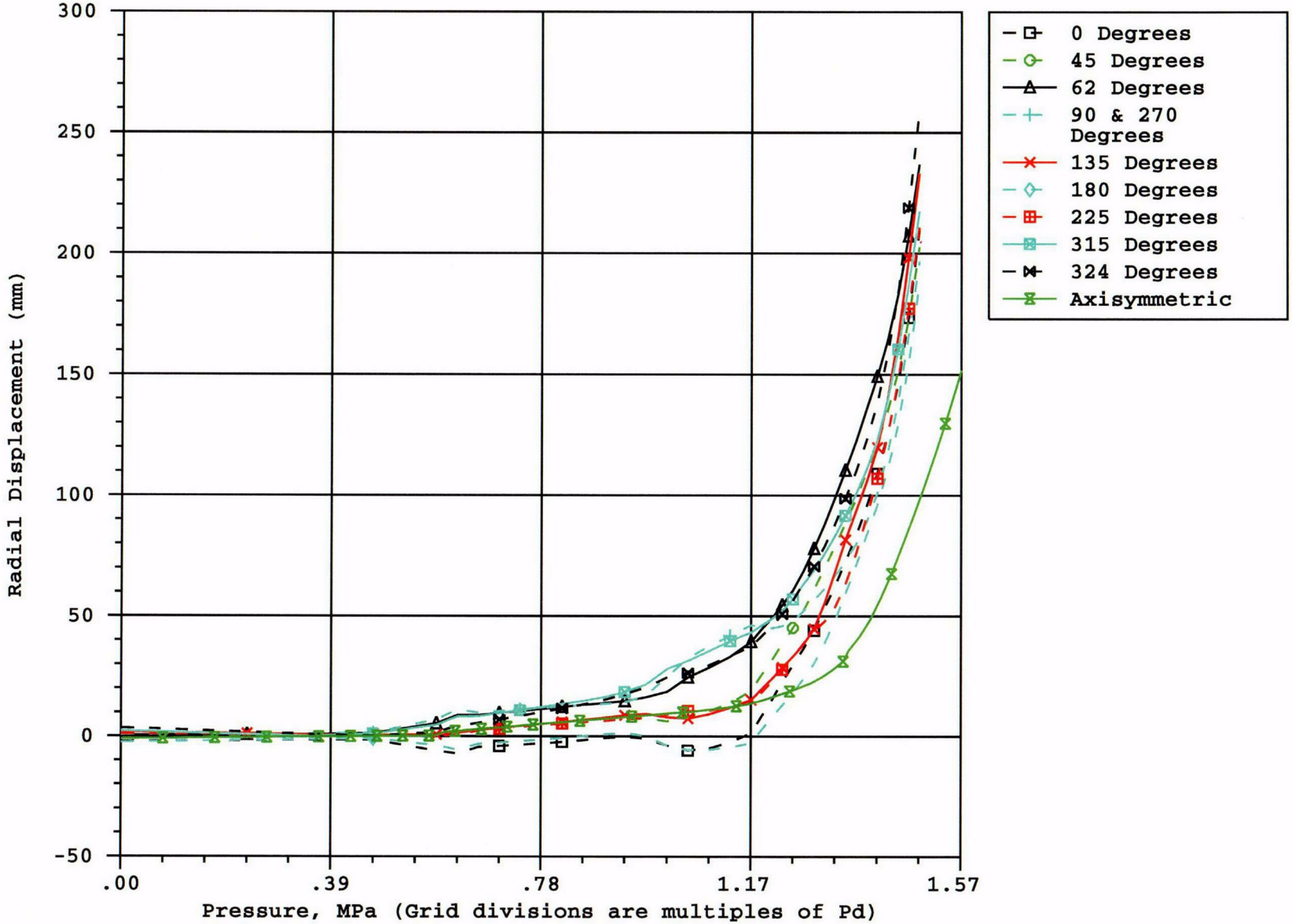

Figure 2-17. Radial Displacement at EL = 4.7 m, 3DCM Compared to Axisymmetric

C07

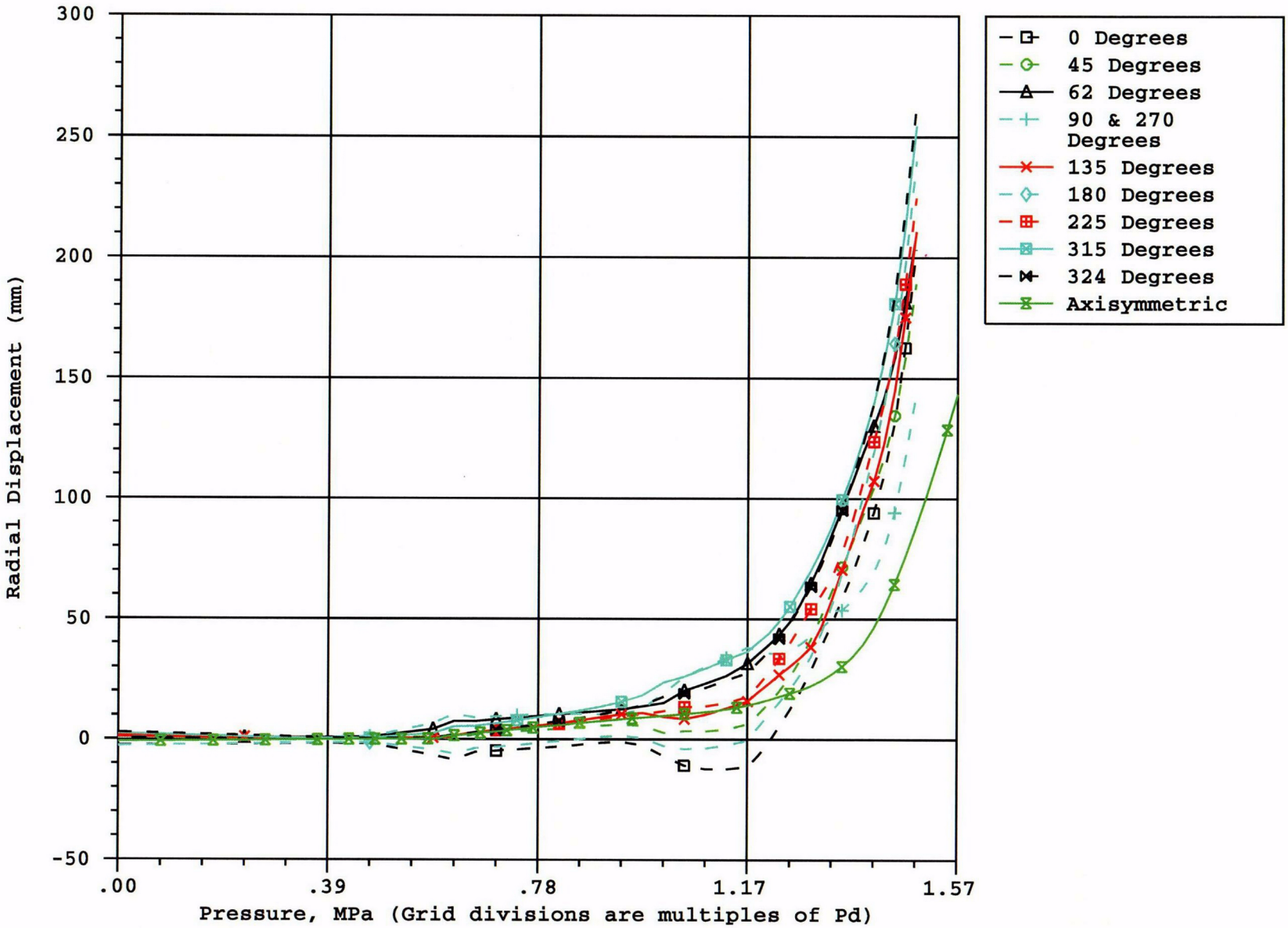

Figure 2-18. Radial Displacement at EL = 8.9 m, 3DCM Compared to Axisymmetric

C08

3.0 TEST MEASUREMENTS

3.1 Overview of Instrumentation

In any experimental program, there are a number of external factors or artifacts of the instrumentation that can influence the data. The goal of this effort was to identify these factors and, to the extent that their influence was significant, adjust the raw data to produce a uniform data set. As part of the posttest analysis effort, ANATECH was also tasked with reviewing the data, identifying significant external influences or artifacts and, if possible, correcting the measurements taken during the LST for these unwanted influences.

A detailed presentation and discussion of the PCCV instrumentation is beyond the scope of this report; a thorough coverage is provided in Ref. 8. This chapter identifies the external influences on the test data and then summarizes the methods to characterize and correct for these influences, if feasible. The details of the corrections are also included in the PCCV test report [8].

The instrumentation measurements in the "data correction" effort, and the effects and phenomena that were addressed, are listed below.

Table 3-1. Instrumentation Measurements

Measurement	Effects Considered for Correction
Displacement	Temperature, Rigid Body Motion
Strains in Special Gaged Rebars	Temperature, Strain Localization
Strains in Liner	Temperature
Pressure	--
Strains in Rebar	Temperature, Strain Localization
Tendon Strains	Temperature
Temperatures	--

3.2 Temperature Effects on Measurements

The data acquisition system was installed and activated more than seven months prior to the LST. Gage measurements taken at various time intervals throughout these seven months provided a vast database of the model's response to changes in ambient temperature. Since the goal of the "data correction" effort is to create a corrected set of data that is free of temperature effects, data were extracted from the database to calibrate correction formulas for each gage. Changes in temperature have a direct influence on the strains and displacements of a free-standing structure. Furthermore, temperature changes have secondary effects on the voltage readouts of strain gages. Both of these effects were considered and quantified in the data correction effort; the former by direct observation of the model response during the calibration periods and the latter by the gage manufacturer. To correct for either phenomena first requires that the temperature be known at every gage, or, in effect, at all possible locations within the PCCV. This information was obtained by developing a temperature mapping algorithm based on interpolation between the matrix of temperature gages. Development of the temperature mapping and data correction algorithms is described in the test report [8].

3.3 Instrumentation Artifacts

In addition to temperature effects, some data artifacts were introduced by the inherent limitations of the instruments themselves or by the methods used to mount them to the structures.

3.3.1 Displacements

While analyses report absolute displacements, that is, in terms of a fixed, global coordinate system, displacement data obtained from experiments are always relative to some other physical structure. In the case of the PCCV model, nearly all the displacements were obtained by measuring the vertical and radial motion of the PCCV relative to the internal instrumentation frame and basemat. The basemat vertical uplift was measured relative to the mudmat. All of these 'reference' structures are, themselves, subject to the same influences and loads as the main body of the PCCV model, and therefore also move. A separate set of instruments were applied to these structures to monitor their motion in response the these loads. This data was used to evaluate whether these reference structure motions had a significant influence on the test data. This data is also provided in the test report [8].

With the exception of basemat uplift, the motion of the instrumentation frame to variations in ambient or internal temperature and pressure were negligible relative to the overall motion of the PCCV model, and no corrections were applied to the data.

Regarding the basemat uplift, after the pressure test were completed, it was recognized that the mudmat tended to conform itself to the basemat, and as a result, no relative motion between the basemat and mudmat occurred or was measured. This data was initially interpreted to show that there was no basemat uplift. It was subsequently recognized, therefore, that the vertical displacement transducers on the basemat were not capable of measuring the absolute uplift of the basemat. Unfortunately, no other transducers were available to provide this data and no correction algorithm could be developed. The implications relative to the analysis are described in the next chapter. Fortunately, however, the calculated uplift is relatively small and has very little influence, if any, on the vertical displacement data for the cylinder wall and dome.

3.3.2 Rebar Strains

In addition to the temperature effects described above, there is an additional gage artifact that affects strain gages mounted on deformed rebar. The strain gages used in the PCCV model tests are foil-type resistance gages bonded to the rebar using adhesives. In order to 'glue' these gages to the rebar, a relatively flat, smooth surface is required. This surface is obtained by grinding away the local deformations over an area slightly larger than the gage and then polishing this surface. This grinding, while minimized, reduces the cross-sectional area of the rebar at the location where the gage is applied. This locally reduced segment then yields slightly before the rest of the bar, and as a result, strains at the gage location are higher (on the order of 0.5%) than the rest of the bar at stresses just below yield and beyond. This is a significant effect and can be demonstrated analytically for reductions in the cross-sectional area as small as 1%. The phenomena has been illustrated by a series of rebar tensile tests performed at SNL, a few results of which are plotted in Figure 3-1.

This artifact was known from previous experience, and efforts were made to minimize the effect during instrumentation of the rebar. Data was collected on the final bar diameters with the hope that a standardized correction algorithm could be developed.

Recognizing that the rebar gage measurements tend to overpredict the corresponding engineering strain, especially in the range of initial yield (i.e. between $\varepsilon = 0.002$ and $\varepsilon = 0.015$), one possible correction algorithm was developed, as follows. Based on measurements of the instrumented rebar, the typical area reduction as a result of the grinding is 2%. It is assumed that for all strain ε, there is a unique stress, σ, according to the engineering stress-versus engineering strain data. Using the averaged data for the SD390-D13 bars, the yield curve is approximately

ε	σ
.002	58 ksi
.009	60.9 ksi
.013	62.06 ksi
.015	63.075 ksi
.020	66.7 ksi

For a measured local rebar strain, ε_i, the corresponding stress, σ_i, is "looked-up" from the stress-strain data for the bar in question.

The nominal stress in the bar, i.e. outside the locally reduced area, is $\sigma_n = \sigma_i$ / (Area Ratio).

The nominal strain, ε_n, is then returned from the yield function.

This correction is also illustrated in Figure 3-2. Unfortunately, this correction did not account for the complete gage effect. Attempts to apply the correction to all the rebar data did not improve the data, and in some cases made it worse. As a result, it was decided not to apply the correction to the data, but to recognize its presence and consider it, as appropriate, when comparing the data to analyses.

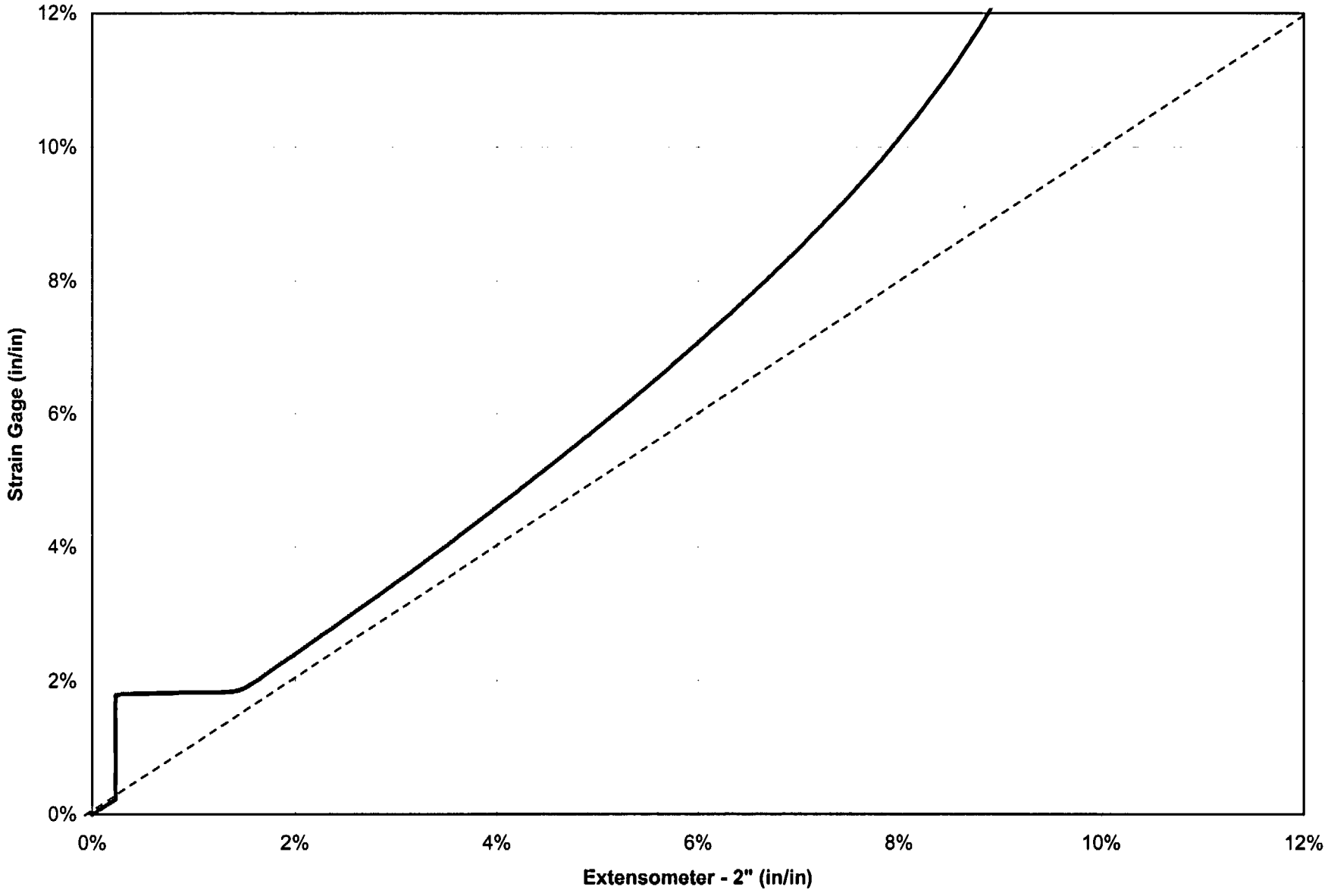

Figure 3-1. Comparison of Strain at Z6 (Azimuth 135 degrees, Elev. 6280)

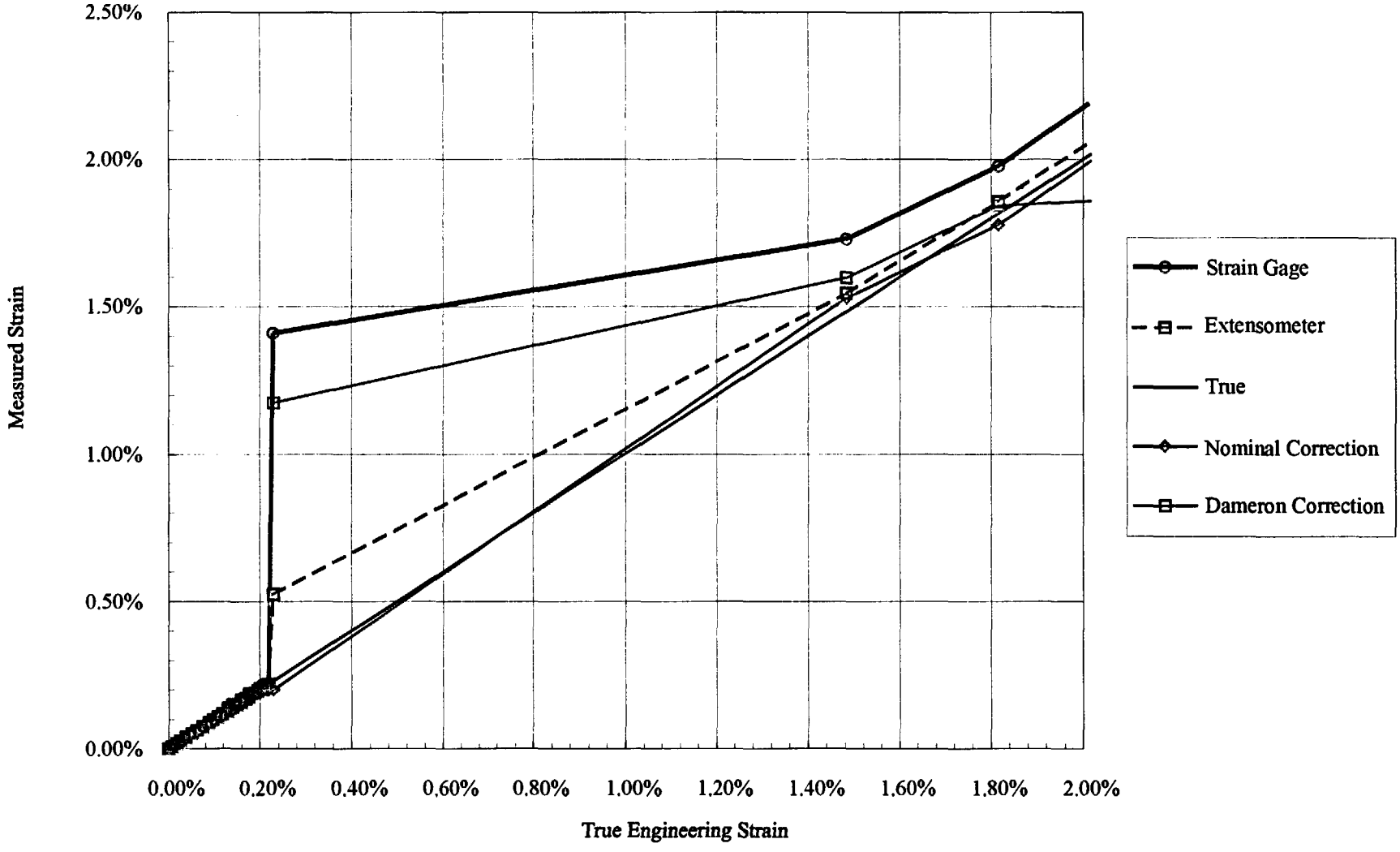

Figure 3-2. Rebar Tensile Test Simulation

4.0 COMPARISONS OF PRETEST ANALYSIS RESULTS WITH THE TEST

The pretest analyses consisted of global axisymmetric analysis and local model analysis. The local models analyzed were: the E/H region, the personnel airlock region, and the M/S penetration region. A detailed 3DCM was also developed to investigate tendon behavior in the cylinder and 3D effects that drive the local strain concentrations near the penetrations. A highly detailed representation of the wall-basemat juncture region was included in the 2D axisymmetric model, making a total of five pretest analysis models. The results of the initial pretest analyses were published in 1999 [1] and were the basis of the SNL/ANATECH contribution to an international Round Robin Pretest Analysis exercise [3]. As described in Chapter 2, a final pretest analysis was completed in 2000, immediately prior to the LST.

This chapter compares the test measurements to both pretest analyses. Test data are compared to the results of the analysis. For example, the results of the 3DCM model, with its explicit tendon representation, are compared to the tendon strain or force data, whereas results of the axisymmetric model are compared to those response data that are relatively independent of the azimuth, such as free-field displacements and the behavior of the wall-base junction and the dome response. The same rationale is used to compare and discuss failure modes.

A set of 55 SOLs, each associated with an actual gage (or set of gages), was identified by the project team to provide a comprehensive suite of data sets for comparison to the round robin analysis results. The SOLs are described in Table 4-1, along with the associated gage(s). After reviewing the PCCV LST data, these locations were indeed useful comparison points. This chapter thus makes extensive use of comparisons at these 55 SOLs. In some cases, to learn more about how the analysis or the test responded at another location, additional plots and comparisons were extracted from the analytical models and the test data.

Table 4-1. Standard Output Locations

Loc. #	Type	Orientation	Az. (deg)	El. (m)	Comments	General Location	Instr. ID (1st)	ID (2nd gage)
1	Displacement	Vertical	135	0	Outside Cylinder	Top of Basemat	DL-M-Z0-01	
2	Displacement	Radial	135	0.25	Inside Liner Surface	Base of Cylinder	DL-R-Z2-01	
3	Displacement	Radial	135	1.43	Inside Liner Surface	Base of Cylinder	DL-R-Z3-01	
4	Displacement	Radial	135	2.63	Inside Liner Surface	Base of Cylinder	DT-R-Z4-01	
5	Displacement	Radial	135	4.68	Inside Liner Surface	E/H elev.	DT-R-Z5-01	
6	Displacement	Radial	135	6.2	Inside Liner Surface	Approximate Midheight	DT-R-Z6-01	
7	Displacement	Radial	135	10.75	Inside Liner Surface	Springline	DT-R-Z9-01	
8	Displacement	Vertical	135	10.75	Inside Liner Surface	Springline	DT-M-Z9-01	
9	Displacement	Horiz. (Rad)	135	14.55	Inside Liner Surface	Dome 45 deg	CP-R-Z11-01	
10	Displacement	Vertical	135	14.55	Inside Liner Surface	Dome 45 deg.	DT-M-Z11-01	
11	Displacement	Vertical	135	16.13	Inside Liner Surface	Dome apex	DT-M-Z13-01	
12	Displacement	Radial	90	6.2	Inside Liner Surface	Midheight @ Buttress	CP-R-D6-01	
13	Displacement	Radial	90	10.75	Inside Liner Surface	Springline @ Buttress	CP-R-D9-01	

Table 4-1. Standard Output Locations

Loc. #	Type	Orientation	Az. (deg)	El. (m)	Comments	General Location	Instr. ID (1st)	ID (2nd gage)
14	Displacement	Radial	324	4.675	Inside Liner Surface	Center of E//H	CP-R-L5-01	
15	Displacement	Radial	62	4.525	Inside Liner Surface	Center of A/L	CP-R-C5-01	
16	Rebar Strain	Meridional	135	0.05	Inner Rebar Layer	Base of Cylinder	RS-M-Z1-01	
17	Rebar Strain	Meridional	135	0.05	Outer Rebar Layer	Base of Cylinder	RS-M-Z1-02	
18	Rebar Strain	Meridional	135	0.25	Inner Rebar Layer	Base of Cylinder	RS-M-Z2-01	
19	Rebar Strain	Meridional	135	0.25	Outer Rebar Layer	Base of Cylinder	RS-M-Z2-02	
20	Rebar Strain	Meridional	135	1.43	Inner Rebar Layer	Base of Cylinder	RS-M-Z3-01	
21	Rebar Strain	Meridional	135	1.43	Outer Rebar Layer	Base of Cylinder	RS-M-Z3-02	
22	Rebar Strain	Hoop	135	6.2	Outer Rebar Layer	Midheight	RS-C-Z6-02	
23	Rebar Strain	Meridional	135	6.2	Outer Rebar Layer	Midheight	RS-M-Z6-02	
24	Rebar Strain	Hoop	135	10.75	Outer Rebar Layer	Springline	RS-C-Z9-02	
25	Rebar Strain	Meridional	135	10.75	Inner Rebar Layer	Springline	RS-M-Z9-01	RS-M-Z9-03
26	Rebar Strain	Meridional	135	10.75	Outer Rebar Layer	Springline	RS-M-Z9-02	RS-M-Z9-04
27	Rebar Strain	Hoop	135	14.55	Outer Rebar Layer	Dome 45 deg.	RS-C-Z11-02	
28	Rebar Strain	Meridional	135	14.55	Inner Rebar Layer	Dome 45 deg.	RS-M-Z11-01	RS-M-Z11-03
29	Rebar Strain	Meridional	135	14.55	Outer Rebar Layer	Dome 45 deg.	RS-M-Z11-02	RS-M-Z11-04
30	Rebar Strain	Meridional	90	0.05	Inner Rebar Layer	Base of Cylinder @ Buttress	RS-M-D1-01	
31	Rebar Strain	Meridional	90	0.05	Outer Rebar Layer	Base of Cylinder @ Buttress	RS-M-D1-02	
32	Rebar Strain	Hoop	90	6.2	Outer Rebar Layer	Midheight @ Buttress	RS-C-D6-02	
33	Rebar Strain	Meridional	90	6.2	Outer Rebar Layer	Midheight @ Buttress	RS-M-D6-02	
34	Liner Strain	Meridional	0	0.01	Inside Liner Surface	Base of Cylinder	LSI-M-A1-01	
35	Liner Strain	Meridional	0	0.01	Outside Liner Surface	Base of Cylinder	LSO-M-A1-03	
36	Liner Strain	Meridional	135	0.25	Inside Liner Surface	Base of Cylinder	LSI-M-Z2-01	

Table 4-1. Standard Output Locations

Loc. #	Type	Orientation	Az. (deg)	El. (m)	Comments	General Location	Instr. ID (1st)	ID (2nd gage)
37	Liner Strain	Hoop	135	0.25	Inside Liner Surface	Base of Cylinder	LSI-C-Z2-01	
38	Liner Strain	Meridional	135	6.2	Inside Liner Surface	Midheight	LSI-M-Z6-01	
39	Liner Strain	Hoop	135	6.2	Inside Liner Surface	Midheight	LSI-C-Z6-01	
40	Liner Strain	Meridional	135	10.75	Inside Liner Surface	Springline	LSI-M-Z9-01	
41	Liner Strain	Hoop	135	10.75	Inside Liner Surface	Springline	LCI-C-Z9-01	
42	Liner Strain	Meridional	135	16.13	Inside Liner Surface	Dome apex	LSI-M-Z13-01	LSI-C-Z13-01
43	Liner Strain	Meridional	90	6.2	Inside Liner Surface	Midheight @ Buttress	LSI-M-D6-01	
44	Liner Strain	Hoop	90	6.2	Inside Liner Surface	Midheight @ Buttress	LSI-C-D6-01	
45	Liner Strain	Hoop	334	4.675	Inside Liner Surface	10 mm from thickened plate	LSI-C-A5-03	
46	Liner Strain	Hoop	58	4.525	Inside Liner Surface	10 mm from thickened plate	LSI-C-C5-03	
47	Base Liner	Radial	135	0	100 mm Inside Cylinder	FF Basemat Liner Strain	LSI-R-Z1-08	
48	Tendon Strain	Hairpin	180	15.6	Tendon - V37	Tendon Apex	TT-M-G12-01	TF-M-G12-01
49	Tendon Strain	Hairpin	135	10.75	Tendon - V46	Tendon Springline	TT-M-Z9-01	TF-M-Z9-01
50	Tendon Strain	Hoop	90	6.58	Tendon - H53	Mid. Tendon	TT-C-D6-01	TT-C-D6-02
51	Tendon Strain	Hoop	180	6.58	Tendon - H53	¼ - Tendon	TT-C-G6-01	TF-C-G6-01
52	Tendon Strain	Hoop	280	6.58	Tendon - H53	Tendon Near Buttress	TT-C-K6-01	TF-C-K6-01
53	Tendon Strain	Hoop	0	4.57	Tendon - H35	Tendon between E/H and A/L	TT-C-A5-01	TT-C-A5-02
54	Tendon Force	Hairpin	241	-1.16	Tendon - V37	Tendon Gallery	TL—10-03	
55	Tendon Force	Hoop	275	6.58	Tendon - H53	@ Buttress	TL-C-J6-02	

4.1 Displacements

The most fundamental response quantities to compare are displacements, so significant emphasis was placed on measurements and comparisons of these. As discussed later, various local phenomena can significantly influence the measurements of strains in the liner, reinforcement, or tendons, but displacement measurements are regarded as the most reliable source of general response information. Much global strain information can also be inferred from displacement measurement by using, for example, a kinematic relationship such as

$$\varepsilon_h = \frac{u_r}{R},$$

where ε_h is the hoop strain, u_r is the radial displacement, and R is the radius.

Meridional strain can also be inferred from the difference in vertical displacement divided by the gage length in between.

Displacements as a function of pressure are compared at SOLs 1 through 14 in Figures 4-1 through 4-4. Each comparison plot includes four curves:

1. LST DOR
2. LST correction (LST DOR corrected for ambient temperature effects, as per Reference [8])
3. 2000 analysis (final pretest analysis performed just prior to the test and discussed in Chapter 2)
4. 1999 analysis (published pretest analysis [1] and [4])

A discussion of each comparison is listed by location, below. One additional adjustment to the analysis results should be noted. To focus on comparing the pressure response of the model, all of the analysis results were shifted so that the calculated zero pressure response matched the data at the start of the test. This eliminated differences that could occur due to creep or other time dependent effects. The only other loading conditions considered in the analyses, besides internal pressurization, were dead load and prestressing loads. Since the PCCV instrumentation was initialized on March 3, 2000, after construction was essentially complete, response to dead load was not measured. The model was then completely prestressed, exposed to six months of ambient temperature fluctuations (during which the model was allowed to creep, shrink, and relax), and finally to preliminary pressure testing prior to the start of the LST. By adjusting the analysis results, differences due to these secondary effects were eliminated from the comparison to the pressure response.

SOL 1. Vertical Displacement at Outside Edge, Top of Basemat. The test data shows virtually no uplift, while the analyses at 3.3 Pd show 2.3mm and 9mm for the 1999 and 2000 analyses, respectively. The apparent discrepancy between the test data and the analysis results may be an artifact from the way basemat uplift was measured during the LST. The displacement gage(s) were mounted to measure the relative displacement between the bottom of the basemat and the top of the underlying mud-mat, since there were no other practical means of referencing a fixed point. In an analysis that uses a very stiff foundation, even very small basemat curvatures create appreciable basemat uplift, but being much more flexible, mud-mat flexure can be assumed to follow basemat flexure. As a result, there could have been appreciable basemat flexure without the mud-mat ever separating from the PCCV basemat and, therefore, no observed relative motion. Unfortunately, there is no way to corroborate the accuracy of the analysis predictions for basemat uplift. The differences between the analyses and the test, and between the analyses themselves, are both noteworthy and are discussed in the revised global posttest analysis in Chapter 5.

SOLs 2, 3, 4, 5, 6, 14, and 15. There is very good agreement (to within +/- 4% over most of the pressurization history) for all of the cylinder radial displacement locations between analysis and test, but a few general observations can be made. The analyses and the test consistently exhibit a sharp jump in displacement at approximately 1.45 Pd (0.57 MPa). This is possibly associated with the onset of hoop cracking in the cylinder, although the data is not entirely conclusive on this point. At first, it was thought this was associated with the 3 hour pressure hold at 1.5 Pd, but the jump in the data occurs just prior to the 1.5 Pd pressure hold. Also, there is no similar jump in data at the 2.0 Pd pressure hold, which was held overnight. The radial displacement at the A/L is somewhat overpredicted beyond 2.8 Pd.

SOLs 7, 8, 9, 10, and 11. There is poor correlation between analysis and test data for these displacements in the dome and springline. Radial displacements at the springline were underpredicted in analysis by roughly a factor of 2. Vertical

displacement was also off, but overprediction is understandable, given the significant overprediction of basemat uplift. (The 1999 analysis better predicts this quantity than the 2000 analysis.) The same is true for vertical displacements at the dome 45-degree-angle and the apex, but the radial displacement at the dome 45-degree-angle is well predicted (to within +/- 20%).

SOLs 12 and 13. At the buttress locations, the analysis overpredicted the measured response at the midheight and underpredicted the measured response at the springline. This is consistent with the trends observed in the 3DCM analysis, which is discussed in much more detail in Chapter 6. Note that for SOLs where axisymmetric analysis is inapplicable, only a "2000" results curve is plotted.

4.2 Rebar Comparisons

Rebar comparisons are made in Figures 4-5 through 4-9.

SOLs 16, 17, 18, 19, 20, and 21. This series of locations compares inner and outer meridional rebars in a series near the base of the cylinder wall, which is a zone of significant flexure and shear. In general, the strains in the inner rebar layers agree fairly well with analysis and the outer rebar layers show more noticeable differences. The main reason for this may be simply that the outer rebar strains have quite small amplitudes, since the wall's vertical flexure tends to add tension on the inside and compression on the outside surfaces. It is often difficult to match a test measurement of very small amplitude (i.e., percentage differences may appear large, while in absolute terms, the differences are quite small). The predicted trends do appear to be reasonable, however. It should also be noted that the outer rebars that were gaged are likely to be very close to the neutral axis of bending in the section. Thus, if the analytical prediction of neutral axis location is only off by a few millimeters, the strain predictions immediately adjacent to this could be at large variance with the test model, or even have opposite signs. The inside bars are sufficiently far from the neutral axis of bending to prevent such sensitivity.

SOLs 22 and 23. These locations compare hoop and meridional rebar strain at the cylinder midheight. Agreement with analysis is generally good, although the hoop bar strains late in the test tend to be underpredicted. This difference has been attributed to rebar gage effects, as discussed in Chapter 3. The argument is that the analysis agrees well on radial displacements at this location, so by kinematics, it follows that the prediction of global hoop strain at this location is also good.

SOLs 24, 25, and 26. These locations compare a hoop rebar and an inner and outer meridional rebar at the springline. Again, the hoop rebar strain and inner rebar strain predictions show similar trends to the measurements, while the outer rebar strain is significantly overpredicted. The same observations made at the wall-base juncture apply here. Due to the radial stiffness differential between cylinder and dome, the springline is once again a point of significant meridional bending, with tension on the inside and compression on the outside. (This flexural component is in addition to the underlying tension caused by the pr/2t cylinder stress.) As an indicator, the measurements for the inside meridional bar reaches .0013 by the end of the test (3.3 Pd), while the measurement for the outside bar only reaches .00022.

SOL 27, 28, and 29. These rebar strain measurements in inner and outer hoop and meridional rebar show good agreement to analysis for the hoop rebar, but poor agreement for both meridional rebar. This observation and the dome displacement observation clearly show that the analysis overpredicted vertical deformations in the dome.

SOL 30, 31, 32, and 33. These comparisons are for the meridional (inner and outer) and hoop rebar at the 90 degree buttress. The comparisons of inner meridional rebar strain at the base of the wall are good (to within about 25%), while for the outer meridional rebars they are significantly overpredicted. The previous argument about local bending and proximity to the neutral axis may also apply here. The buttress hoop rebar strain at cylinder midheight is also significantly overpredicted.

4.3 Liner Strain Comparisons

Liner strain comparisons are made in Figures 4-10 through 4-13.

SOL 34, 35, 36, and 37. The first four comparisons are for strains near the wall-base juncture at azimuth 0 degrees and azimuth 135 degrees, inside and outside liner surface. At elevation 0.01 meters, the analysis shows a similar trend to the data, but overpredicts the magnitude. This comparison may be highly influenced by gage placement and by the location for extracting the analytical data. The location is within just a few millimeters of a sharp stiffness discontinuity. There is also some evidence in the test data that the liner base anchor may have begun to pull out of the concrete; if this indeed occurred, it would lessen the severity of the stiffness discontinuity and the meridional strains near the wall-base juncture. Unfortunately, the liner strain gages at azimuth 135 degrees were damaged by welding operations during the PCCV model construction, so the evidence supporting this hypothesis is limited. The meridional and hoop strain comparisons at 0.25 meters elevation show fair agreement. It is interesting to note that the hoop gages at 0.25 meters elevation show positive values during prestress and a negative trend during pressurization. This is counter to the rest of the cylinder and is likely caused by the reverse in vertical curvature that takes place at this elevation, and apparently is a Poisson Effect caused by wall flexure.

SOL 38 and 39. Hoop and meridional strain comparisons at cylinder midheight show similar trends. At approximately 2.8 Pd, the test data indicates significant yielding of the liner in the hoop direction. The analysis results also demonstrate a change in stiffness at this pressure, but not so sharply. Note that the analysis results are purely global response, taken from axisymmetric analysis, while liner strain measurements can be influenced by local details on the liner, such as proximity to stiffeners, weld seams, or even proximity to a concrete crack behind the liner.

SOL 40, 41, and 42. Hoop and meridional strain comparisons at the springline show good agreement (within ~10%) for hoop behavior, but the meridional strain, which is likely influenced significantly by vertical bending behavior, is overpredicted by analysis. This is consistent with the observed trend that vertical deformations in the dome were overpredicted by analysis. The meridional strain comparison at the dome apex shows fairly good agreement (within ~25%).

SOL 43 and 44. These locations compare meridional and hoop strain near the 90 degree buttress at the cylinder midheight. The hoop strain compares very closely, while the meridional strain is overpredicted.

SOL 45 and 46. These locations are intended to capture strain concentration locations near the thickened insert plate of the E/H and A/L, respectively. While at pressures lower than about 2.7 Pd, there is fair agreement with the measurements, clearly the local analyses predicted a strong strain concentration that did not occur in the test. This fundamental difference between the analytical predictions and the test is discussed later in detail.

SOL 47. This location is on the liner at the basemat, 100 mm inside the cylinder. While the strain comparisons at least show a similar trend, there are large differences in magnitude. However, the measured data and the analysis predictions are small, so quantities being compared are also small.

4.4 Tendon Comparisons

Tendon gage versus analysis (pressure histories) comparisons are made in Figure 4-14 and 4-15

SOL 48, 49, and 54. These locations compare strain and load cell force in two vertical (hairpin) tendons. The comparisons of strain are fairly good, while the comparison of load cell force is somewhat overpredicted.

SOL 50, 52, 53, and 55. These locations compare strain for hoop tendon H53 (mid-tendon, near buttress, and between E/H and A/L) and load cell force for hoop tendon H53. The strain comparisons generally show good agreement, except near the buttress, where the analysis overpredicted. The load cell force also shows reasonably good agreement.

An overview of comparisons of analytically predicted to actual tendon behavior is provided in Figures 4-16 through 4-22. These figures combine the test measurement information from load cells and the average of the wire strain gages.

The wire strain gage data was converted to force by SNL using the stress versus strain curves for the total tendon. These were provided in Ref. [8]. The analysis data for the hoop tendon comparisons is from the pretest 3DCM analysis. More hoop tendon comparisons are provided in Chapter 6 in the discussion on the 3DCM. The reader is also directed to those Figures (6-3 to 6-6) for the following discussion.

The hoop tendon data provides the following insights into the PCCV hoop tendon behavior and the predictions of behavior provided by the pretest 3DCM analysis.

1. The initial prestress anchor forces put into the pretest model have the same shape as the basic design friction assumption and roughly 9% lower magnitude. This 9% reduction from design values was incorporated to address the long term losses that occurred between initial seating and the LST. This strategy for initial anchor force, on average, agrees well with the tendon anchor force measurements taken just prior to LST pressurization. These observations are based on comparing the "Analysis @ 0.000" anchor force data to the data points at "9/26/00 10:03 0.00." At H11, H35, H53, H67, and H68, the zero pressure anchor forces are generally in good agreement with the analysis, and are generally 5% to 10% lower than the design assumptions.

2. The shape of the tendon stress distribution at the start of the LST also shows a similar trend compared with measurements, implying that the angular friction and anchor set modeling assumptions at the start of the test (which were made based on standard design assumptions) were reasonable. There is some scatter in the level of agreement, however. Tendon H11 shows about 20% less angular friction loss than assumed, while H35, H53, and H67 show much closer agreement. H68 also shows some scatter in the measured friction loss profile.

3. Some of the hoop tendon stress distributions during pressurization showed poor agreement with the pretest analysis. This is based on comparing the analysis curve at 1.17 MPa (3.0 Pd) to the data at 1.162 MPa. While H11 and H53 show fair agreement at the "interior" gages, the anchor forces are significantly over-predicted. Higher on the cylinder (H53 and H67), the interior gages are underpredicted *and* the anchor forces are overpredicted.

4. The cylinder hoop tendon data, in total, shows evidence of changes in friction orientation (i.e. tendon slipping) during pressurization. H53 and H67 show this particularly well. The data indicate that the shape of the tendon stress profile changes during pressurization. The total force increase on the plot is equivalenced to a hoop strain derived from the radial expansion of the cylinder (i.e., H53 $\Delta\varepsilon$=0.48% and H67 $\Delta\varepsilon$=0.45%, while hoop strain from radial expansion is significantly lower at 0.35% and 0.37%.). This implies that portions of the tendons are slipping to accommodate the higher deformation at other azimuths.

The vertical tendon data (Figures 4-17 through 4-22) provide the following insights.

1. As with the hoop tendons, there was about 8% to 10% loss occurrence between the initial prestressing and the start of the LST caused by long term effects and by the System Functionality Test (SFT) and SIT. This is evidenced in Figures 4-17 and 4-18 for tendon V37, Figures 4-19 and 4-20 for V46, and Figures 4-21 and 4-22 for V85. Only V85 showed significant friction losses above the springline, and the other two gaged vertical tendons showed only about half of the friction loss in the dome than what was assumed by the designers and incorporated in the analysis.

2. Comparisons with the axisymmetric analysis show that assuming no friction along the straight portion of the tendon and much smaller friction in the dome would provide improved simulation of the vertical tendon behavior. (As discussed in Chapter 5, this justifies returning to the 1999 axisymmetric analysis as the better vertical tendon simulation.)

4.5 Wall-Base Juncture Shear Behavior

Another local area of the PCCV model that was studied in detail was the wall-base juncture [1]. Some relatively large concrete strains, driven by shear and flexure were predicted to occur as shown in Figure 4-23, but no failure associated with the shear and flexure mechanism was predicted until P > 4.0 Pd, much larger than the 3.3 Pd reached in the LST. Nevertheless, it is of interest to compare special rebar and liner strain measurements taken in the wall-base juncture area

to the pretest analysis. Since it was concluded during the posttest work that the 1999 pretest model provided the more appropriate simulation of the true vertical tendon stresses, and since this modeling detail has significant influence on the wall-base juncture behavior, the comparisons to the test are only made to the 1999 predictions.

Because this area was identified as having a high potential for large strains and liner tearing in the preliminary analysis, a significant effort was made to instrument the liner and wall at several azimuths. Specially fabricated 'gage bars' (not part of the model reinforcing) were installed through the thickness of the wall in an attempt to monitor the local strain distribution. Unfortunately, many of the gages installed on the liner and the gage bars were damaged during construction or subsequent water penetration and were not functional during the LST. The typical arrangement of liner strain gages at the wall-base juncture are shown in Figure 4-24. The 'gage bar' strain gages installed in the area are shown schematically in Figure 4-25. Fortunately, a large number of gages survived at the 135 azimuth, which was chosen to represent the axisymmetric behavior of the model. During the test, many of these gages were monitored in real time using this display screen. The gage numbering shown on the screen is tabulated in Table 4-2. A labeling scheme that facilitates analysis versus test comparisons is shown in Figure 4-26.

Table 4-2. Gage Identification for the Basemat Junction Display Screen

Number on Screen	Gage Name
1	GB-M-Z1-05
2	GB-M-Z1-10
3	RS-R-Z2-02
4	GB-M-Z1-15
5	GB-M-Z1-20
7	GB-M-Z1-09
8	RS-R-Z2-01
9	GB-M-Z1-14
10	GB-M-Z1-19
11	GB-M-Z1-03
13	RS-R-Z-1-02
14	GB-M-Z1-13
15	GB-M-Z1-18
18	RS-R-Z1-01
20	GB-M-Z1-22
24	GB-M-Z1-21
25	RS-M-Z2-01
26	RS-M-Z2-02
27	RS-M-Z1-01
28	RS-M-Z1-02
38	RS-M-Z0-13
39	RS-M-Z0-14

Comparisons between wall-base area liner and rebar strain gages are provided in Figures 4-27 through 4-49. The analysis data was zeroed to the experimental measurements, but a specific gage had to be selected for this zeroing. Which gage was selected is clear from observing which data/gage history curves "match" at P=0. The liner strain comparisons near the base of the wall (Figures 4-27 through 4-32) show similar trends to the analysis. When two liner positions are shown (i.e., B, C, etc.), this is provided to straddle strain gage locations that occur between the two analysis liner locations. Thus, often a particular gage will agree well with one of the pair of analysis points or with an average of the two. In general, the agreement shows that the wall-base liner behavior was well simulated by the analysis.

The level of correlation with the rebar gages (Figures 4-33 through 4-49) was not as good, but such was the case in comparing "free-field" rebar strain data, as well. As described in Chapter 3, in general the rebar strain measurements, upon reaching yield ($\varepsilon \cong 0.002$), tend to significantly overstate the actual strain. It is also quite difficult to pinpoint an analysis location that coincides with a rebar strain gage location. Nevertheless, some of the gages show quite good agreement with analysis. These include Axisymmetric Position D compared to GB-M-A1-04 (Figure 4-34), midway

between Positions E and J versus GB-M-Z1-05 (Figure 4-35), Position D vs. GB-M-Z1-10 (Figure 4-38), and Position V (in flexural compression) vs. GB-M-Z1-22 (Figure 4-43) and Position W vs. GB-M-Z1-18 (Figure 4-44). These are all vertical bars, indicating that the analysis captured the wall-base flexure behavior reasonably well.

Figures 4-46, 4-47, 4-48, and 4-49 compare stirrup strains. In general, these would be extremely difficult to match with analysis because stirrup strains are so influenced by the precise location of a major shear crack. Nevertheless, Figure 4-48 for stirrup location AB (shown in yellow on Figure 4-26, at about Elev. 12 inches) shows similar behavior to the gage measurements, indicating that shear behavior was simulated reasonably well. Note that all of the stirrup strains (measured and predicted) are well below yield, indicating that at the end of the LST (3.3 Pd), the model is far from developing shear failure.

4.6 Failures: Predicted and Observed

The 3DCM model predicted rupture of hoop tendons near the E/H with strains exceeding 5% at a model pressure of about 3.5 Pd[1]. However, this mode was predicted to be precluded by the liner tearing and leakage failure mode associated with the local models. The failure pressure at which a local analysis computed effective plastic strain that reached the failure strain of approximately 16% was 3.2 Pd, or 1.3MPa. The location for this liner-tearing failure was near the E/H, adjacent to a vertical liner anchor that terminated near the liner insert plate transition. Other local models showed other candidate liner tear locations, several of which were predicted to occur during the pressure range 3.2 Pd to 3.5 Pd, if they were not precluded first by the growth of the first tear and subsequent depressurization of the vessel. Significant candidate tear locations were also predicted near weld seams with hoop stiffener rat-holes, for example, near the 90-degree buttress where hoop strains are elevated due to circumferential bending. Failure at such locations was predicted to occur shortly after the E/H location.

As discussed in detail in Chapter 8, this last type of tear location was the predominant failure mode observed in the LST. Liner tears occurred in 16 locations, and there is evidence (acoustic and pressure/leak-rate measurements) supporting approximately 2.5 Pd as the pressure of the first tear initiation. Although predicted as a general failure mode, the specific location and pressure were not predicted. The following chapters discuss and present conclusions as to why these specific tear events were not explicitly predicted and why the strain predictions at the highest strain location of the pretest analysis was significantly overpredicted.

While the scope and objectives of the pretest analysis work for the 1:4-scale PCCV did not include a formal probabilistic risk assessment of the failure (leakage) pressure prediction, the final probability of liner tearing/leakage versus pressure was described in probabilistic terms with reference to the final list of candidate tearing locations. Combining probabilities and locations produced the following leakage pressure predictions and confidence intervals, which were published prior to the test. Best estimate (Probability = 0.5), $P_{leakage}$=3.2 Pd=1.3 MPa; upper bound (Probability = 0.9), $P_{leakage}$=3.5 Pd=1.4 MPa; lower bound (Probability = 0.1), $P_{leakage}$=2.75 Pd=1.1 MPa. Referring back to the pretest report where these were derived, the first leakage occurred below the 10% probability. This was an unacceptable prediction, but is easily explained by the presence of extensive flaws near weld seams. Such flaws probably can and should be considered in containment probabilistic calculations. Discussion of these issues as they relate to the test observations is also provided in later chapters.

4.7 Discussion and Conclusions of Analysis vs. Test Comparisons

A good overview of the test versus analysis comparisons in this chapter can be made by combining the response history information into deformed shape comparison plots. This information is provided in Figures 4-50 through 4-53. The plots show displaced shape along a horizontal slice (at Elev. 4.68 m) and three vertical slices (at 135, 324, and 90 degree azimuths) at various pressures compared to analysis. The overall conclusions from these and other comparisons in this chapter are as follows.

- Radial displacements were well predicted by global axisymmetric analysis, but dome and overall vertical displacements were significantly overpredicted.

- Based on the gages available, the wall-base juncture behavior appears to have been well predicted by the detailed wall-base juncture (axisymmetric) modeling.

- Maximum pressure (187.9 psig (3.30 Pd), which was primarily a function of the onset of global yielding, was closely predicted by analysis, but the predicted failure mode did not manifest itself. Note that the maximum pressure achieved during the LST was also limited by the capacity of the pressurization system to balance the increasing leak rate after functional failure occurred.

- An initial small leak occurred at 2.5 Pd that was not predicted by analysis, but this probably occurred due to defects associated with weld seam repair.

- Average radial displacement reached 23mm at 3.3 Pd
  - Average hoop strain = 0.0040 (well predicted by global analysis).

- Maximum radial displacement at E/H = 29mm at 3.3 Pd
  - Equivalent hoop strain = 0.0054 (reasonably well predicted by 3DCM, but prediction of some displacements at other azimuths — like the buttresses — was poor).

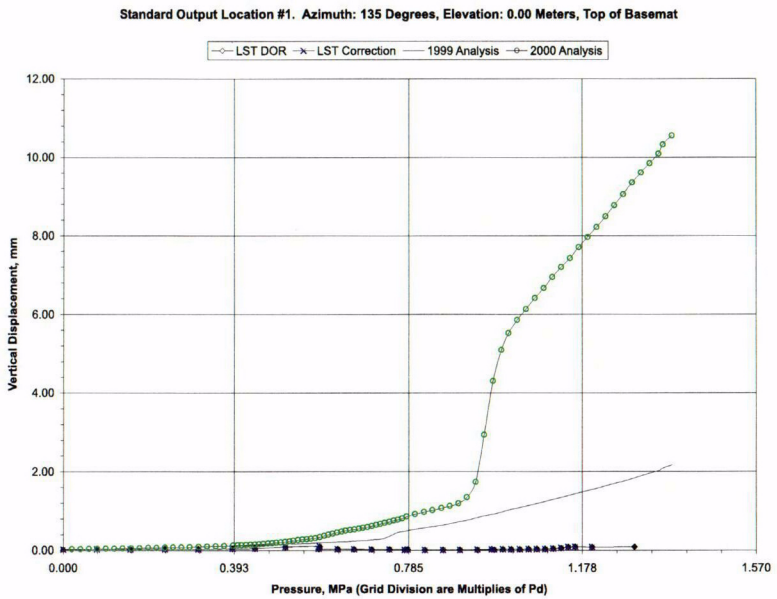

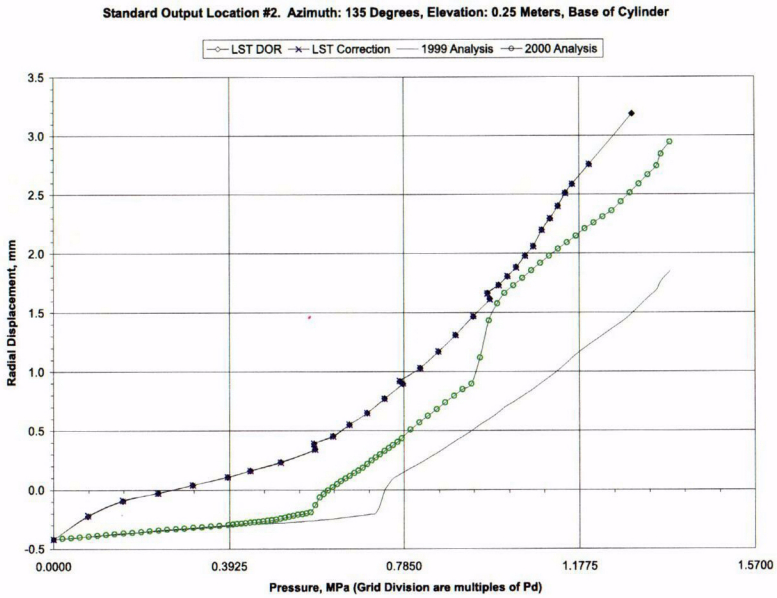

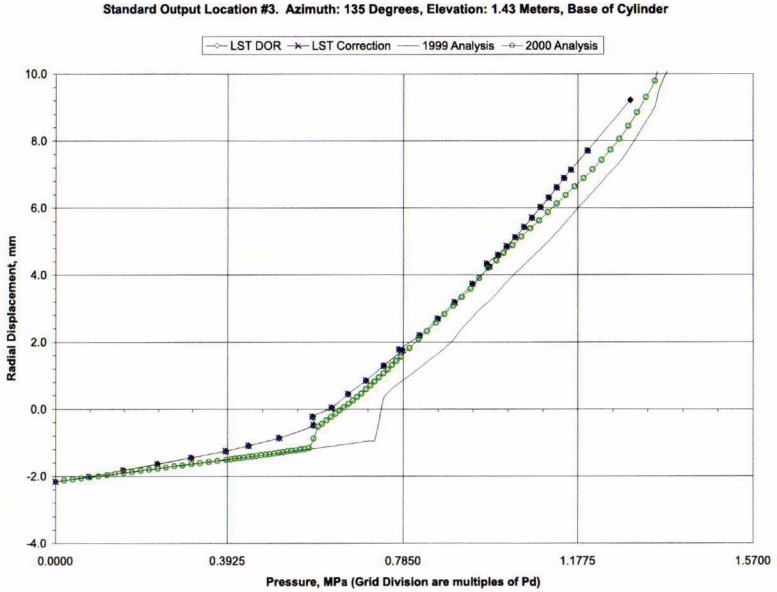

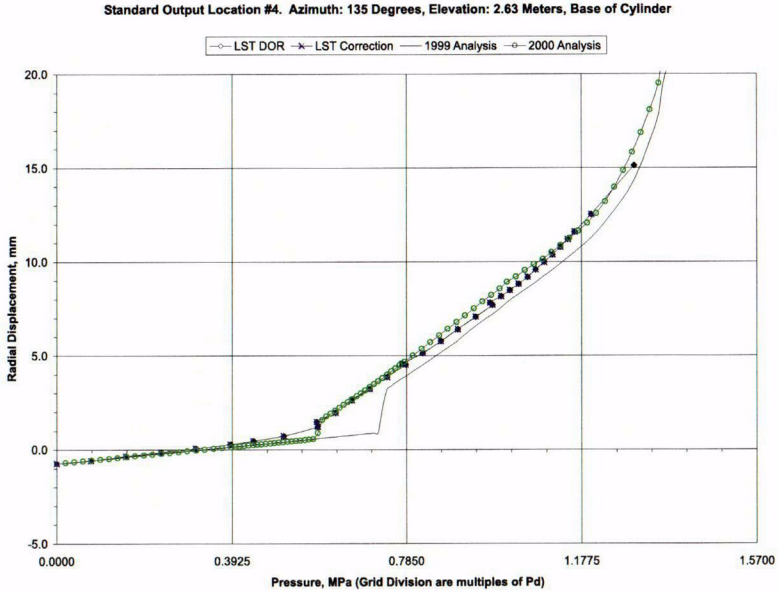

Figure 4-1. Comparisons at Standard Output Location 1, 2, 3, and 4

C09

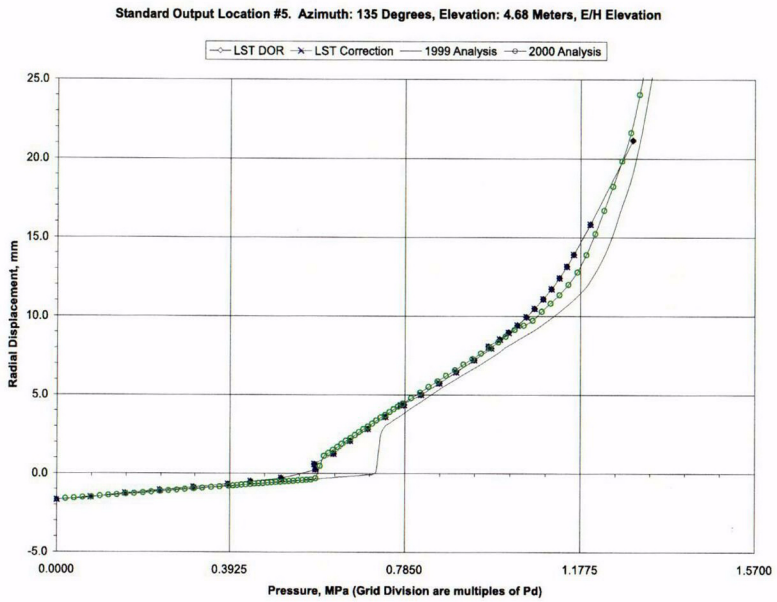

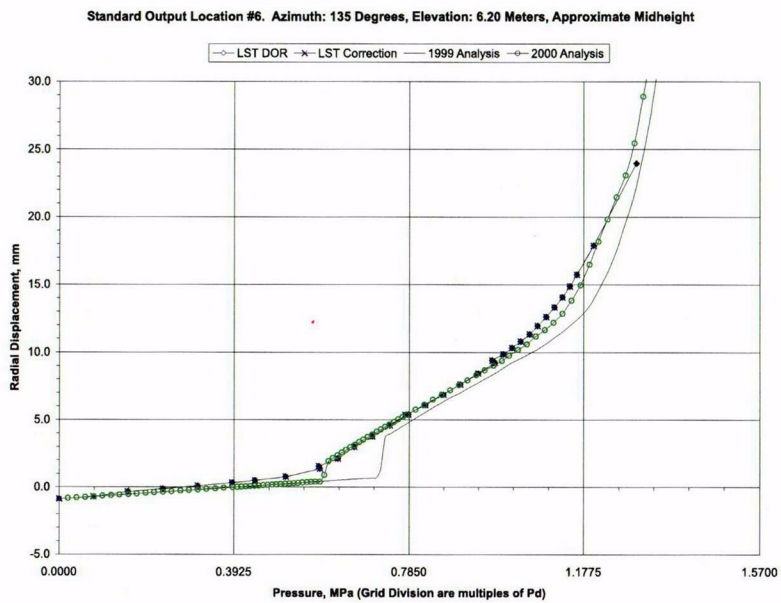

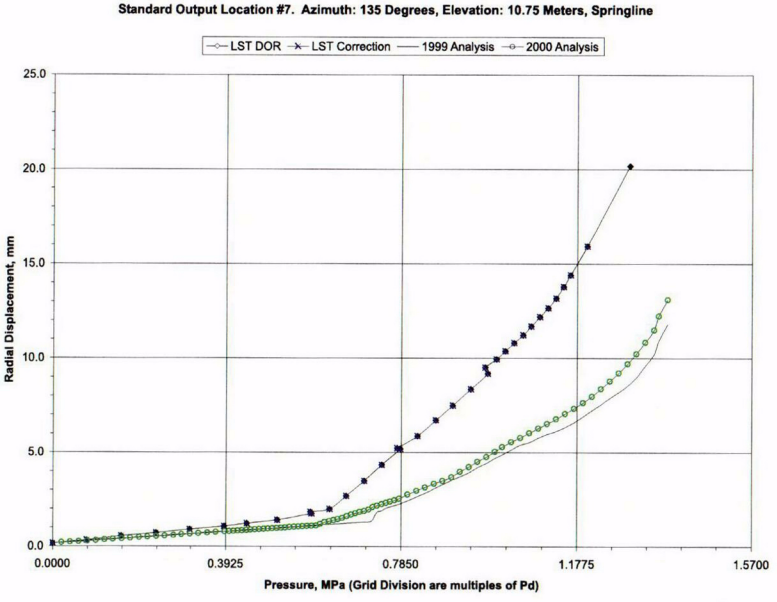

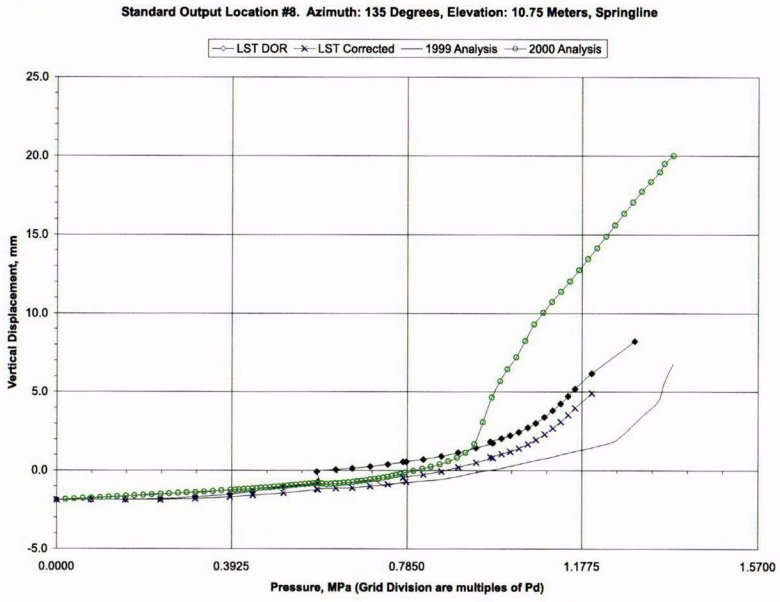

Figure 4-2. Comparisons at Standard Output Location 5, 6, 7, and 8

C10

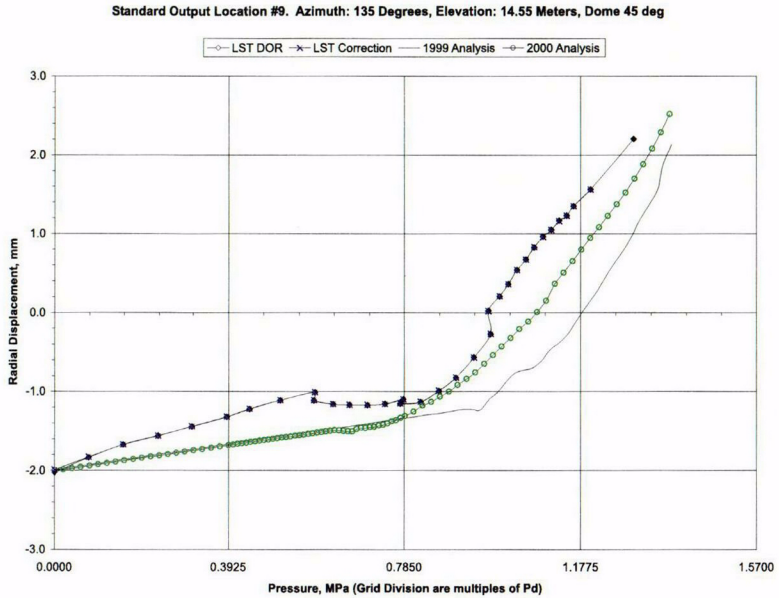

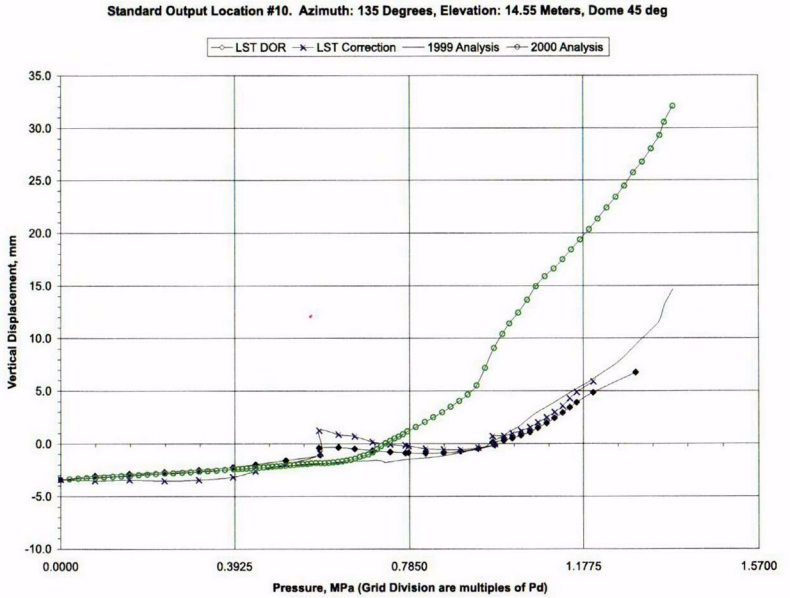

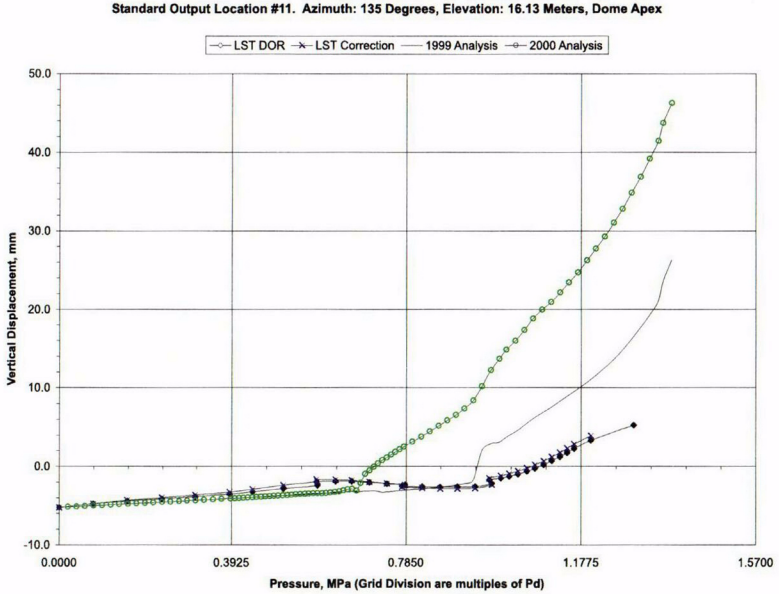

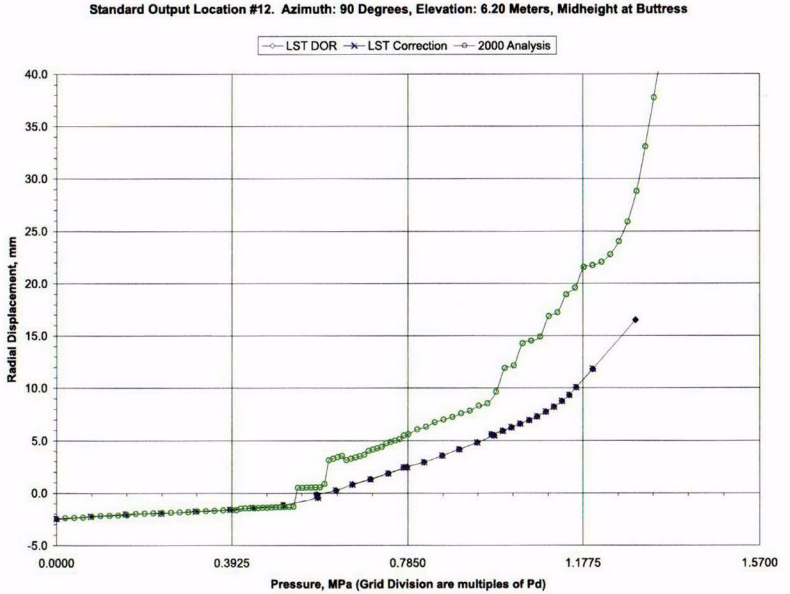

Figure 4-3. Comparisons at Standard Output Location 9, 10, 11, and 12

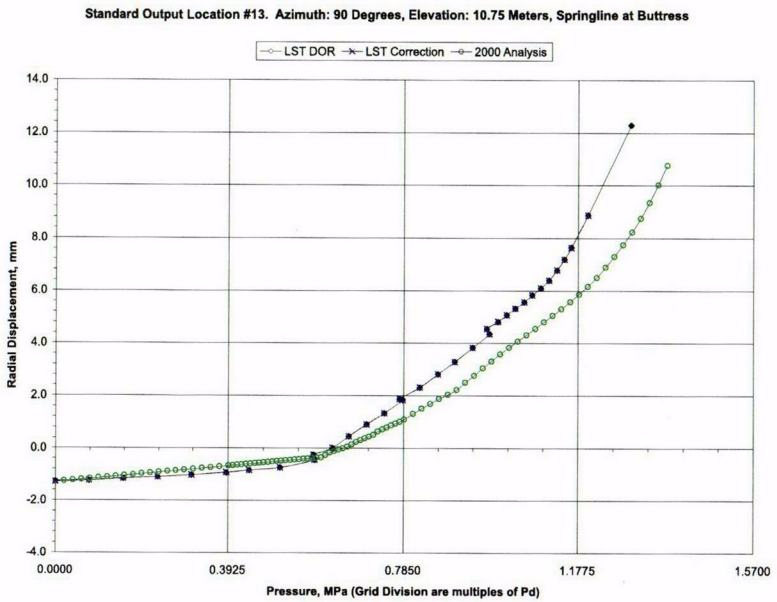

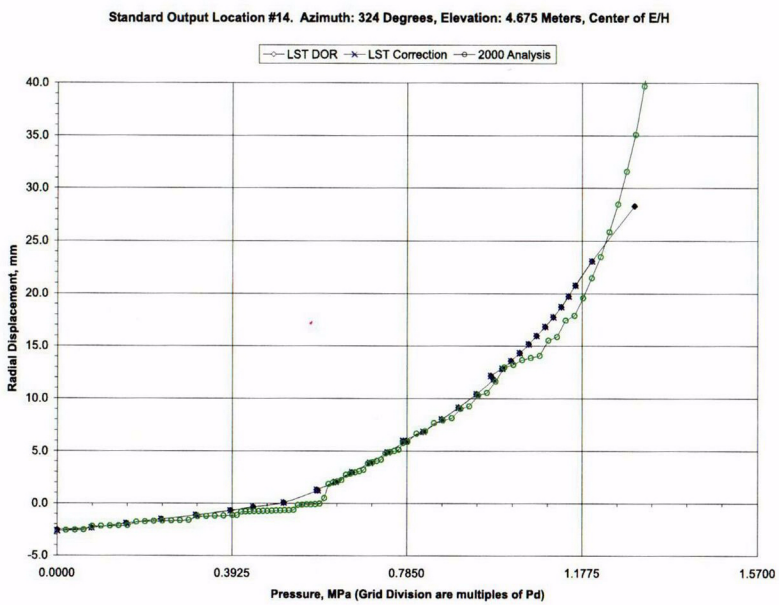

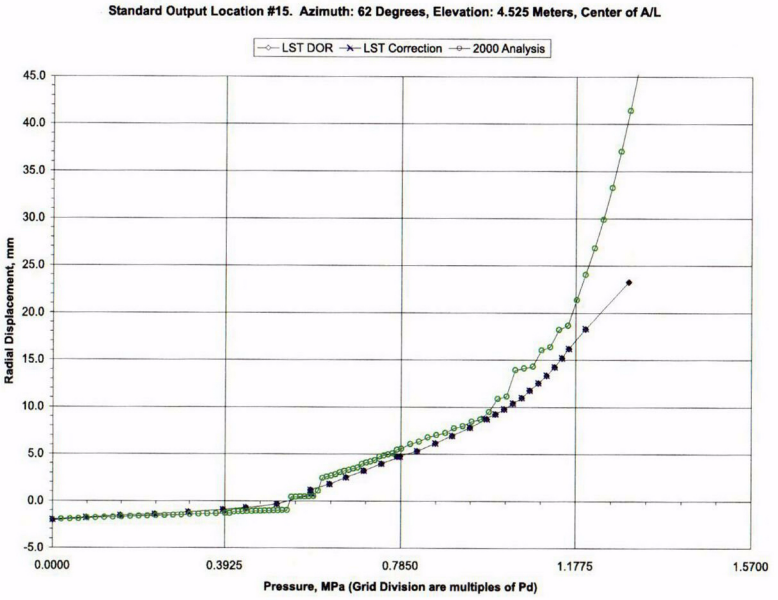

Figure 4-4. Comparisons at Standard Output Location 13, 14, and 15

C12

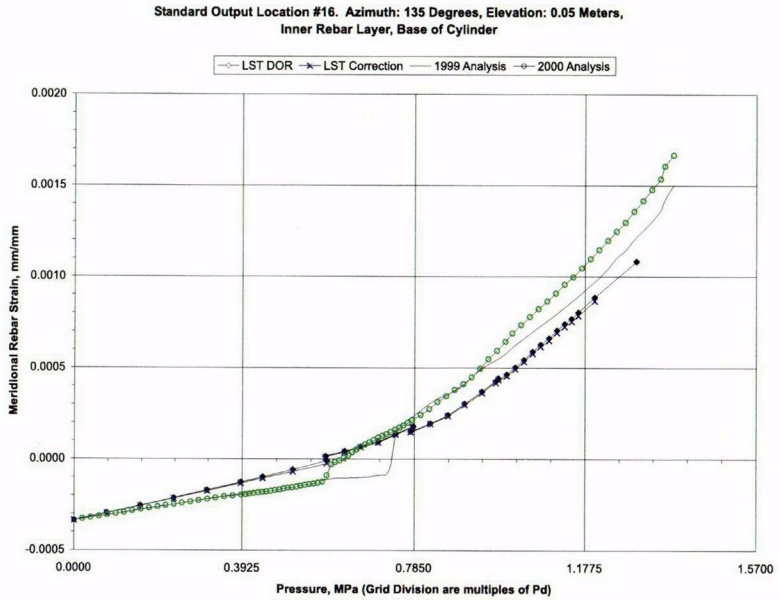

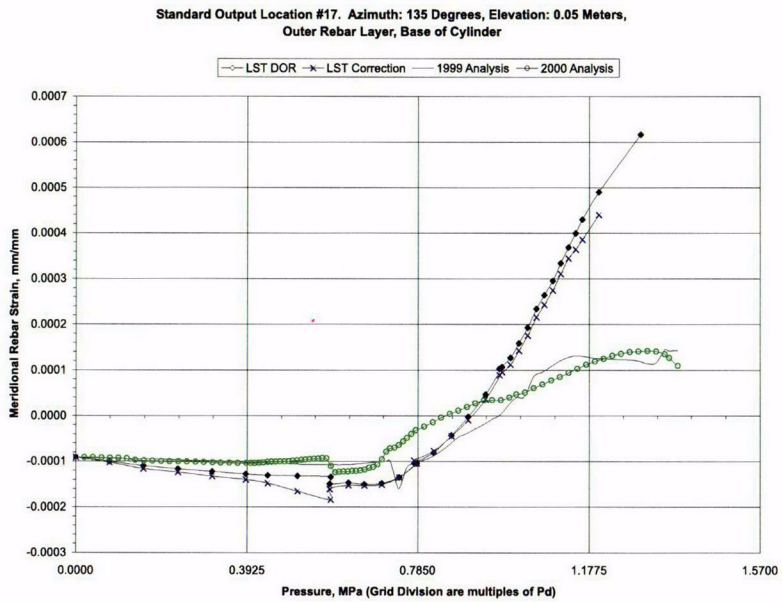

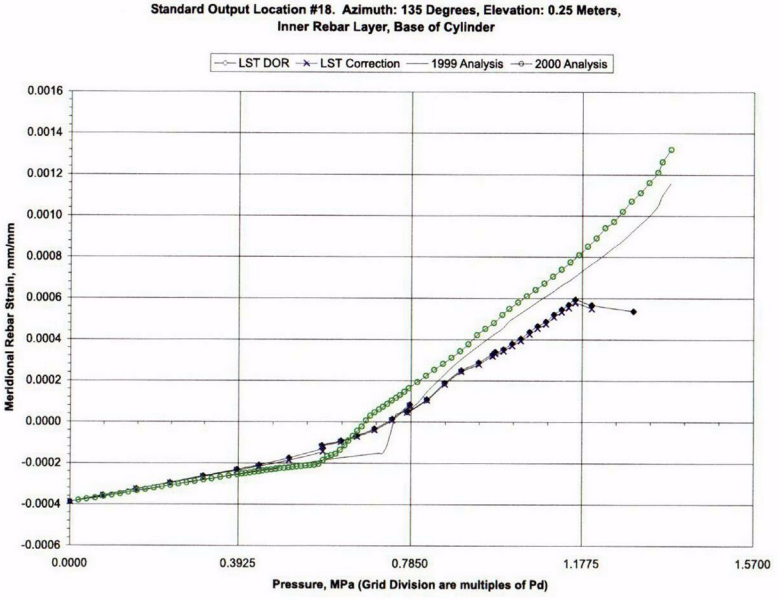

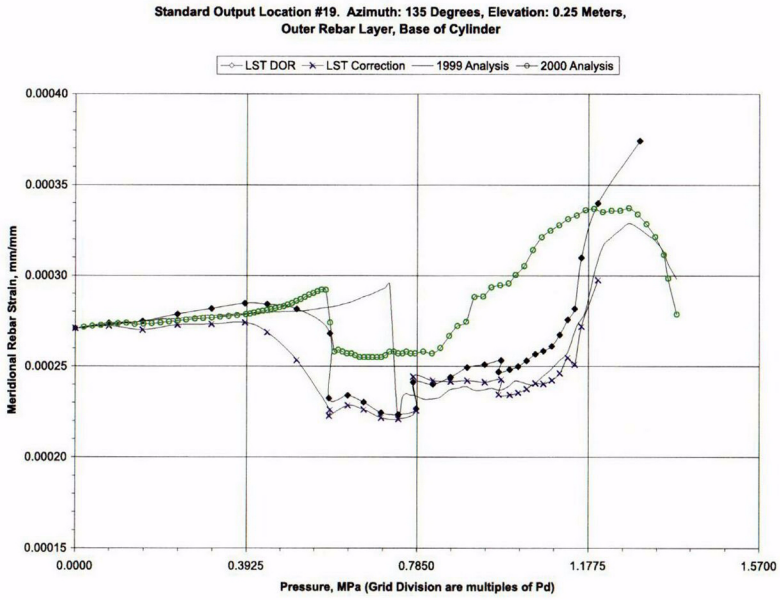

Figure 4-5. Comparisons at Standard Output Location 16, 17, 18, and 19

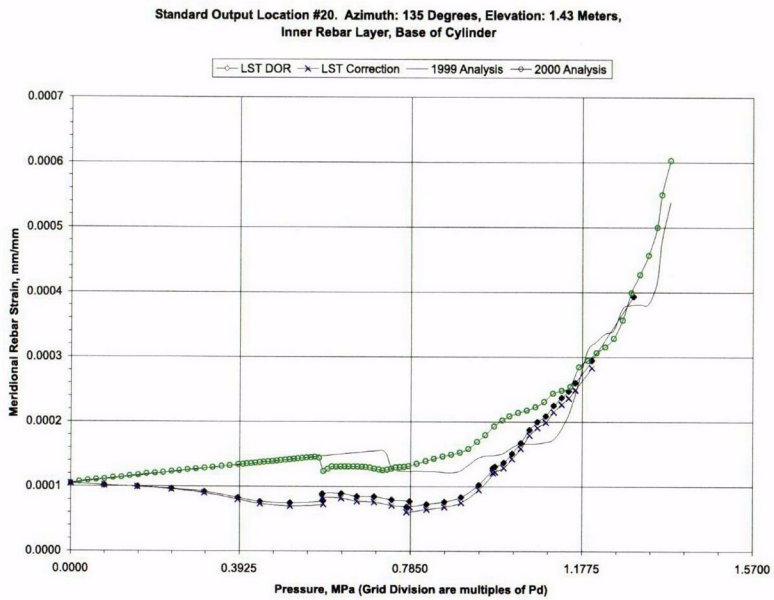

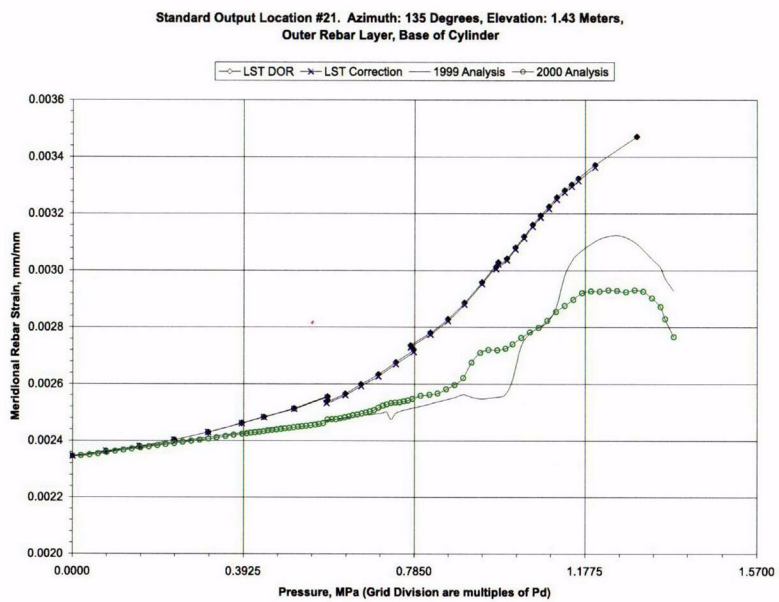

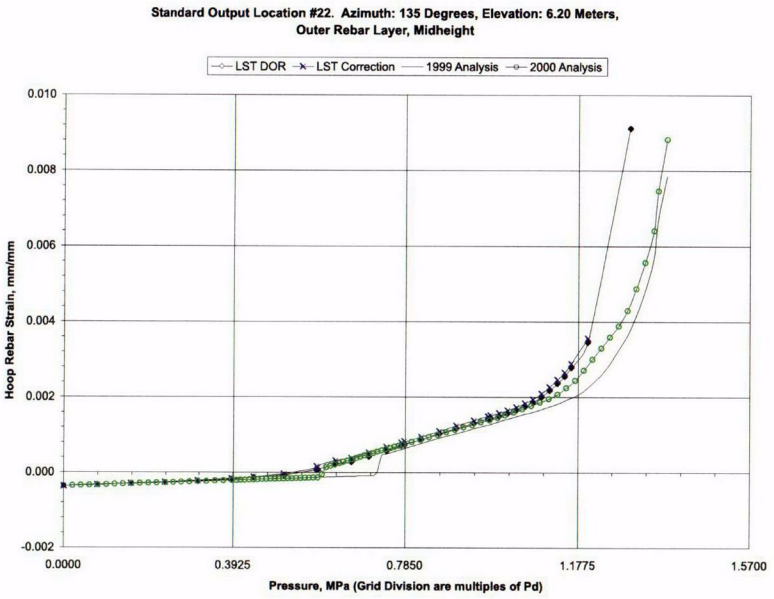

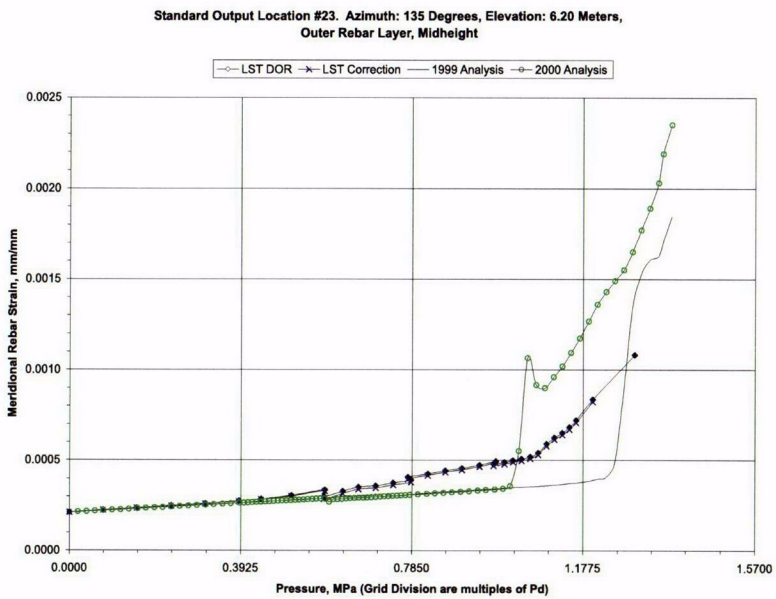

Figure 4-6. Comparisons at Standard Output Location 20, 21, 22, and 23

C14

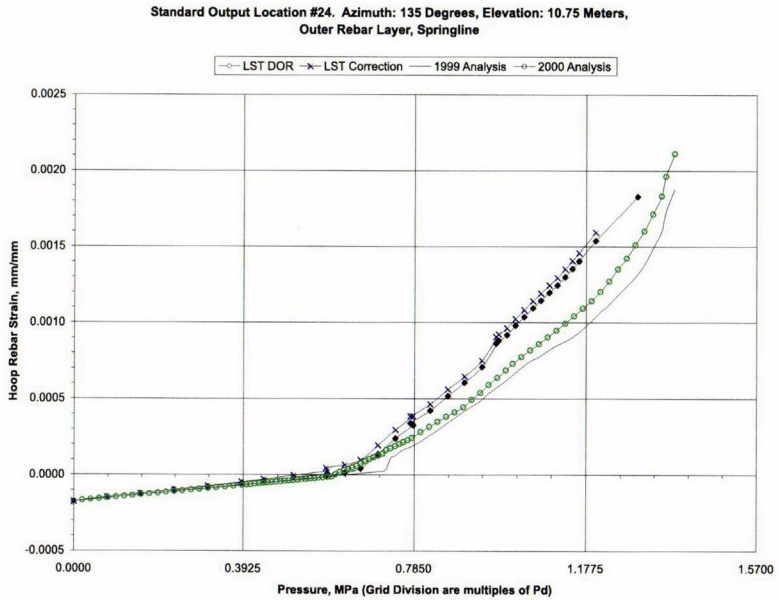

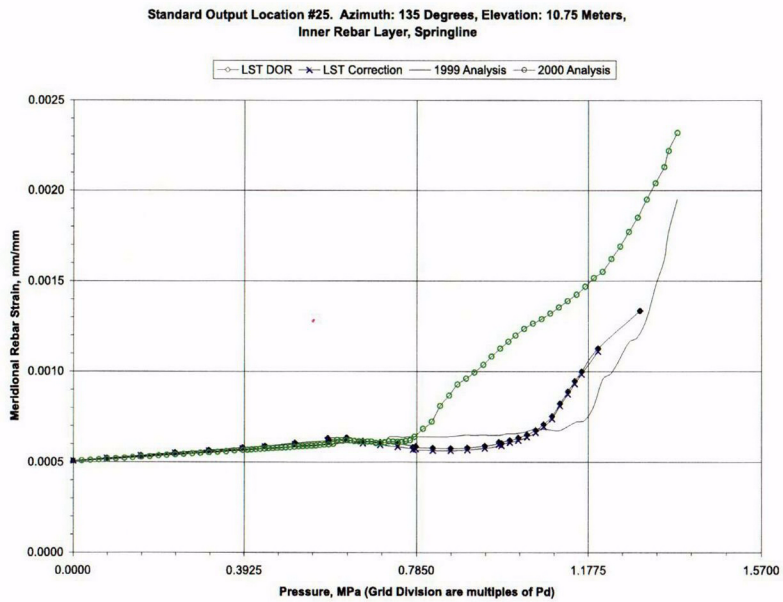

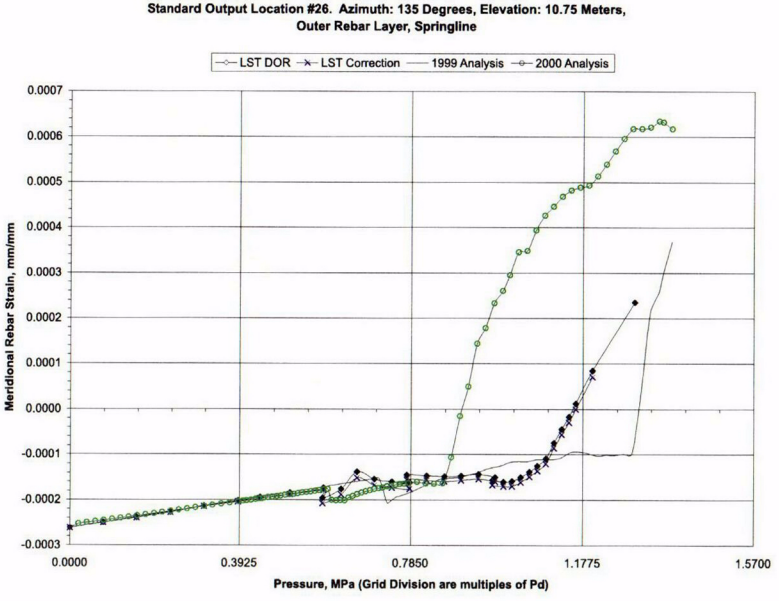

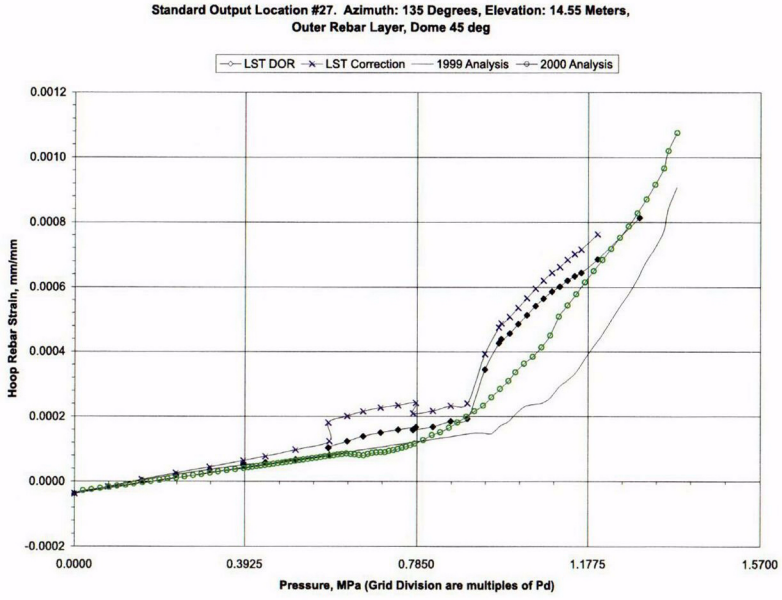

Figure 4-7. Comparisons at Standard Output Location 24, 25, 26, and 27

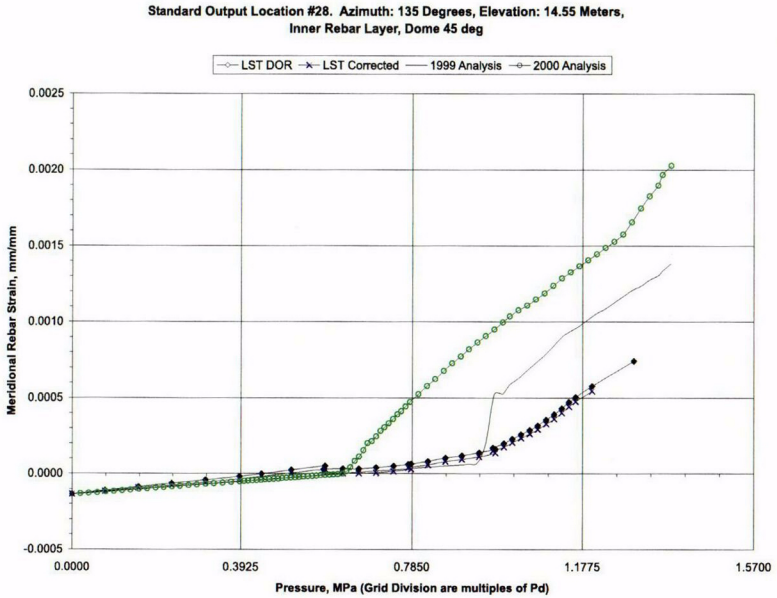

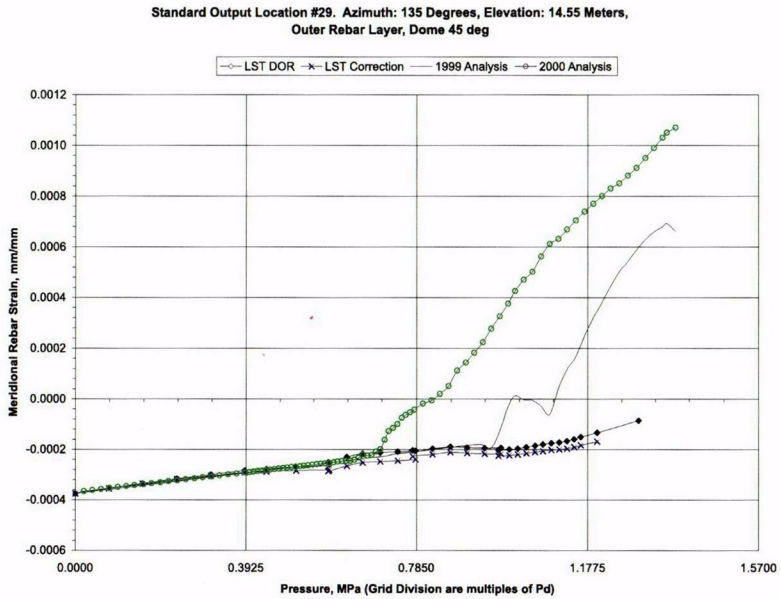

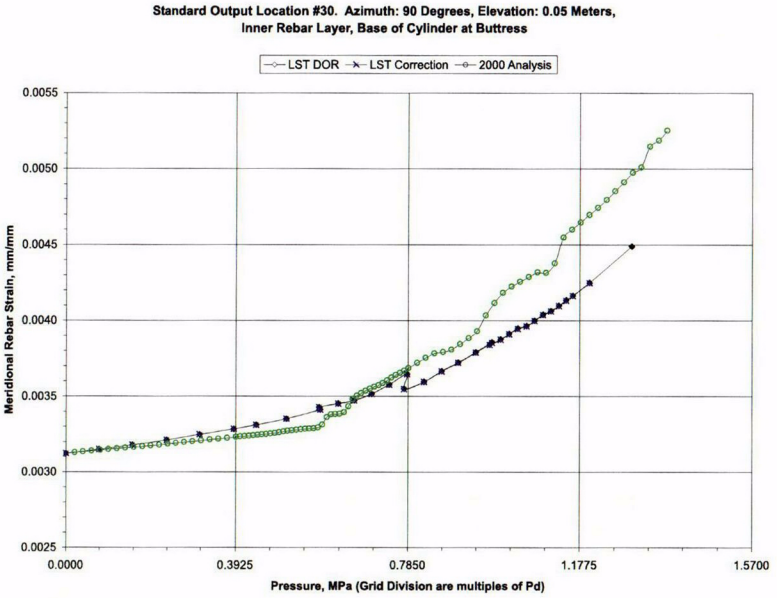

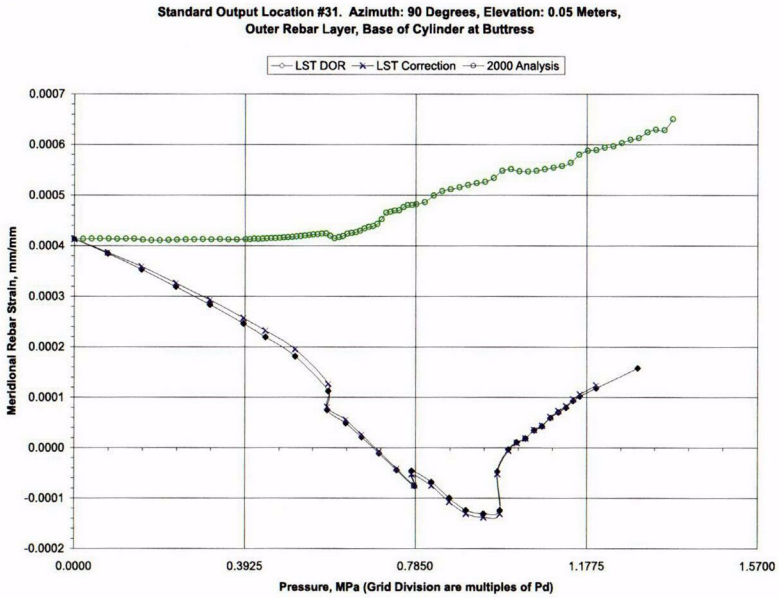

Figure 4-8. Comparisons at Standard Output Location 28, 29, 30, and 31

C16

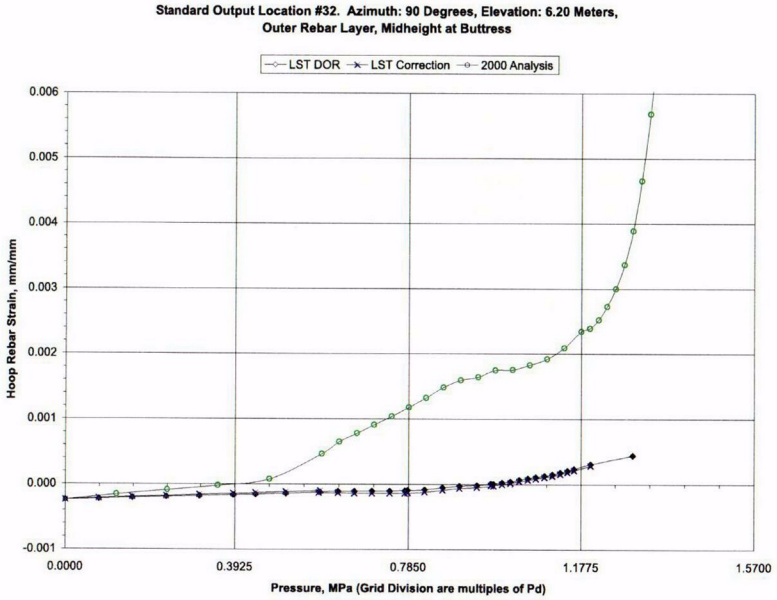

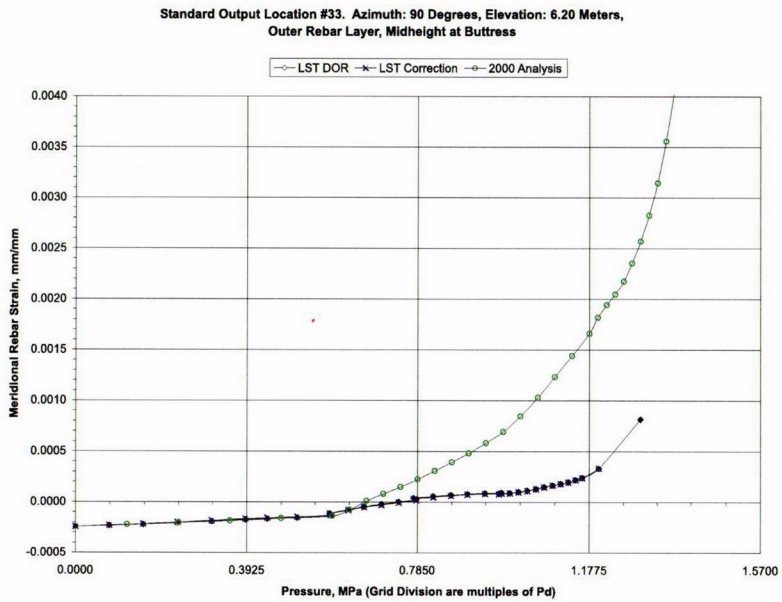

Figure 4-9. Comparisons at Standard Output Location 32 and 33

C17

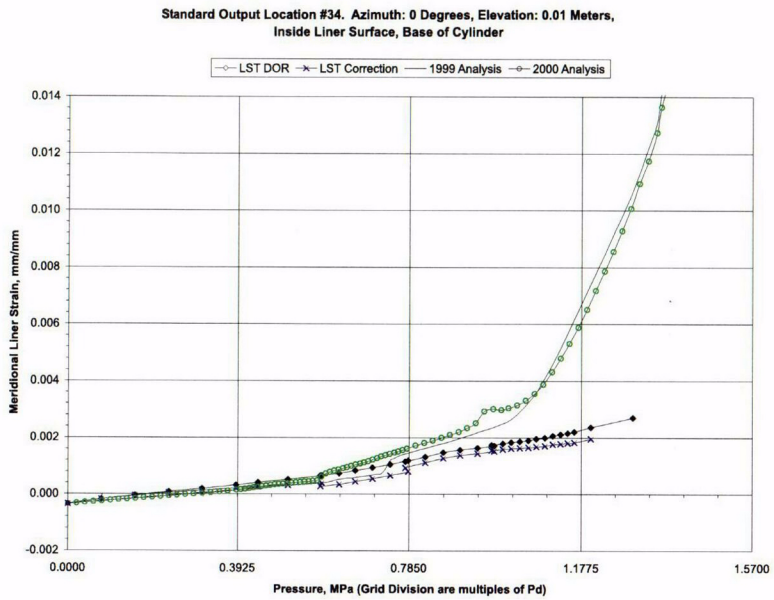

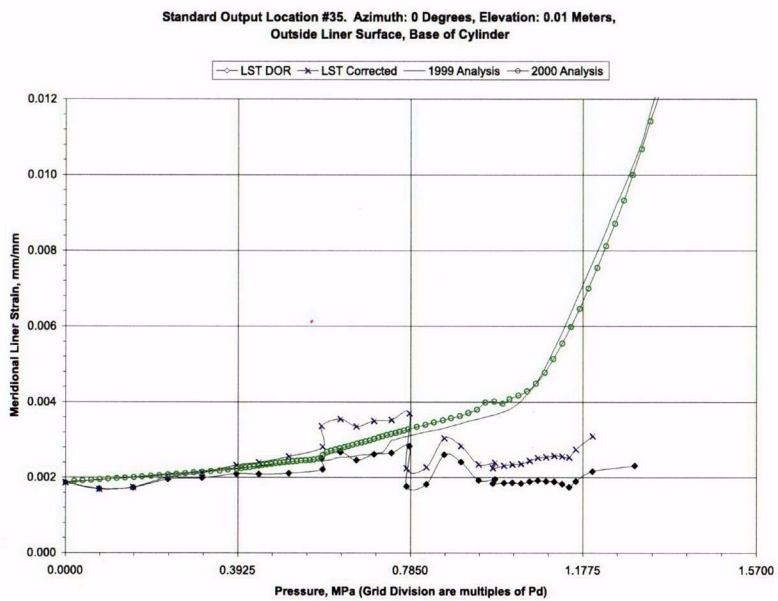

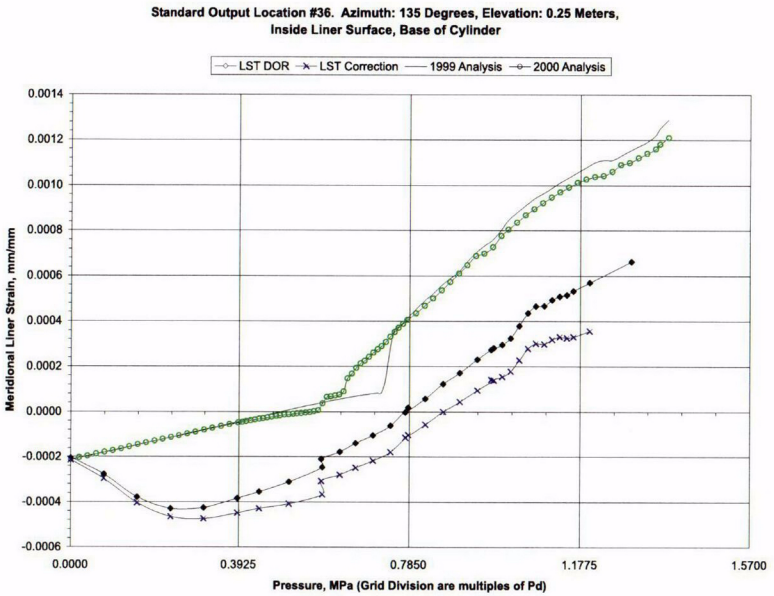

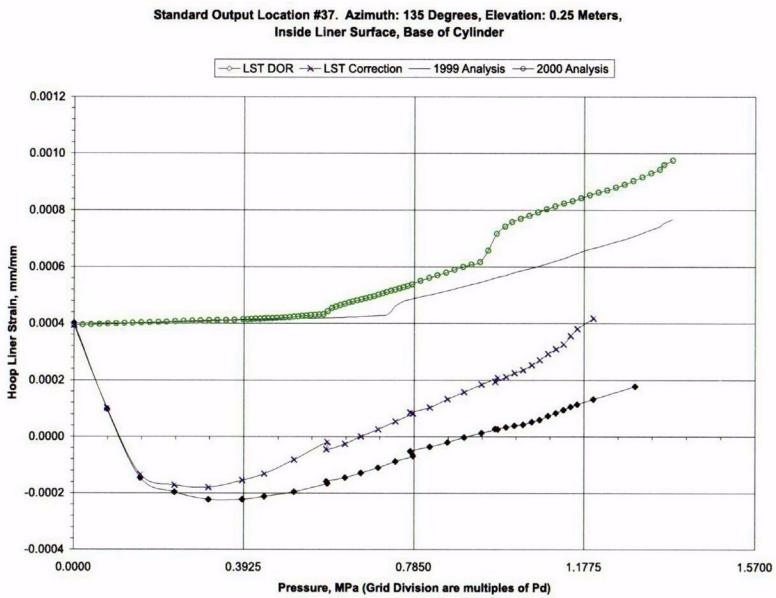

Figure 4-10. Comparisons at Standard Output Location 34, 35, 36, and 37

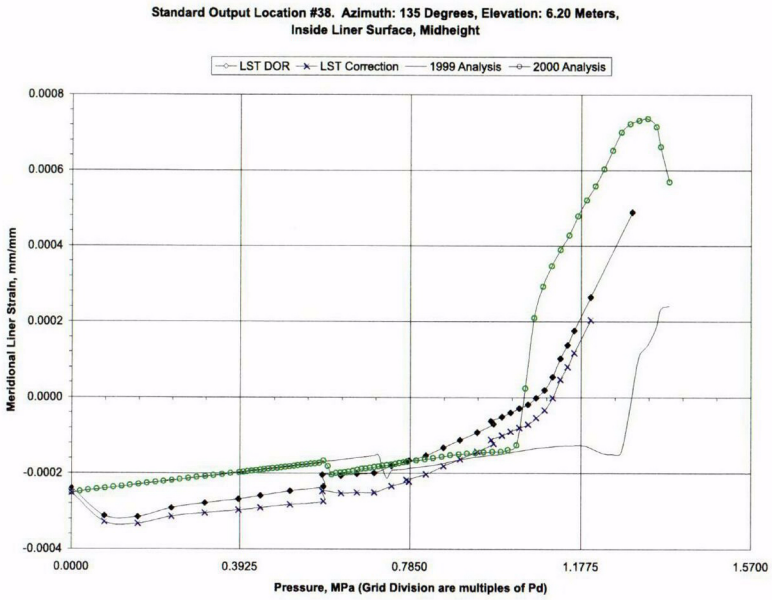

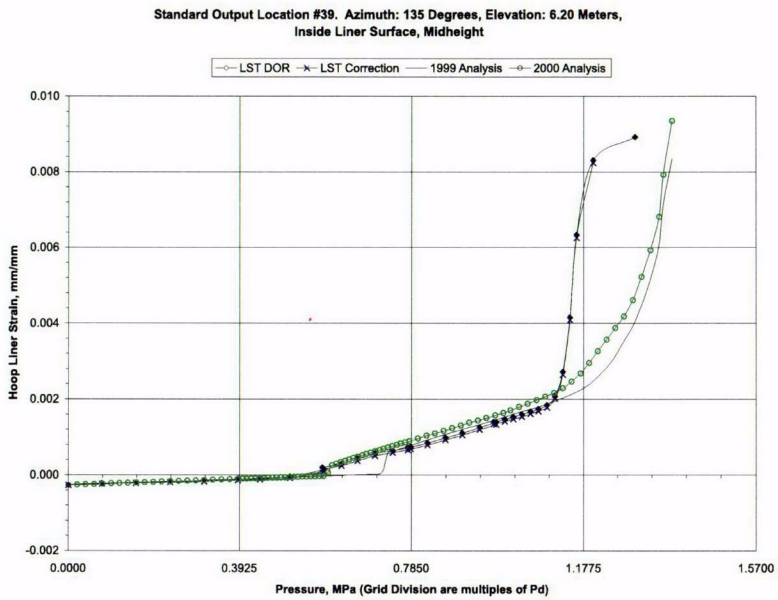

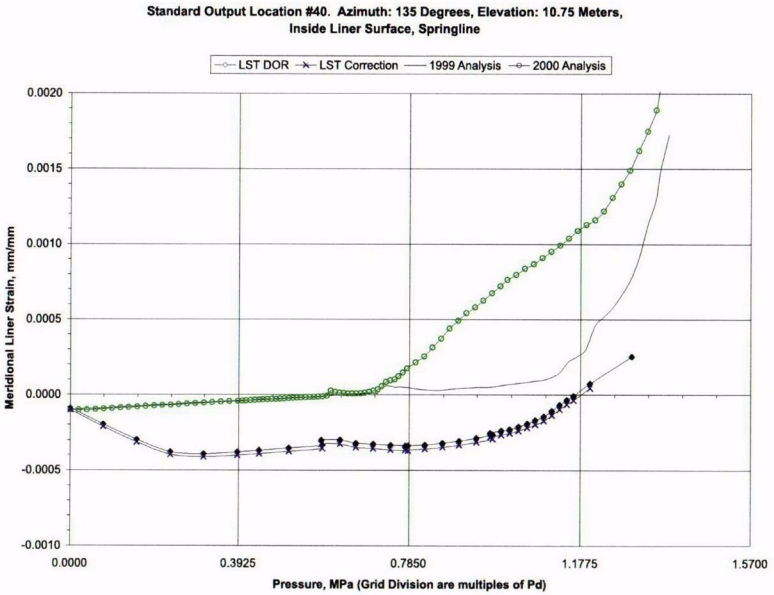

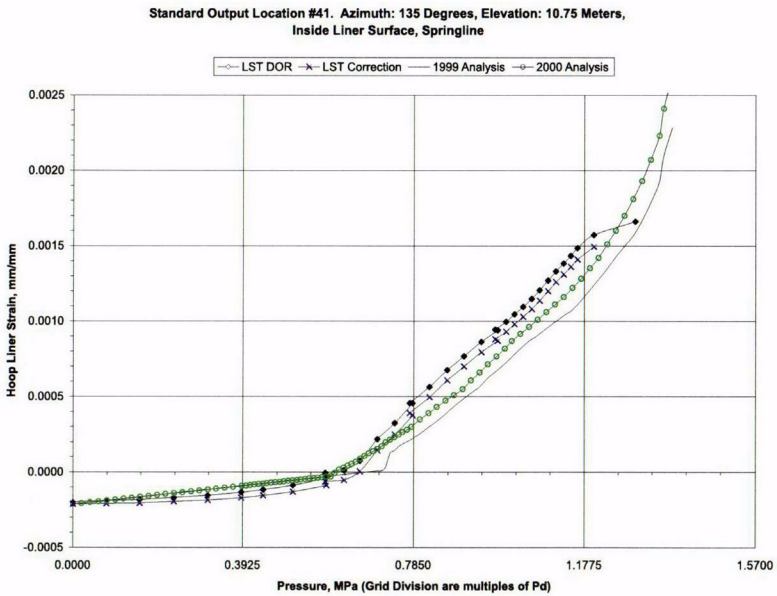

Figure 4-11. Comparisons at Standard Output Location 38, 39, 40, and 41

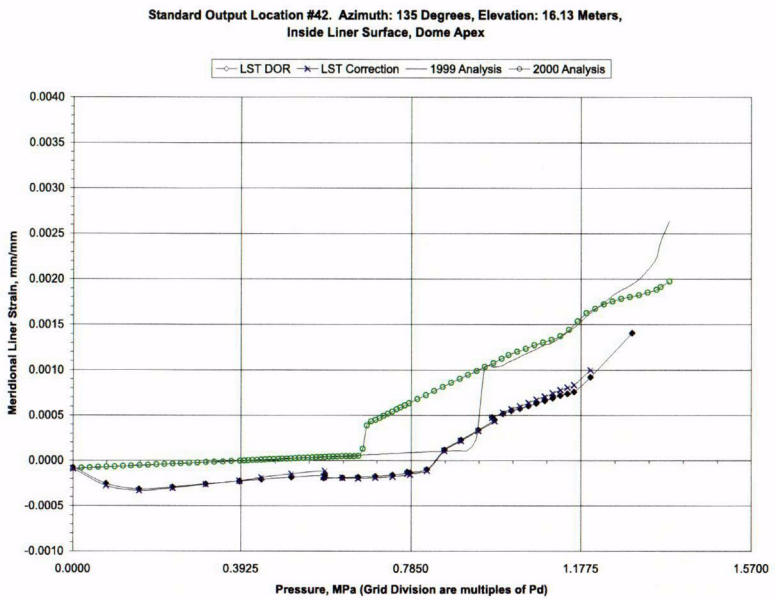

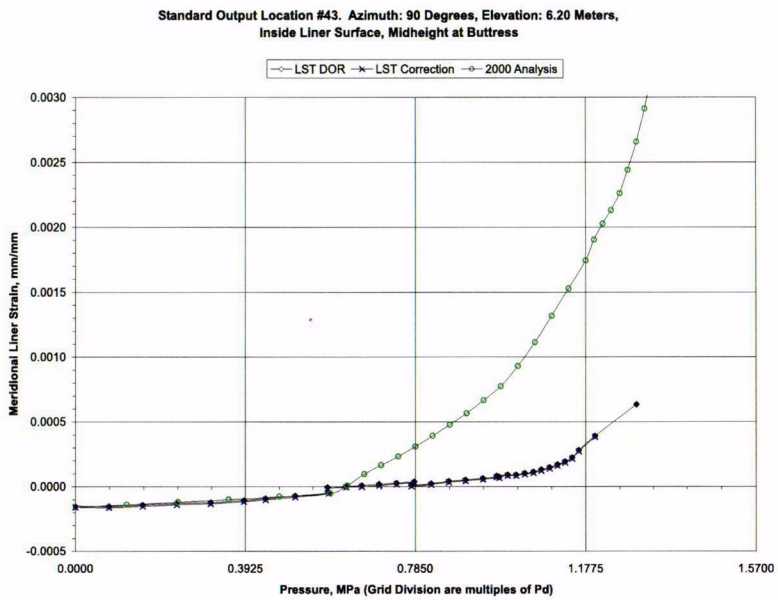

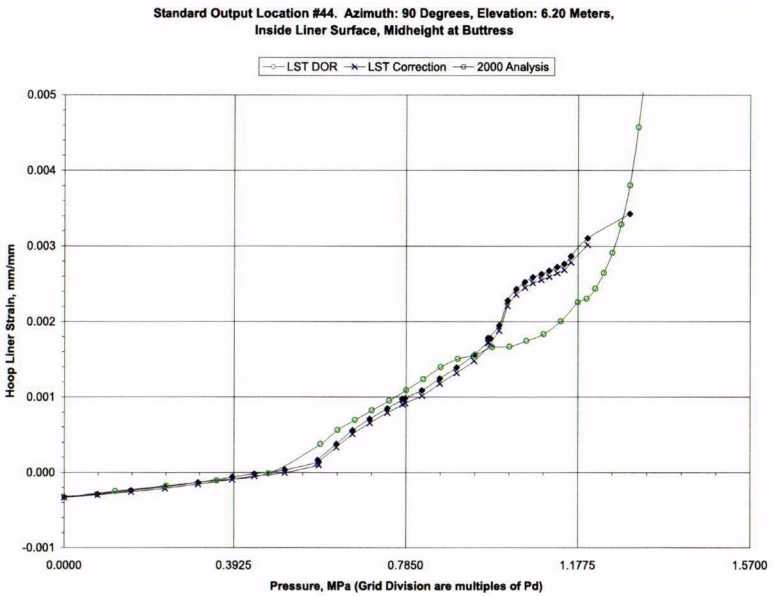

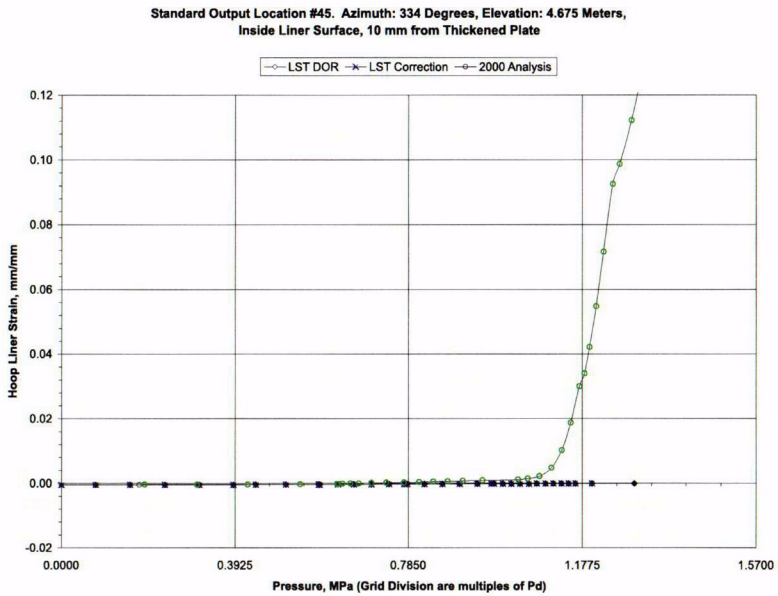

Figure 4-12. Comparisons at Standard Output Location 42, 43, 44, and 45

C20

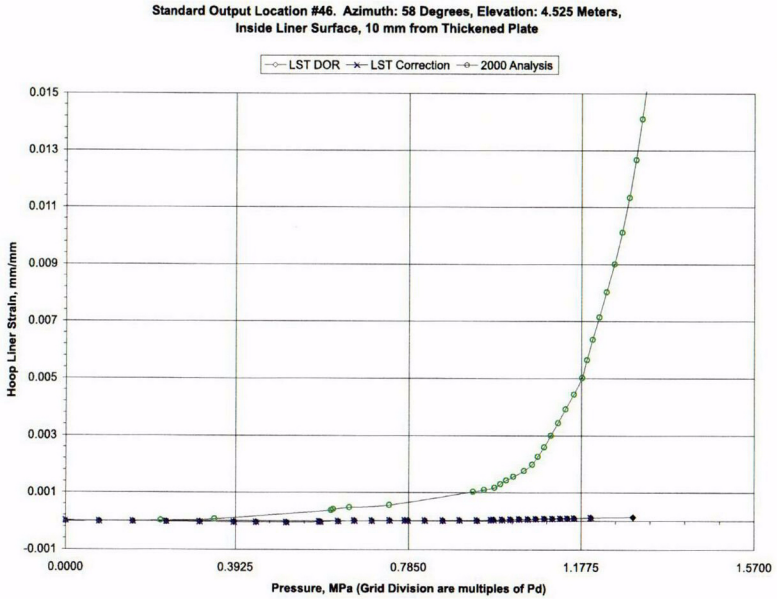

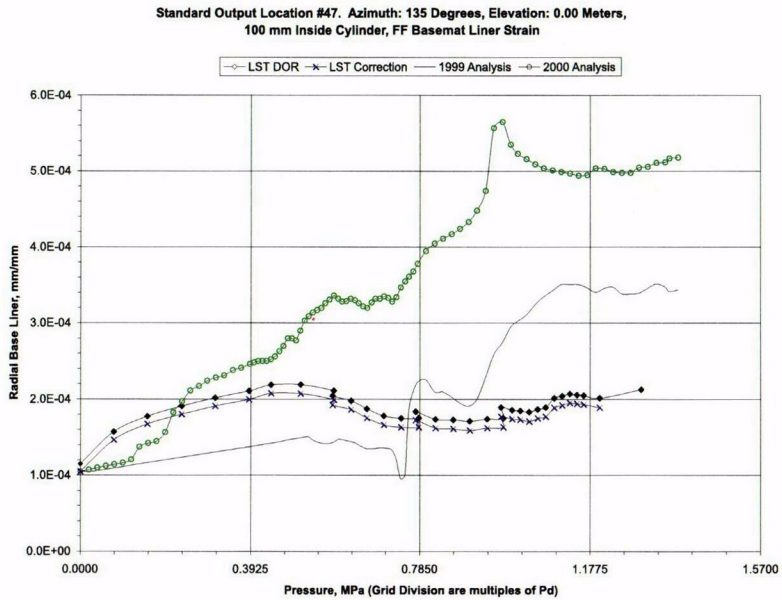

Figure 4-13. Comparisons at Standard Output Location 46 and 47

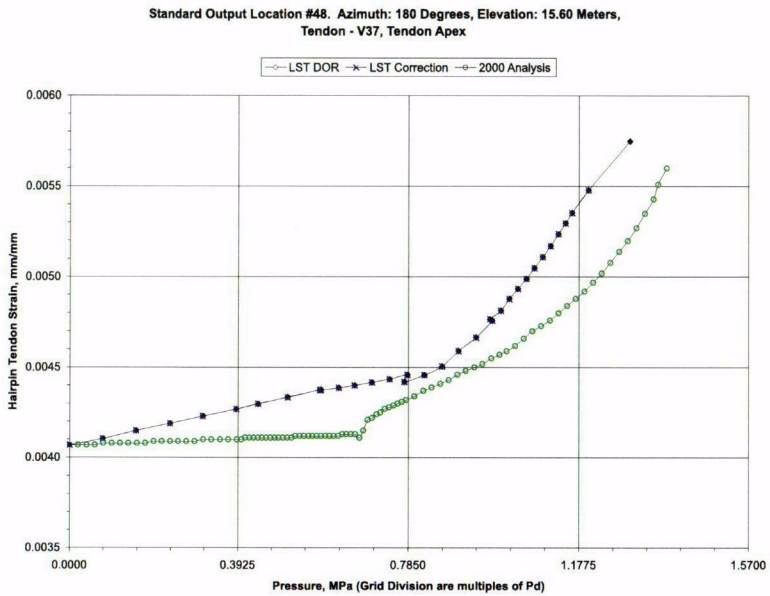

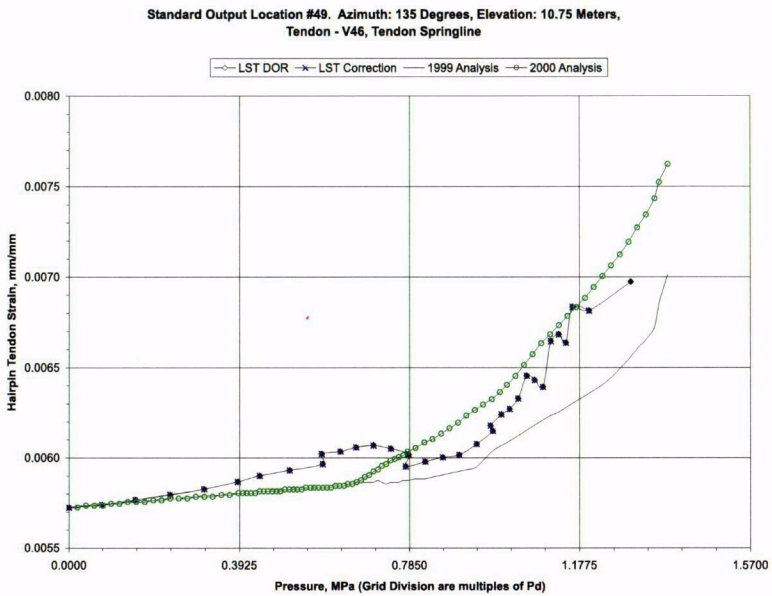

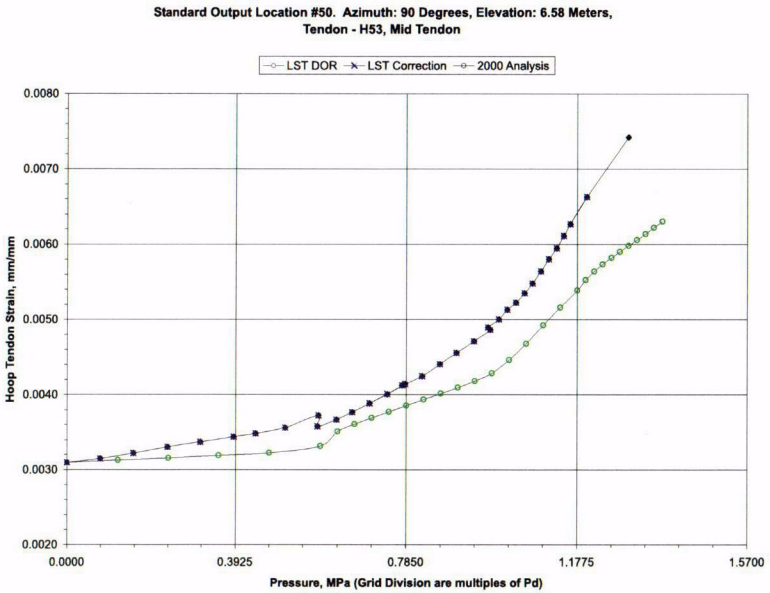

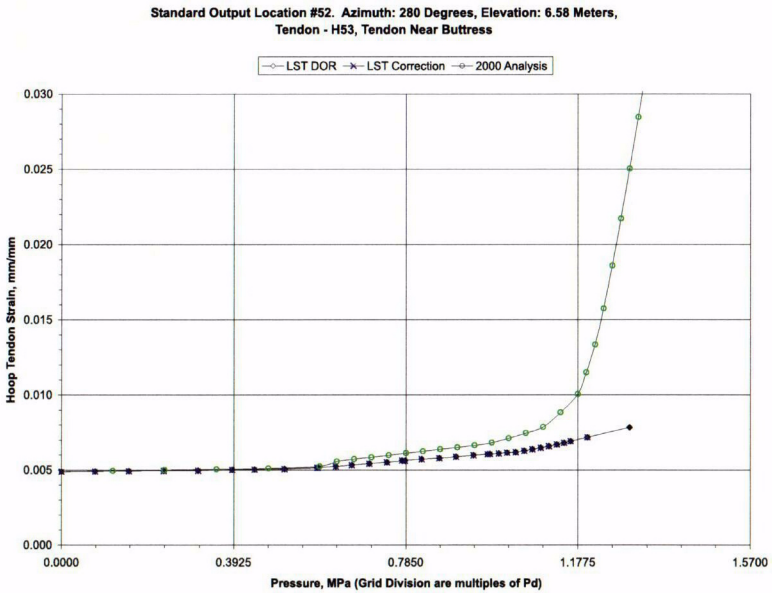

Figure 4-14. Comparisons at Standard Output Location 48, 49, 50, and 52

C22

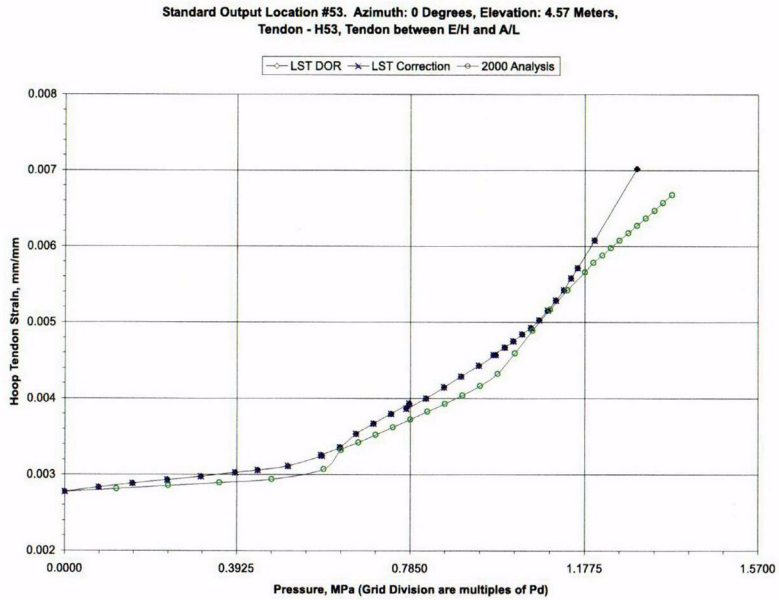

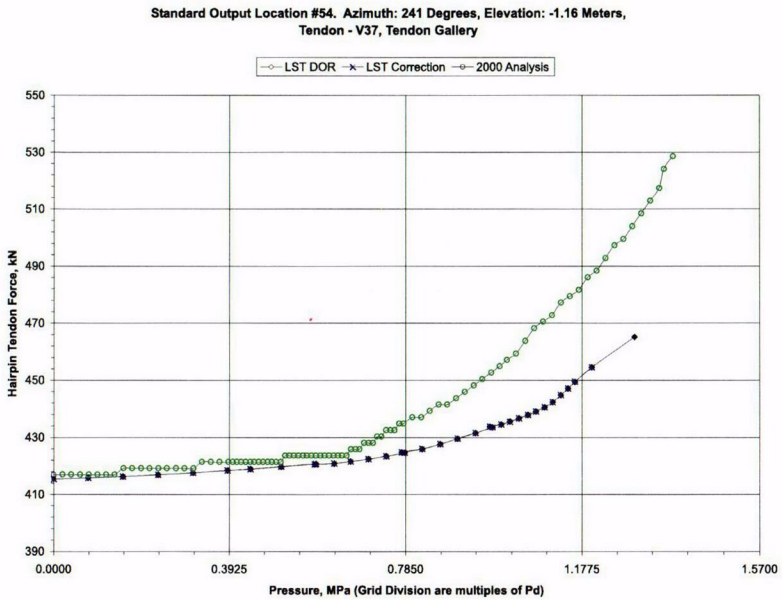

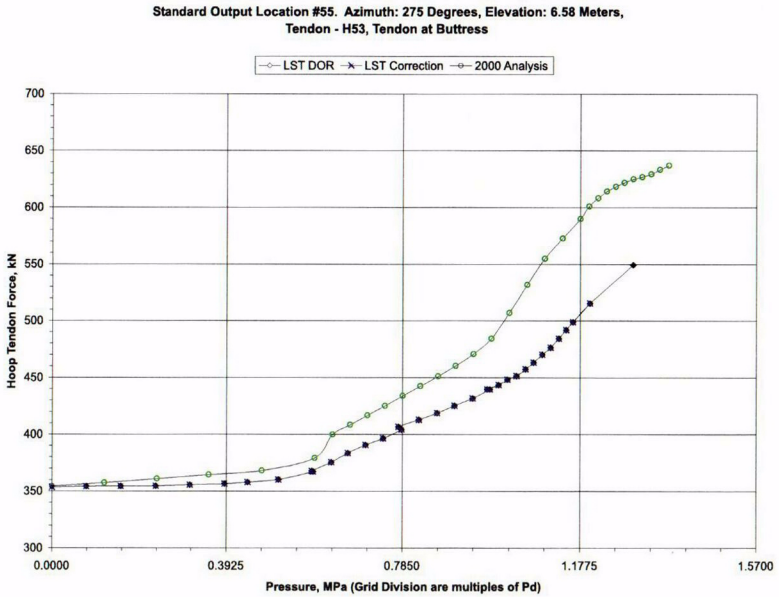

Figure 4-15. Comparisons at Standard Output Location 53, 54, and 55

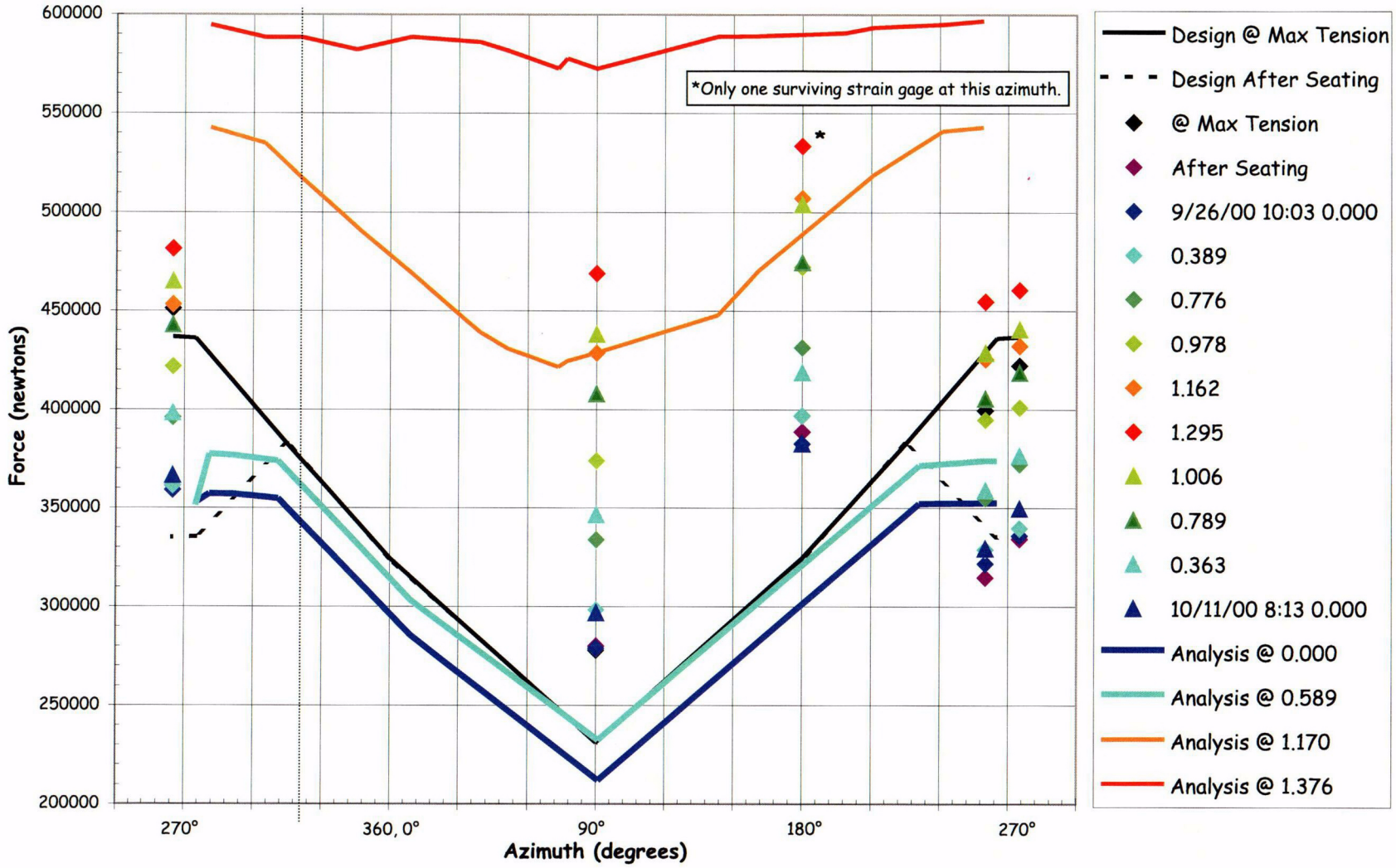

Figure 4-16. H11 Tendon Force Distribution, El. 1854 (Load Cells and Average of Wire Strain Gages)

C24

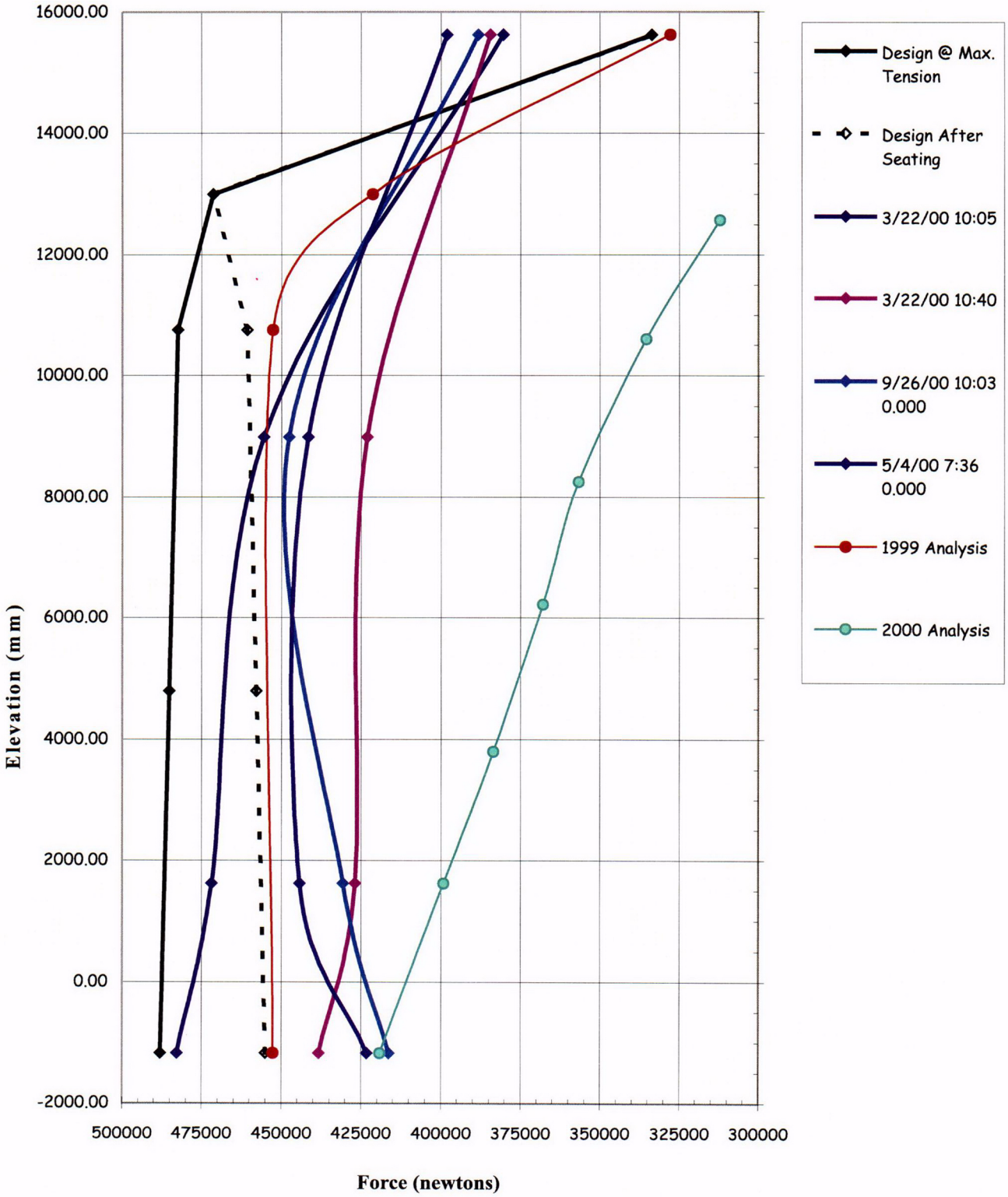

Figure 4-17. V37 Tendon Force Distribution @ Azimuth 240
(Load Cells and Average of Wire Strain Gages)

C25

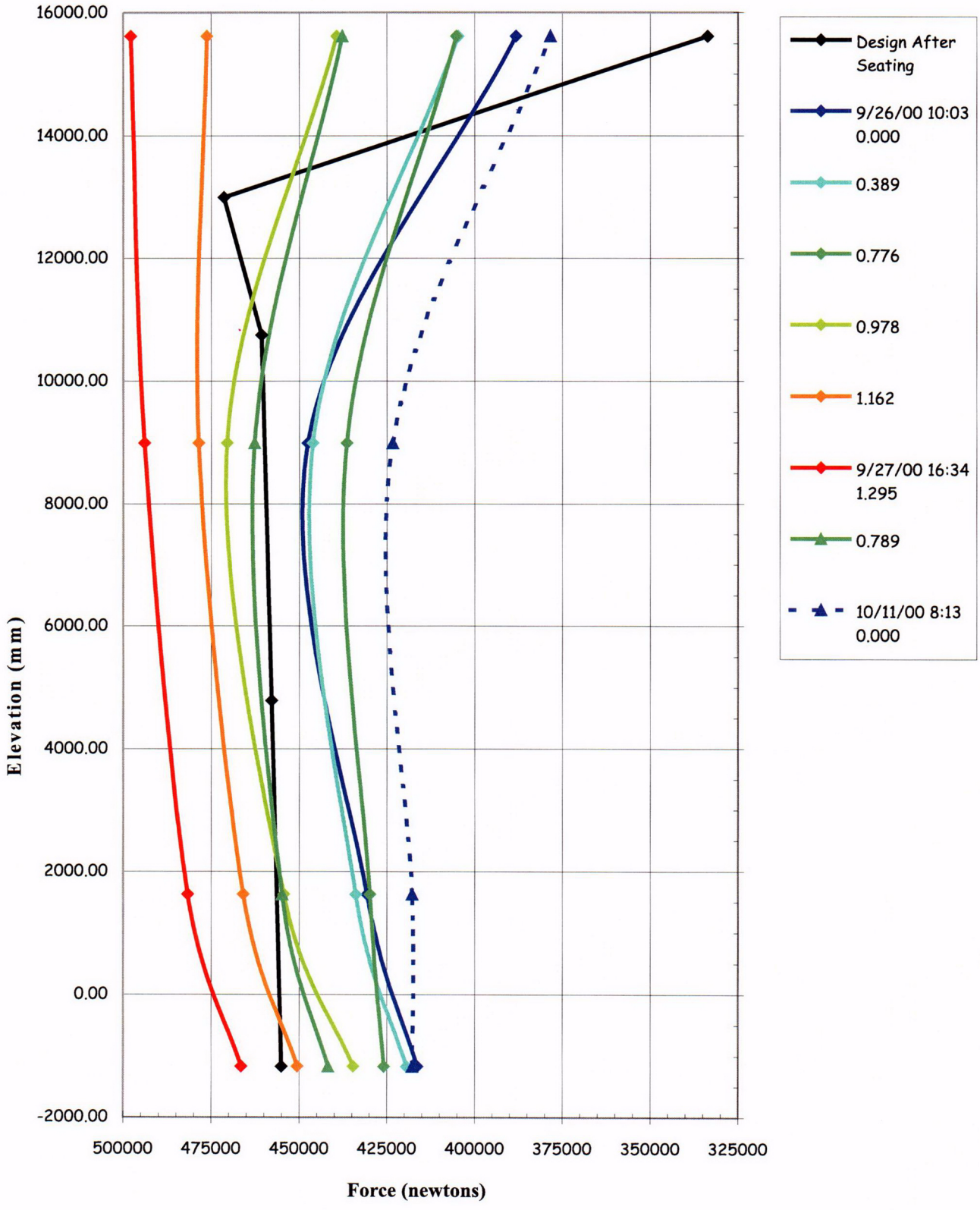

Figure 4-18. V37 Tendon Force Distribution @ Azimuth 240
(Load Cells and Average of Wire Strain Gages)

C26

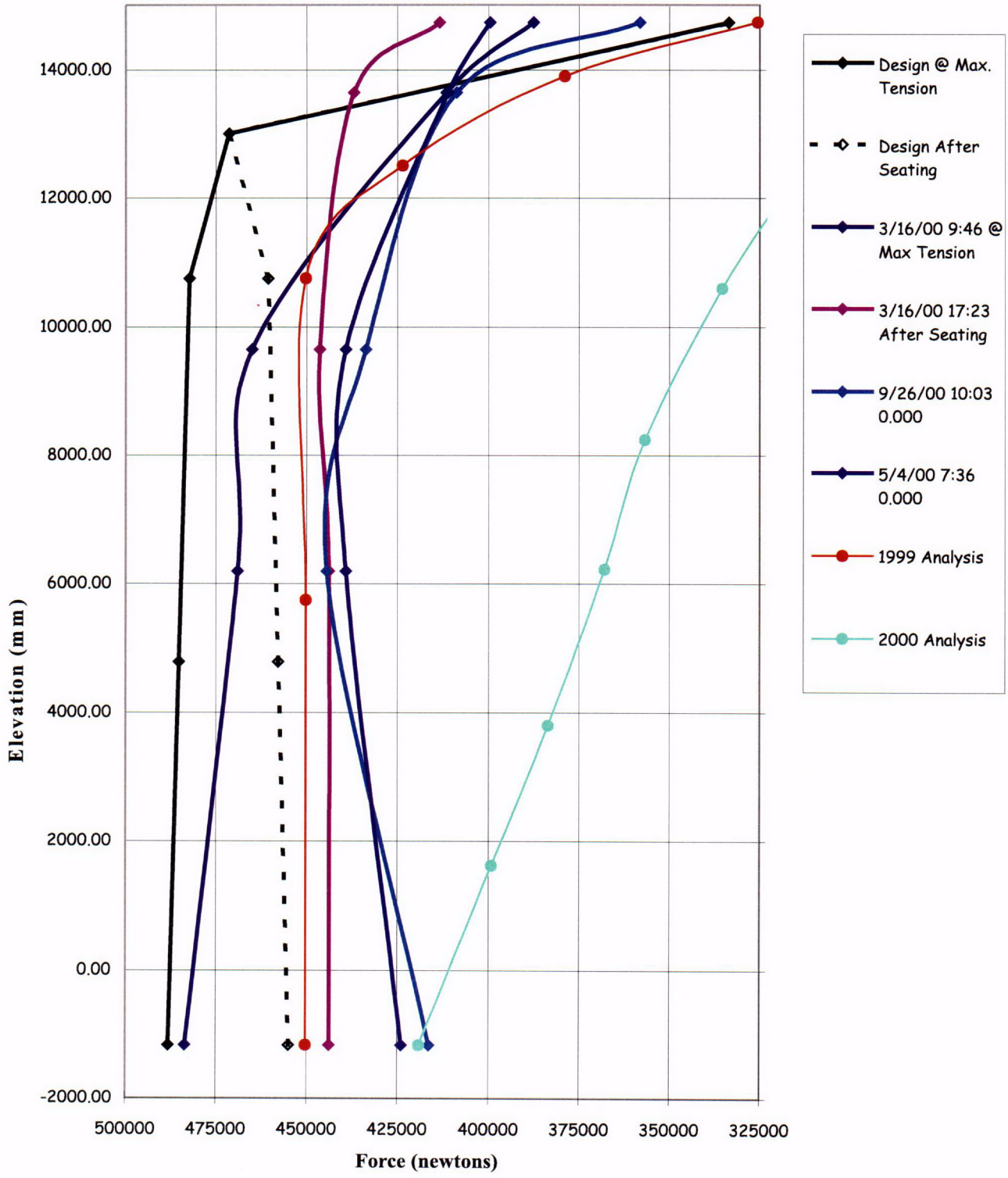

Figure 4-19. V46 Tendon Force Distribution @ Azimuth 135
(Load Cells and Average of Wire Strain Gages)

C27

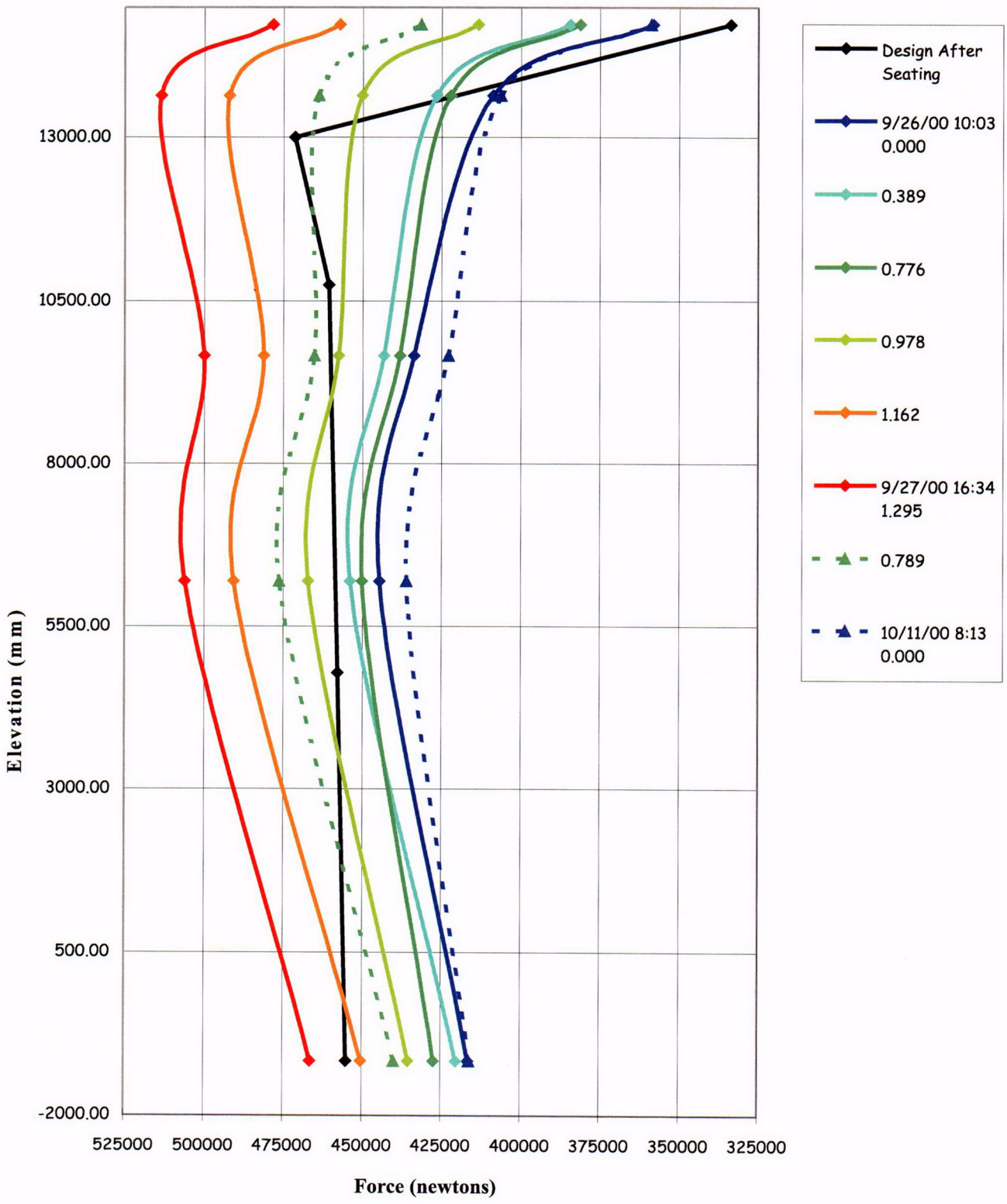

Figure 4-20. V46 Tendon Force Distribution @ Azimuth 135□
(Load Cells and Average of Wire Strain Gages)

C28

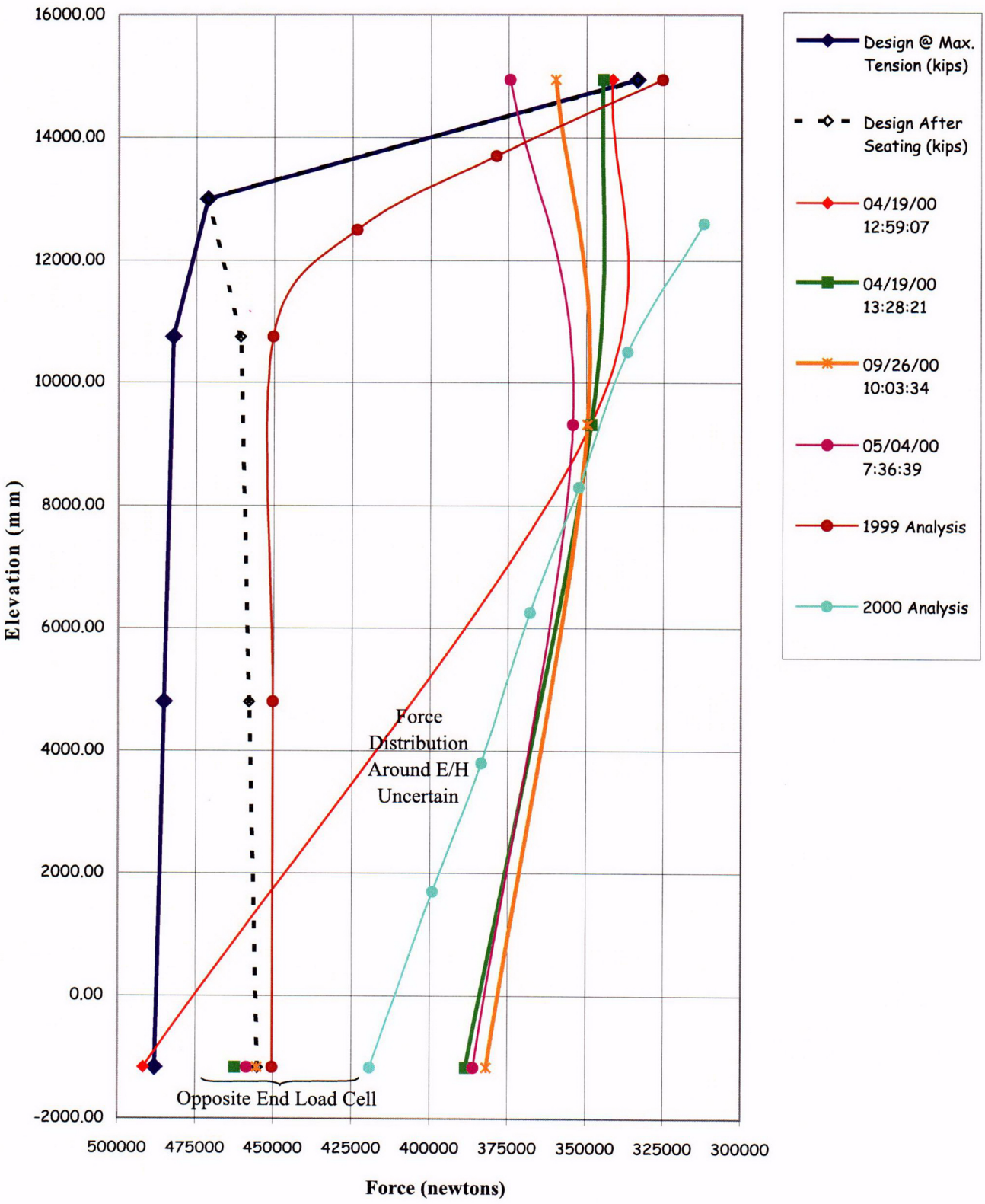

Figure 4-21. V85 Tendon Force Distribution @ Azimuth 325
(Load Cells and Average of Wire Strain Gages)

C29

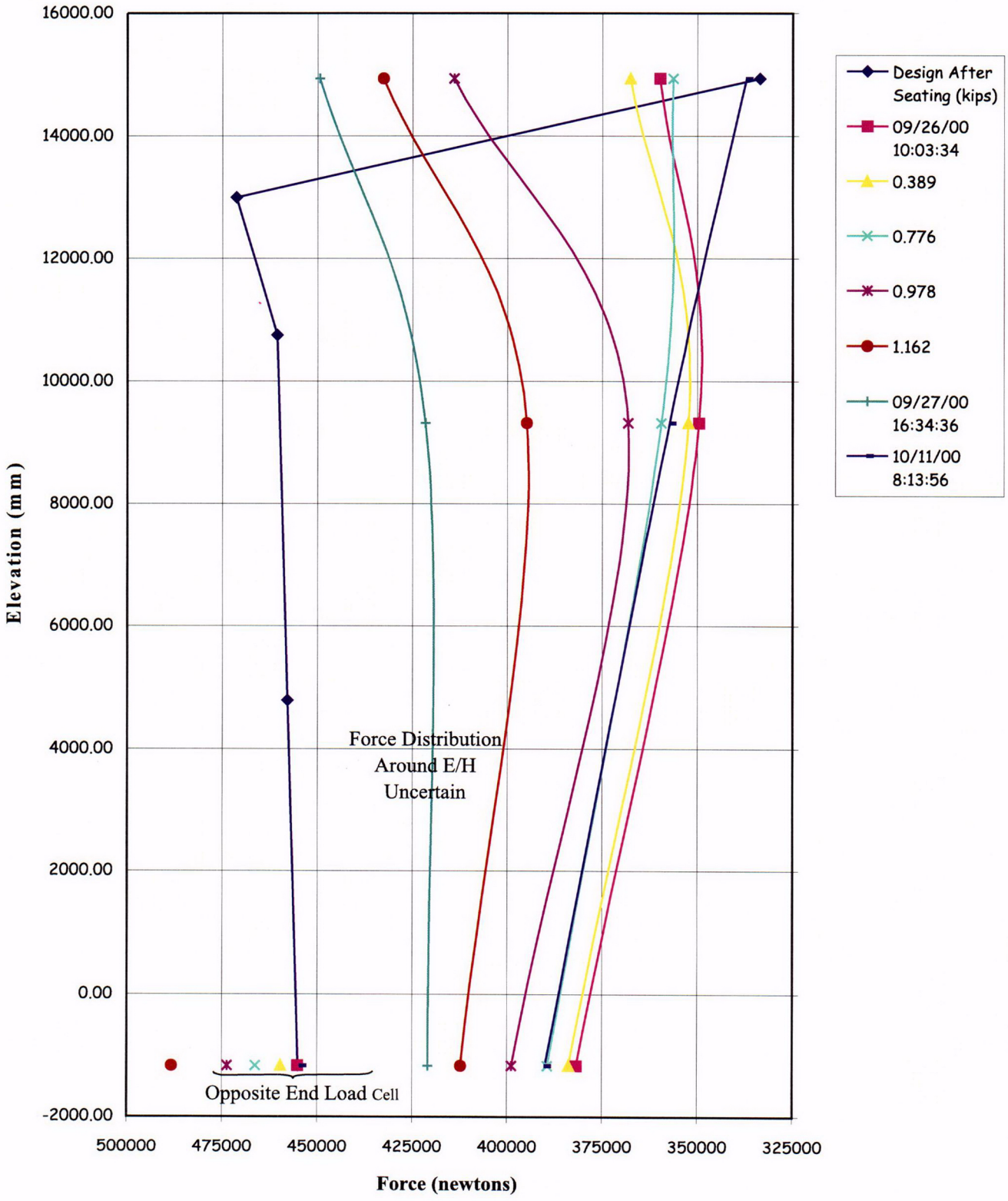

Figure 4-22. V85 Tendon Force Distribution @ Azimuth 325
(Load Cells and Average of Wire Strain Gages)

C30